CHARACTERISTICS OF CONVECTIVE CLOUDS OVER THE INDIAN MONSOON ZONE DERIVED FROM WEATHER RADAR DATA

A thesis submitted for the degree of

Doctor of Philosophy

In the

Faculty of Engineering

By

KAPIL DEV SINDHU

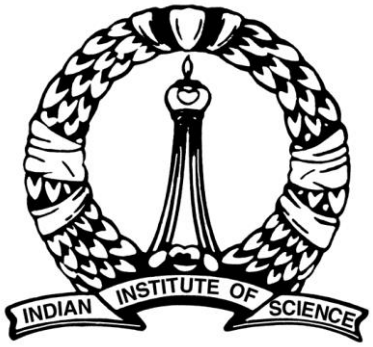

Centre for Atmospheric and Oceanic Sciences

Indian Institute of Science

Bangalore-560012, India

April, 2018

****

Dedicated to *my Amma and Dada, my Parents and my Family members*

****

Declaration

I hereby declare that I am the sole author of this thesis. My thesis contains original work and key findings obtained by me and carried out at Centre for Atmospheric and Oceanic Sciences, Indian Institute of Science (Bangalore). Partly, my thesis contains the text and figures including tables and supplemental material from the research papers from my thesis work and primarily authored by me with the consent of, coauthor (if any) and publication authorities under the copyright statements quoted by publications agencies.

I authorize Indian Institute of Science (Bangalore) to lend this thesis to other institutions or individuals for the purpose of non-profit scholarly research.

Kapil Dev Sindhu
April, 2018
I. I. Sc. Bangalore

Acknowledgements

It is a great pleasure for me to express my gratitude towards my mentor Prof. G. S. Bhat. He always motivated me and supervised me in such a way that I always felt confident. His perfection and dedication towards research made me sincere and hardworking. It is his kindness that I am here in CAOS and completed my PhD with pride and wisdom. Certainly, he will be always a source of inspiration for me.

I am immensely thankful to Mr. Michael Dixon, PI of TITAN at UCAR, USA. He helped me up to my required needs regarding radar data processing. His continuous suggestions and discussions are remarkable. I also thank Mr. S. B. Thampi, RMC, Chennai for discussing radar data formats.

I deeply acknowledge the CloudSat and TRMM administrations, PI's and authorities of CTCZ experiment and India Meteorological Department for providing datasets for PhD research. I am grateful to the Institute for proving PhD scholarship. I also acknowledge all the funding agencies for their financial support during PhD degree.

I am grateful to Prof. Debasis Sengupta (Chairman, CAOS) and Prof. Ravi S. Nanjundiah (Former Chairman, CAOS), IISc Bangalore for providing all facilities and administrative support during PhD degree. I am thankful to all CAOS staff for helping me regarding all local administrative work.

I am happy to have my special friends Ram and Basant for sharing precious time with me. I enjoyed a lot many memorable moments of my life with them.

I am very thankful to Deepesh for his support and help. I also thank Shailendra and Jayesh for their research inputs during lab meetings. I thank Prabhat, Jahfer and Mahesh for helping in computational stuff. I thank Surajit, Harsha, Gaurav S, Santosh, Arvind and Manu Sir for sharing a good company during my final days at IISc.

My Amma, Dada, Mom, Papa, and all my family members are the key people who always pray for my good health and happy life. Their unconditional and selfless blessings brought me here and that's why today I see myself a successful and blessed person who is full with the confidence. I am extremely privileged to have such a beautiful family. I wish all of them for their healthy and prosperous long life together.

With special thanks to my wife Sonika who supports me and gives me strength in my adverse time. Her unconditional love and care admire me. She makes every moment of my life beautiful and joyful. I am really privileged to be a part of her life forever and together.

My mistakes and failures taught me not to lose hope and patience in hard time. Every unwanted failure which comes with a bunch of several mistakes but later that turned into success. I would like to give credit to my mistakes and failures for teaching me secret lessons to be a good researcher.

Thank You.

Kapil Dev Sindhu

April, 2018

I. I. Sc. Bangalore

Abstract

Deep convective clouds play an important role in global energy balance through vertical transport of water vapor, momentum and energy, altering radiation and also influence hydrological cycle via precipitation. These clouds are organized mainly at Synoptic scale (~1000 km), Mesoscale (~100 km) and storm-scale (~10 km) and involve interactions from micro-scale (e.g., cloud condensation nuclei and droplets) to planetary scale. Physical processes associated with such clouds are the largest sources of uncertainty in atmospheric weather and climate models. Clouds involve rich physics and therefore, studying and understanding of convective clouds is an important research area in weather and climate sciences.

In present work, the mesoscale and storm scales of convective cloud systems are addressed using spacebrone and ground based Doppler weather (conventional and polarimetric) radars. The work started with the analysis of cloud systems over Tibetan Plateau. These cloud systems are observed to be very deep in nature. After finding the underestimation of radar reflectivity especially in convective regime, analysis is further extended in entire latitudinal belt of 38°N-38°S. The coincident data collected with the precipitation radar (PR) onboard TRMM (Tropical Precipitation measuring Mission) satellite and profiling radar (CPR) onboard CloudSat satellite is used. It is shown the PR measures properties of convective part but it misses portions of the anvil part of mesoscale convective cloud systems (MCSs). CPR measures the full spatial extent of MCSs however its reflectivity values are very low due to the strong attenuation suffered by the radar beam while passing through a precipitating convective cloud. CPR beam gets attenuated severely during convective rain episodes especially below 6 km height. While going by their technical specification, we can expect substantial overlap in the radar reflectivity factor for convective clouds, very little overlap is observed. One should be very careful while drawing conclusions on the cloud characteristics measured with the PR and CPR. I felt that it is better to study the cloud properties using ground radars, hence, most of the results reported in the thesis are based on ground radar data.

As part of the Continental Tropical Convergence Zone (CTCZ) program of the Ministry of Earth Sciences, Govt. India, India Meteorological Department (IMD) made available its

Doppler weather radar (DWR) data for the years 2012 and 2013 to researchers within the country. Using IMD DWR data, life cycle of monsoonal MCSs over Indian monsoon zone and properties of storms embedded within MCSs are studied at five locations, namely, Kolkata, Hyderabad, Nagpur, Patiala and Delhi. Stages in the lifecycle of MCSs have been explored including convective area and precipitation fractions. It was observed that intense precipitation within an MCS is confined to several pockets having areas much smaller than that of an MCS. Those convective cells are called storms in this work. Storm is a precipitating convective cloud having a volume of more than 50 km^3 of connected pixels with radar reflectivity factor of at least 30 dBZ. The results of storm properties are reported for the first time using the DWR data for the Indian subcontinent. It is observed that the growth phase of an MCS is characterized by a rapid increase in the number of storms. An MCS can have more than one growth and decay phases during its lifetime. MCS may contain few or large number of storms depending upon geographic location and life phase. Average area of storms varies from less than 20 to more than 250 km^2, while average storm height lies typically between 6 and 10 km. In one extreme case, it is found even 17 km. Average convective precipitation fraction (CPF) is 40% or less, highest at Kolkata, Hyderabad, Patiala and Delhi (~40%) and the least at Nagpur (13%). Average convective area fraction (CAF) is less than 15% at all locations. The maximum CAF and CPF can go higher up to 45% and 90% respectively. The most intense convective clouds are observed over Patiala and Delhi where 30 dBZ radar echoes are found above 10 km. These locations lie near Himalayan foothills. According to previous studies, this region experiences intense convective systems due to high degree of potential instability caused by high moisture flux from low-level air flow from Arabian Sea to over foothills of Himalayas which interacts with extra moisture supplied from soil wetted from earlier precipitation. The vertical structure of MCSs is different at each radar location. These differences appear remarkably below 5 km and above 10 km altitudes. The final part of the thesis is based on the analysis of data from a polarimetric DWR located at Delhi. Using polarimetric DWR radar reflectivity data at Delhi (a land Indian region), the three prominent features of an MCS (Severe precipitation (below 4 km), melting band (at ~4 km) and anvil structures at higher altitudes (~12 km) are captured in vertical distributions of convective and stratiform echoes. Convective clouds are very deep over the Delhi region, many of them extended beyond 16

km. The typical storm duration is an hour while few exceed 3½ hours. Storms those have large average areas and long durations contribute more in precipitation amount. The average precipitation rate (R) of storms is estimated in between 5 and 34 mm hr^{-1}. The total accumulated precipitation (P_{acc}) derived from polarimetric variable (K_{dp}) is as large as 250 mm in 6 days at Delhi. The cloud liquid water content (M) is derived using horizontal radar reflectivity (Z_h, property of cloud volume observed by the radar beam which is which is proportional to the 6^{th} moment of the diameter of hydrometeors) and specific differential phase (a measure of phase difference between horizontally and vertically polarized waves). The mean of cloud liquid water content derived from Z_h (~1 gm m^{-3}) is just half of that derived from K_{dp}. However, their maximum bound (~4.2 gm m^{-3}) are found similar but have different frequencies. At each altitude, values of M vary largely which reflects the natural variability in clouds. One of the important finding is that the P_{acc} and M estimates are found to be more realistic when derived using polarimetric variable.

Contents

Acknowledgements

Abstract

List of Publications

List of Figures

List of Tables

Notations and Abbreviations

1. Introduction

2. Data and methods

3. Properties of clouds over the Tibetan Plateau and comparison of CPR and PR reflectivities

4. Characteristics of mesoscale convective systems

5. Properties of convective clouds measured by a polarimetric DWR at Delhi

6. Conclusions

References

List of Publications

1. **Sindhu and Bhat (2013),** Comparison of CloudSat and TRMM radar reflectivities. (*Journal of Earth System Science.* **122**, 947-956).

2. **Sindhu and Bhat (2018)**, Characteristics of mesoscale convective systems over the Indian monsoon zone. (Under Revision in *Quarterly Journal of the Royal Meteorological Society*)

3. **Sindhu and Bhat (2018),** Properties of Convective Clouds over Northwest India Measured by C-band Polarimetric Doppler Weather Radar. (To be submitted to *Journal of Hydrometeorology*)

List of Figures

Figure 2.1. Geo-locations of S-band DWRs overlaid USGS global 30 arc-second terrain elevation. Radius of the outer circle around each radar location is of 150 km. Abbreviations used here are the following: DLI-Delhi, HYD-Hyderabad, KOL-Kolkata, NGP-Nagpur, PTL-Patiala.

Figure 2.2. Typical ranges of Z_{dr} and K_{dp} and corresponding target characteristics (Courtesy: National Weather Service, USA).

Figure 2.3. Projection of column maximum of radar reflectivity Z_h, differential reflectivity Z_{dr} and specific differential phase K_{dp} are shown in panels (a), (c) and (e) respectively observed on 11 June at 0712 LST. The corresponding vertical sections taken along line AB are shown in panels (b), (d) and (e), respectively. The color bars on right refer to Z_h (in dBZ), Z_{dr} (in dB) and K_{dp} (in deg km^{-1}) respectively.

Figure 2.4. Contour lines of infrared brightness temperature overlaid onto the horizontal projection of the maximum Z_e of all vertical levels for an MCS observed over Kolkata on 2 September, 2013. Different plots correspond to time (a) 0730 UTC, (b) 0800 UTC, (c) 0830 UTC, and (d) 0900 UTC.

Figure 2.5. Illustration of the steps involved in the identification of convective pixels in MCS. The cloud system was observed over Nagpur at 1330 LST on 14 June 2013: (a) projection of maximum Z_e between 2 and 3 km (b) pixels having $Z_e \geq 40$ dBZ (convective). (c) convective pixels resulting from the BG criterion. (d) horizontal gradient in Z_e. (e) convective pixels resulting from the Z_s criterion and (f) total convective pixels.

Figure 2.6. (a). Projection of the maximum Z_e between 2 and 3 km for an MCS observed at 2120 LST on 14 June, 2013 over Nagpur. (b) Convective and stratiform areas for the cloud system shown in (a). (c) Vertical cross section along the line AB in panel (b). In (a) and (b) filled red circle shows the location of radar.

Figure 3.1. Average vertical profiles of moist static energy measured at upper air stations in the Tibetan Plateau region during May to September months in the year 2008. Left: Lhasa (29.6°N, 91.1°E) and, right: Nagquo (31.4°N, 92°E). The radiosonde data is obtained from the University of Wyoming for both the locations.

Figure 3.2. Brightness temperature measured by Kalpana-1 satellite over Indian region. The red line shows the descending overpass of CPR through the cyclone AILA observed at 18:30 LST on 25 May, 2009.

Figure 3.3. Vertical section through a cloud system over the Tibetan Plateau captured with the CPR. The colorbar coded here is CPR radar reflectivity in dBZ units. The signatures of deep convective cloud and melting band (around 5 km altitude) are captured. Thick red line shows the land surface elevation of Tibetan Plateau along the section.

Figure 3.4. Cloud systems over Tibetan Plateau observed by CloudSat on (a) 7 August, 2007, (b) 13 July, 2008, (c) 19 July, 2008 and (d) 10 August, 2010. The colorbar coded here is radar reflectivity in dBZ.

Figure 3.5. Vertical profiles of monthly mean of maximum Z_e over Tibetan Plateau for the year 2008. Each profile corresponding to each month is mean of all vertical profiles of the maximum Z_e during that month. Panels (a) and (b) are corresponding to CPR ascending and descending overpasses over Tibetan Plateau.

Figure 3.6. Example of TRMM PR and CloudSat CPR coincident overpasses observed on 8 July 2008 over Bay of Bengal (top); 13 July 2008 over Tibetan Plateau (middle), and 10 August 2010 over Tibetan Plateau (bottom). Continuous lines show the path of CloudSat and parallelograms PR footprints. For PR, the maximum reflectivity in each vertical column of the grid is projected onto the plane. Color bar on the top refers to PR Z_e in dBZ units.

Figure 3.7. Intersection points of coincident CPR and PR overpasses for the period July 2006 to December 2010.

Figure 3.8. Number of coincident points at different vertical levels for case 1 and case 2. For case 1, both CPR and PR show similar trend but not exactly identical owing to the difference in their footprint sizes. Numbers of coincident points are very few above 15 km. For case 2, CPR shows a peak around the freezing level and at 2 km height, whereas PR has peak at 2 km and numbers drop drastically above 10 km.

Figure 3.9. Contoured frequency by altitude diagrams (CFADs) of reflectivities for case 1 (top) and case 2 (bottom). The bin size for Z_e is 5 dBZ and height intervals are 0.24 km and 0.25 km for CPR and PR respectively. The color bar shows the frequency (in %) of reflectivity occurrence. Differences in the maximum heights of the contours and abrupt ending are due to the number of points falling below the 10% criterion used in CFADs (see text for details). The contours' values lower than the minimum detectable limit of 17 dBZ has been discarded in PR CFAD.

Figure 3.10. (a) Vertical variation of the mean reflectivity for CPR and PR for case 1. The error bars correspond to one standard deviation about the mean. At no height, two measurements come close to each other, and mean trends are in opposite directions below 6 km level. (b) Vertical variation in the maximum frequency of occurrence of CPR and PR reflectivities for case 1 indicating the preference for a certain Z_e to occur more frequently at that height, and the mode itself a function of height as shown in Figure 3.9. (c) Histograms of the reflectivities for CPR and PR for case 1. Reflectivity values at all heights are taken into consideration while constructing these histograms. Curves (in red and black colors) are the probability density functions obtained by fitting normal distribution function.

Figure 3.11. Vertical cross sections of PR Z_e superimposed on that of CPR along the CloudSat path for the cases shown in Figure 3.6 in the same order. Discrete vertical bars

and blue color correspond to PR and CPR reflectivities, respectively. High values at the bottom may be due to surface reflectance (especially over the Tibetan Plateau). The color bar shows the radar reflectivity values in dBZ.

Figure 3.12. Intercomparison of probability distributions of radar reflectivity obtained from CloudSat CPR, TRMM PR and DWR.

Figure 4.1. Merging of two storms within the MCS observed over Patna on 14 August in the year 2012 at 8:42 UTC.

Figure 4.2. Vertical structures of storms within MCS. Each panel is obtained at the interval of 10 minutes.

Figure 4.3. Temporal evolution of convective, stratiform and total area of MCSs observed on (a) 2 September 2013 over Kolkata, (b) 5 June 2013 over Hyderabad, (c) 13 June 2013 over Nagpur, (d) 11 June 2013 over Patiala and (e) 13 June 2013 over Delhi. Here the stratiform and total areas are divided by 5 so that areas look comparable and fit in the same graph

Figure 4.4. Skew-*T* log *p* diagram of temperature and dew-point temperature from radiosonde data measured over (a) Kolkata (2 September), (b) Hyderabad (5 June), (c) Nagpur (13 June), (d) Patiala (11 June) and (e) Delhi (13 June) in the year 2013.

Figure 4.5. MCS observed on 2 September 2013 over Kolkata. (a) Satellite IR brightness temperature at 0904 LST. Circles shown here are 50 km distant each other having radius of outermost circle of 150 km. (b) Spatial extent of the MCS at 0900 LST revealed in the projection of the maximum Z_e between 2 and 3 km. Units of x- and y- distances are the number of pixels of the re-gridded data in respective directions, and the pixel size is 2 km × 2 km. Arrow at the top left corner points in the direction of the gross movement of the MCS around this time. (c) Pixels contain convective precipitation. Many of the pixels marked in red belong to storms. (d) Spatial distribution of the instantaneous rain rate at 1.5 km height. The color bar is in logarithmic scale. (e) Temporal variation in the number of storms embedded in the MCS. (f) Time evolution of total storm (As) and convective (Ac) areas within the MCS. (g) Convective precipitation fraction (CPF) and convective area fraction (CAF) and (h) total and convective precipitation accumulation rates.

Figure 4.6. As Figure 4.5, but for MCS observed on 5 June 2013 over Hyderabad. Instantaneous snapshot is at 2330 LST.

Figure 4.7. As Figure 4.5, but for MCS observed on 13 June 2013 over Nagpur. Instantaneous snapshot is taken at 1830 LST. CAF is rather small here, often less than 5%.

Figure 4.8. As Figure 4.5, but for MCS observed on 11 June 2013 over Patiala. Instantaneous snapshot is taken at 1300 LST.

Figure 4.9. As Figure 4.5, but for MCS observed on 13 June 2013 over Delhi. Instantaneous snapshot is taken at 0830 LST.

Figure 4.10. Statistics of convective area fraction and convective precipitation fraction for (a) and (b) for MCSs considered for life cycle studies and (c, d) for all clouds within 150 km radar range during July and August. All data are from S-band except for Delhi which is C-band. See Figure 2.1 for the station abbreviations shown along the x-axis. Filled circle and the horizontal bar nearest to it are the average and the median of the population, respectively.

Figure 4.11. (a) Temporal variations of the average area of storms embedded in the MCSs shown in figures 4.5 to 4.9. (b) Average height of the storms. On average, storms at Nagpur are much narrower but their height is marginally more compared to the rest. In the dissipation stage of the MCS at Kolkata, both the number of storms and their area decreased.

Figure 4.12. Distributions of echo top heights of 30 dBZ and 40 dBZ within convective echoes. (a-b) probability, (c-d) cumulative probability.

Figure 4.13. (a-e) Vertical profiles of radar reflectivity (*VPRR*) of convective echoes in MCSs. N is the total number of *VPRR*s and thick line is the mean profile of all *VPRRs.* The horizontal lines around the mean curve indicate 1-standard deviation of all *VPRRs*. (f) comparison of mean of all VPRRs at different stations.

Figure 5.1. Top: KALPANA-1 IR brightness temperature, left: 11 June, 2013 at 1300 LST; right: 13 June, 2013 at 0830 LST. Lower panels: Skew-*T* log*p* diagrams of temperature and dew-point temperatures at Delhi on 10, 11, 13 and 14 June in the year 2013. Line legend is same in all sub-plots.

Figure 5.2. Left panel shows the projection of column maximum Z_h. Right panel a vertical section long line AB shown in left panel. Date is 11 June 2013 and top, middle and lower panels were observed at 0530 IST, 0630 IST and 0730 IST, respectively.

Figure 5.3. Contoured frequency by altitude diagrams (CFADs) for (a) convective and (b) stratiform cells. Variable used is Z_h. Color bars for panels (a) and (b) show the frequency of radar echoes. Panels (c) and (d) show the vertical profiles of mean Z_h and the maximum frequency of occurrence of Z_h, respectively.

Figure 5.4. Storms characteristics: (a) Life duration, (b) Propagation speed, (c) Propagation direction and (d) area. (e) Horizontal projection of the columnar maximum Z_h and (f) Vertical section taken along line AB for storm observed on 11 June at 0700 LST whose area exceed than 400 km^2.

Figure 5.5. (a-c) Temporal evolution of properties of long-lived storm (~3½ hours) observed on 13 June 2013. (a) Maximum and average values of Z_h, (b) ETH of 30 dBZ and Z_{max} echoes and precipitation rate calculated at an altitude of 1.5 km. Precipitation rate is expressed in mm hr^{-1} units, (c) Area and volume. Note that the area is multiplied by 10 to fit the two curves in the same plot.

Figure 5.6. Average characteristics of storms: (a) Scatter plot between mean echo area (EA_{mean}) and storm life duration. (b) Scatter plot between mean echo area and area time

integral ATI. (c) Scatter plot between maximum echo top height and total precipitation amount expressed as mass of rain water. (d) Scatter plot between ATI and total precipitation amount. The symbol '×' and 'filled circles' correspond to storms with life duration of more and less than one and half hour, respectively.

Figure 5.7. (a) Probability and (b) cumulative probability distribution of precipitation rates derived from different Z-R relations (see Table 2.4).

Figure 5.8. Horizontal structure of total accumulated precipitation (in mm) during 6, 12, 13, 14, 15 and 16 June derived using (a) R_{IG}, (b) R_{HMP}, (c) R_{BC} and (d) R_{DZ} (see Table 2.4 for functional forms).

Figure 5.9. The distribution of IMD rain gauges around C-band polarimetric Doppler weather radar (28.58°N, 77.22°E). The rain gauges within the 5 km radius (in white filled-in circles) around DWR are excluded in the rainfall estimates. Following are the IMD rain gauge locations: (1) Pusa (77.16°E, 28.64°N), Akshardham (77.27°E, 28.61°N), Mungeshpur (76.97°E, 28.82°N) Narela (77.08°E, 28.85°N), Pitampura (77.15°E, 28.7°N), Aya Nagar (77.02°E, 28.68°N), Palam (77.12°E, 28.57°N), Lodi Road (77.24°E, 28.59°N), Safdarjung (77.23°E, 28.66°N), Delhi Ridge (77.18°E, 28.62°N), Delhi University (77.1°E, 28.7°N).

Figure 5.10. Comparison between DWR and Rain gauge accumulated precipitation. The vertical bar at each data point is the 1-standard deviation of rainfall accumulation at each DWR pixel around the rain gauge location.

Figure 5.11. Cloud liquid water content (M) estimated using (a) M_{GC}, (b) M_{BC}, and (c) M_{DZ} (see Table 2.5 for functional forms). The filled circles are the average values of M at each altitude. Here, the horizontal bar within the box is the median value, and the lower and upper limits of M show 25% and 75% percentile of the data. Black dots beyond 75% percentile of M indicate the outliers in data.

List of Tables

Table 2.1. Technical specifications of CloudSat CPR and TRMM PR.

Table 2.2. Geo-locations of the S-band DWRs, their technical specifications, scan angles and data availability.

Table 2.3. Specifications, provided products and data availability of C-band polarimetric DWR.

Table 2.4. Relationships used for estimating rain rate R (mm hr^{-1}).

Table 2.5. Relationships used for estimating cloud liquid water content M (gm m^{-3}).

Table 5.1. Normalized bias and RMSE between rain gauge and DWR derived accumulated precipitations.

Table 5.2. Mean and maximum cloud liquid water content (M) derived from Z_h and K_{dp}.

Notations and Abbreviations

ATI	Area-time integral
BBF	Bright band fraction
c	Speed of light
CAF	Convective area fraction
CAPPI	Constant altitude plan position indicator
Cb	Cumulonimbus
CFAD	Contoured frequency by altitude diagram
CIMO	Commission for instruments and methods of observations
CPR	Cloud profiling radar
CAF	Convective area fraction
CPF	Convective precipitation fraction
CTCZ	Continental tropical convergence zone
dB	Decibel
dBZ	Unit of radar reflectivity in decibel
D_i	Diameter of i^{th} particle in cloud volume
DSD	Drop size distribution
DWR	Doppler weather radar
f	Frequency of radar
G_o	Antenna gain
ICRP	Indian climate research programme
IMD	India meteorological department
JAXA	Japan aerospace exploration agency
K	Dielectric constant of water
K_{dp}	Specific differential phase
LST	Local standard time
M	Cloud liquid water content
MCSs	Mesoscale convective systems
MDV	Meteorological data volume
NASA	National aeronautics and space administration
NB	Normalized bias
NCAR	National centre for atmospheric research

NCEP	National centers for environmental prediction
PR	Precipitation radar
P_t	Transmitted power
r	Radar beam range
R	Rain rate
R_c	Average rain rate
R_{DWR}	Rainfall derived from DWR variables
RERV	Radar estimated rain volume
R_{gauge}	Rainfall from rain gauge
RMSE	Root mean square error
T_B	Brightness temperature
TITAN	Thunderstorms identification, tracking, analysis and nowcasting
TRMM	Tropical rainfall measuring mission
USGS	United states geological survey
UTC	Universal time coordinate
VHRR	Very high resolution scanning radiometer
V_p	Radar beam volume
V_R	Radial velocity
W	Spectrum width
Z/Z_e,	Radar reflectivity factor/equivalent radar reflectivity
Z_h	Horizontal radar reflectivity
Z_v	Vertical radar reflectivity
Z_{bg}	Background reflectivity
Z_{dr}	Differential reflectivity
Z_s	Horizontal gradient of reflectivity
Θ	Horizontal beam width
λ	Wavelength
μ	Shape parameter
Φ	Vertical beam width
Φ_{dp}	Differential propagation phase
Φ_h	Two way phase accumulation at horizontal polarization
Φ_v	Two way phase accumulation at vertical polarization

1

Introduction

1.1. Background

More than 1.7 billion people inhabit South Asia making it the most densely populated region on the Earth. South Asia occupies less than 4% of Earth's land surface area while supports nearly a quarter of the world population. Rainfall received during the summer monsoon season, namely, during 122 days of June to September, is very crucial for the very survival of the people here, in particular to the local agriculture that is able to feed such a huge population. Monsoon rainfall is an outcome of complex interactions and physical process and clouds are central to this. A large number of studies have been and are being carried out addressing the Indian Monsoon (e.g., Rao 1976; Krishnamurti 1985; Webster *et al.* 1998, Gadgil 2003; Mapes *et al.* 2005; Kelly and Mapes 2011; Tyagi *et al.* 2012; Hunt *et al.* 2016, to name a few). The strongest planetary scale circulation during the boreal summer is associated with the South Asian monsoon (e.g., Webster *et al.* 1998). A large number of field campaigns have been carried out targeting the South Asian/Indian monsoon (e.g., Bhat and Narasimha 2007). Despite the major efforts in the past, one important aspect of the Indian Monson, namely, the associated cloud microphysical and dynamical processes remain poorly understood. This study is aimed towards partially filling this knowledge gap using weather radar data.

This chapter is organized as follows. Section 1.2 briefly describes some related studies on clouds and cloud systems followed by the status with respect to the Indian monsoon clouds in section 1.3. Section 1.4 discusses outstanding issues and objectives of the thesis.

1.2. Study of convective clouds

Clouds play key role in Earth's weather and climate. Clouds influence Earth's energy budget by altering both shortwave and longwave radiation (e.g., Ohmura and Gilgen 1993,

Rossow and Zhang 1995; Kiehl and Trenberth 1997). Among different types of clouds, deep convective clouds are the most important ones in the global energy balance because they accomplish vertical transport of energy, water vapor and momentum. Latent heat released in tropical deep convective clouds drives the large scale circulation of the tropical atmosphere and influences Earth's water and energy cycles (Charney 1969; Gill 1980; Zhang and Krishnamurti 1996; Holton 2004). Deep convective clouds are organized at different spatial scales e.g., planetary, synoptic (~1000 km), mesoscale (~100 km) and convective (~10 km) (Houze and Cheng 1977, Nakazawa 1988). Understanding their structure, organization and space-time variation is a frontier area of research in tropical meteorology (Randall *et al.* 2007). Physical processes associated with convective clouds are the largest sources of uncertainty in weather and climate models (Kerr 2009). Clouds involve multi-scale interactions ranging from micro-scale (e.g., cloud condensation nuclei and droplets) to planetary scale. Hence, clouds involve rich physics and are practically source of fresh water on land.

Therefore, the study and understanding of convective clouds is important in the global context too. Information about clouds has been collected in different ways. For example, 1) from visual observation that provides qualitative properties (e.g., cloud shape, texture, cloud base altitude, etc.; *International Cloud Atlas* is a classic example), 2) through *in-situ* observations made with an instrumented aircraft (e.g., Stith 1995; Albrecht *et al*. 1995), and 3) remote sensing. *In situ* observations are expensive and provide data along the track of the aircraft. Owing to aircraft safety considerations, aircraft measurements are not made inside severe thunderstorms and convective clouds. Thus, whilst *in situ* measurements are very useful, these data are biased towards less intense clouds and their spatial and temporal coverage is also limited. Ground weather radars provide information on three dimensional structures of clouds, and the present understanding of the mesoscale organization in deep convective cloud systems came from their data (e.g., Houze and Betts, 1981; Houze 1989; Houze 2004). In a mesoscale convective system (MCS), cumulonimbus (Cb) clouds in various stages of development coexist with anvil cloud formed by the merger of old/decaying Cb clouds (Houze 1989). A spectacular example of MCS organization is seen in squall lines, a propagating MCS with convective precipitation (from Cb clouds) towards the leading edge with trailing stratiform precipitation (from anvil cloud) (Houze 1989). The

stratiform precipitation region is characterized by slow ascent in the upper troposphere (above the freezing level), a prominent melting band (bright band in radar reflectivity field) and wide spread slow precipitation at lower levels. In some cases of MCS, active Cb clouds and stratiform precipitation coexist, but convective cells are randomly distributed within MCS. For example, in the MCSs that form in the Australian monsoon clouds (e.g., Mapes and Houze 1992; Cifelli and Rutledge 1998; Takahashi *et al.* 2008) convective cells embedded within stratiform areas of MCSs are observed, whereas during the break phase, squall line structures are more common. The DWR observations made during the South China Sea Monsoon Experiment (SCSMEX) revealed that the lifetime of MCSs was 6 to 12 hours (Lau *et al.* 2000). Large scale circulations during the summer monsoon onset give rise to the formation of MCS over that region (Ding *et al.* 2006).

A wide range of horizontal scale (linear dimension) is associated with mesoscale, from ~10 km to up to 1000 km in the literature and is further subdivided in to α-, β-, γ-mesoscales (e.g., Orlanski, 1975). The MCSs over East Asia region are of α-scale with average area of more than 123000 km^2 and average lifetime of 4.5 hours (Li *et al.* 2012). During the DYNAMO program (Rowe and Houze 2014), S-band polarimetric radar observations were taken. They observed the enhanced stratiform precipitation in the active phases of MJO. The number frequency of wet aggregates peaks near melting level while dry aggregates are concentrated between 7 and 8 km altitudes. The dry and wet aggregates both peak during rainy days with dry aggregates leading wet aggregates which indicates the transition from convective phase to the stratiform phase.

One of the practical limitations of ground radars is their very limited spatial coverage. Weather satellites have proven to be very powerful tools in the study of convective clouds. Satellites provide information on clouds over the entire globe at high spatial and temporal resolutions. Early satellites mostly measured cloud top properties (e.g., Brightness temperature, OLR and albedo) or column integrated properties (e.g., integrated water vapour amount and cloud liquid water path). Using satellite data, cloud top height, spatial coverage, formation and dissipation, propagation, diurnal variation, etc., have been studied (e.g., Chang 1970; Streten and Troup 1973; Sikka and Gadgil 1980; Velasko and Fritsch 1987; King *et al.* 1992; Waliser and Gautier 1993; Lau and Crane 1995; Wielicki *et al.* 1996; Kummerow *et al.* 1998; Diner *et al.* 1998; Rocca and Ramanathan 2000, Gambheer and

Bhat 2000; Mathon *et al.* 2002; Morel and Senesi 2002; Schmetz *et al.* 2002; Stephens *et al*. 2002; Jirak *et al.* 2003; Rossow and Duenas 2004; Winker *et al.* 2009). Studies based on such data could address two dimensional aspects of clouds at synoptic scale (~O(1000 km), mesoscale (~O(100 km) and microscale (~O(10 m)) (Lin 2007).

The vertical structure of clouds is equally important. Information on the 3D structure of cloud systems over vast areas of the globe was not available until the launch of precipitation radar (PR) onboard TRMM satellite in the year 1997 (Kummerow *et al.* 1998). The PR and the cloud profiling radar (CPR) onboard CloudSat satellite which was launched in the year 2006 (Stephens *et al.* 2002, 2008) provided unprecedented data on convective clouds based on which a large number of studies have been carried out (e.g., Nesbitt *et al.* 2000; Stephens *et al*. 2002; Zipser 2006; Stephens *et al*. 2008; Cetrone and houze 2009; Li and Schumacher 2011; Bhat and Kumar 2015; Kumar and Bhat 2016, to name a few). Based on the analysis of the PR data, Alaca and Dessler (2002) observed that continental convection extends to higher altitudes than oceanic counterparts. Nesbitt *et al.* (2000) and Toracinta *et al.* (2002) showed that continental clouds have greater magnitude of reflectivity extending to higher altitude compared oceanic clouds in the tropics. Toracinta *et al*. (2002) noted that for the oceanic systems, the 40 dBZ reflectivity contour lies mostly below 7 km level, with one third of the systems that do not have the 40 dBZ echo at all. Li and Schumacher (2011) studied the anvil clouds associated with convective cloud systems using 10 years (1998-2007) PR data. Anvil area and echo-top heights were highly correlated with convective rain area and to lesser extent on intensity of reflectivity. The average echo top of anvils identified by the 17 dBZ reflectivity is 8.5 km with an average thickness of 2.7 km. The University of Utah prepared a TRMM Precipitation Features (PFs) data base merging multi sensor data of TRMM satellite (Nesbit *et al.* 2000). This data set has been extensively used to extract properties of tropical cloud systems (e.g., Nesbit *et al.* 2006; Li *et al.* 2008, 2012). Liu *et al*. (2008) compared and contrasted properties of deep clouds (e.g., areal extent) derived from the PR reflectivity and brightness temperatures (T_b) from microwave channels. While T_b criterion shows more frequent deep cloud activity over the west Pacific Ocean, the PR data shows that land masses of central Africa, Argentina and India contain deeper and horizontally more extensive PFs compared to oceanic regions. Xu and Zipser (2012) report that 70-80% of total rain is contributed by storms having 40 dBZ radar echoes reaching

above 6 km over continent regime whereas only 40% monsoonal rainfall and 10% oceanic rainfall involve microphysical processes (e.g. freezing of raindrops, rimming of graupel etc.) in mixed phase regions.

TRMM-PR data has also been used to study regional features of precipitating clouds and individual weather events including tropical cyclones and warm clouds. Houze *et al*. (2007) examined the structure of clouds over the Himalayan region during June-September 2002 and 2003. Deep intense convective echoes with 40 dBZ echo >1000 km^2 in horizontal dimension occurred preferentially just upstream of and over the lower elevations of the Himalayas, most frequently in the northwestern indentation of the barrier. The wide intense echoes (40 dBZ echo>1000 km^2 in horizontal dimension) also occurred along the central portion of the Himalayas, and rarely over the Tibetan Plateau. Pessi and Businger (2009) examined the relationship between lightening and precipitation rate over the North Pacific Ocean. Convective rainfall rate, radar reflectivity, storm height, ice water path show a logarithmic dependence on lightning rate. Cetrone and Houze (2009) studied the anvil cloud structure of MCSs in monsoonal regions and reported that the thick portions of anvils show distinct differences from one climatological regime to another. The thick anvils of West African MCSs have a broad, flat histogram of reflectivity in their upper portions and a maximum of reflectivity in their lower portions. The reflectivity histogram of the Bay of Bengal thick anvils shows a sharp peak at all altitudes with modal values that increase downward. The reflectivity histogram of the maritime continent thick anvils is intermediate between that of the West African and Bay of Bengal anvils. Romatschke and Houze (2011) examined the nature of precipitating clouds associated with the south Asian monsoon. Orography is shown to have a large influence on the type of cloud, for example, precipitation is mainly from small, but highly convective systems along the western Himalayas whereas from stratiform clouds farther east along the foothills. Liu *et al*. (2008) addressed some questions on warm rain clouds and reported that clouds with tops below the freezing level contribute 20% and 7.5% of the total rainfall over tropical oceans and land respectively, a large fraction of which are not independent but attached to deep cloud systems.

Very few studies are carried out using both the PR and CPR data. Cetrone and Houze (2009) studied the differences between maritime, continental and oceanic MCSs using the

PR and CPR data for one monsoon season in 2006-2007. They examined precipitating convective and stratiform regions of MCSs using the PR data, whereas, for the non-precipitating part of anvil clouds (identified using the criterion radar reflectivity factor <-10 dBZ below 5 km) CPR data was used. Below the freezing level, West Africa and Bay of Bengal MCSs are found to have the highest and the lowest modal reflectivity, respectively. In their upper portions, the thick anvils of West Africa MCSs have a broad, flat histogram of reflectivity, while corresponding case over the Bay of Bengal has a sharply peaked distribution. For thick anvils (now using the CPR data), the mode of radar reflectivity is around -5 dBZ at 9 km for Bay of Bengal clouds while for West African clouds, it occurs at ~0 dBZ at 8 km. It may be noted that although Cetrone and Houze (2009) use the PR and CPR reflectivity products, but the two are not compared. Yuan *et al.* (2011) delineated the differences in CFADs (contoured frequency by altitude diagrams) of continental and oceanic regions. For thick anvil clouds, CFADs of radar reflectivity over continental regions are broader and have high reflectivity mode at 10 km compare to that obtained over oceanic regions. Li and Schumacher (2011) studied the anvil clouds associated with tropical deep convection, and found that the anvil cloud top height obtained from the PR data are underestimated by ~5 km compare to that obtained from CPR data.

Vertical profiles of heating associated with convective and stratiform clouds have distinctly different shapes (Houze 1982, 1989). The large scale circulation responds to the resultant heating profile, i.e., the area weighted average of convective and stratiform heating over the life span of MCSs (Houze 1989). Thus, information on the relative contributions of convective and stratiform precipitation during MCS's life cycle is useful which requires that convective and stratiform echoes are identified. Convective area fraction (CAF, i.e., fraction of the total cloudy area covered by convective rain) and convective precipitation fraction (CPF, convective precipitation to the total precipitation ratio), and its counterpart, namely, stratiform precipitation fraction (SPF) (e.g., Steiner *et al.* 1995) are some of the measures used to quantify their relative contributions. CAF and CPF have been derived from both ground based Doppler radar data (e.g., Steiner *et al.* 1995; Guy *et al.* 2011) and spaceborne radar data (e.g., Schumacher and Houze, 2003a). Analysis of the PR data shows that SPF varies in the range 20% to 65% in the tropical belt 20°S to 20°N with its values over oceanic regions being larger compared to that over the continents (Schumacher and Houze 2003).

1.3. Study of monsoon clouds

India Meteorological Department (IMD) has been operating weather radars since 1952, using which some studies have been carried out (Abhilash *et al*. 2007; Chatterjee *et al*. 2008; Mukhopadhyay *et al*. 2009). Since early 2000, IMD started operating DWRs at few stations however data were not publicly available for long. In the absence of IMD DWR data, information on monsoon clouds in South Asia has mainly come from the analysis of satellite data.

The PR data has been extensively used for monsoon cloud studies (Nesbitt *et al*. 2000; Houze 2007; Liu *et al*. 2008; Liu and Zipser, 2008; Li and Schumacher 2011; Bhat and Kumar 2015 etc.) while the CPR data to a limited extent (Zhang *et al*. 2007; Luo *et al*. 2008; Yuan *et al*. 2011; Rajeevan *et al*. 2012 etc.). Studies of MCS over the South Asian region are carried out using INSAT pixel level data (Laing and Fritsch 1993; Gambheer and Bhat 2000, Roca and Ramanathan 2000) and numerical simulation experiments using regional models (e.g., Das *et al*. 2006; Rao *et al*. 2007). Gambheer and Bhat (2000, 2001) carried out a detailed study of the life cycle characteristics of MCS over the Indian region including the size and number distribution, regions of formation and dissipation, propagation characteristics, diurnal variation, etc., using 3 hourly IR (infrared) imageries for April 1988-March 1989 period. About 20%-40% of CSs have life spans less than 6 hours, while a few systems live for more than 24 hours. The mean speeds of propagation of CSs varied in a narrower range of 7 to 9 m s^{-1}, which is much less when compared to systems over the Atlantic Ocean. There is also strong diurnal variation across the Indian sub-continent, head Bay of Bengal, and equatorial and southern Indian Ocean. Morning and early noon are found preferred time of convection over the head bay region while convective activity peaks during late night and early morning hours over other parts of the Indian Ocean (Gambheer and Bhat 2000, 2001). There have been a few studies on MCSs over the Indian region India using radar observations (Houze and Churchill 1987; Webster *et al*. 2002). During JASMINE (Joint Air-Sea Monsoon Interaction Experiment) carried out over the equatorial Indian Ocean and southern Bay of Bengal during April-May of the year 1999 radar measurements of cloud systems were made from the American research ship Ron Brown (Webster *et al*. 2002). The results seem to indicate that MCSs over the Bay have structures broadly similar to those observed over the tropics.

Combining disdrometer and MST (Mesosphere-Stratosphere-Troposphere) radar data collected at Gadanki (13.5°N, 79.2°E), Rao *et al.* (2001) conclude that 54%, 12% and 34% of the total precipitation result from convective, stratiform and transition stages, respectively. CPF values are less in the southern parts of India and more in the north and towards the foothills of the Himalayas (Pokherel and Sikka, 2013; Saikranthi *et al.* 2014). Pokhrel and Sikka (2013) showed that CPF varied from ~40% to more than 75% over the Indian region, with higher values occurring near the foothills of the Himalayas. Saikranthi *et al.* (2014) estimated that the CPF values over the northwes India is 64% and it decreases when moves towards the central India (~47%) and west coast of India (~34%). Rajeevan *et al*. (2012) examined the vertical structure of Indian monsoon clouds using CloudSat retrieved products. They showed that the deep convective clouds have large vertical extent (~14 km) over the South Asian monsoon region. They also observed the large cloud water/ice content over the North Bay of Bengal region.

1.4. Objectives

What has been said in the earlier sections is a miniscule of a large body of literature on tropical clouds including that of the South Asian monsoon. Next I briefly summarize what is known about tropical clouds (without giving references for the sake of brevity). Initial understanding of MCS came from GATE observations. Subsequent studies have supported the idea that MCS possesses a structure that is nearly universal, i.e., they contain a region of active cumulus and cumulonimbus (Cb) clouds and a connected anvil region (formed by the merger of old Cb clouds) with well separated updrafts and downdrafts. MCS passes through a life cycle of growth, mature and decay stages. Life span of MCSs can vary from few hours to more than a day. Within a geographic region, MCSs have preferred places of formation, they propagate and eventually decay, all tied up with the diurnal cycle. The nature of the tropical MCSs over continental and oceanic regions is different in terms of their vertical structure. The CAF and CPF values show large variation between ocean and continental areas, and also between active and break phases of the monsoon. The properties of (deep) cloud systems associated with the South Asian monsoon have been investigated using satellite measured infrared brightness temperature data as well as the PR data. The former

mainly refers to the properties of cloud top, whereas the latter also provides cloud vertical structure.

Despite the simplicity of conceptual model of MCS (e.g., Houze 1981, 1989), MCSs still remain among the most important and difficult to understood problems in atmospheric sciences. The main reason being, deep clouds form under a variety of environmental conditions which strongly influence the cloud droplet nucleation and precipitation processes. Differences in synoptic conditions and local surface characteristics also add to natural variability in clouds. Some problems, especially if one considers regional characteristics of MCSs, remain to be addressed. For example, temporal evolution of the three dimensional structure of MCSs remains unknown over the South Asian region despite the critical role of monsoon clouds to the economy of the region. For the geographic region investigated in the present study, namely, the main monsoon zone over the Indian sub-continent (land area north of 18º N and to the south of the Himalayas), no study exists on CPF/SPF estimates derived from DWR data.

The global coverage of the PR comes at the cost of a sampling time interval of several hours. Hence the PR is not suited to study the temporal evolution of MCSs which ideally requires data of ground weather radars. The latter was not publicly available over the Indian region for a long time. This work started in 2011, and in the absence of IMD's DWR data, idea was to use available PR and CPR data to understand the vertical structure of MCSs embedded in South Asian monsoon cloud systems. Past studies using the PR data had looked at the Indian monsoon clouds including that in the Himalayan region, but study on cloud systems over the Tibetan Plateau was missing. Tibetan Plateau plays a key role in the Indian monsoon (Rao 1976), but the nature of cloud systems there was not known. So, I started with the study of cloud systems over this region using the PR and CPR radar reflectivity (Z_e) data. As shown in Chapter 3, while nice looking vertical structures of deep cloud systems are seen there, some major differences exist between the vertical profiles of Z_e obtained from the PR and the CPR data. In the meantime, IMD DWR data became publicly available for the monsoon seasons of 2012 and 2013, and I decided to base my work on the analysis of this data. Accordingly, the main objective of the present work also shifted but the focus remained on the vertical structure and temporal evolution of MCSs in monsoon clouds.

Important objectives of the thesis work are as follows.

1) Vertical structure of clouds over the Tibetan Plateau using the PR and the CPR data.

2) Identify the convective echoes in MCSs over Indian monsoon zone, their temporal evolution and quantify their contribution to the total area cover and precipitation and interconnection between storms and MCSs.

3) Understand differences in MCSs that form in different climatic regimes.

4) Explore storms embedded within MCSs and their important properties

5) Estimate precipitation amount and cloud liquid water content in monsoon clouds using radar reflectivity data and polarimetric variables.

Following is the structure of the thesis: The second chapter briefs about data and methods used in the present study. The third chapter covers the study of Tibetan Plateau clouds using spaceborne radar observations followed by a comparison of the PR and CPR Z_e data. The fourth chapter reports the temporal evolution of MCSs and their interconnection with the storms (embedded within them) at five different locations of the Indian monsoon zone. The fifth chapter reports an analysis of C-band polarimetric radar data to study convective storms (e.g., duration, size, height, speed and direction of movement etc.) and precipitation accumulation and cloud liquid water content estimates. Chapter 6 summarizes the work.

2

Data and Methods

In this chapter, the data and methods used in the thesis work are described. Section 2.1 gives detailed information about the data taken from spaceborne and ground instruments. Section 2.2 briefs about data quality control followed by definitions of MCS and storm. Sections 2.3 to section 2.8 discuss methods of analysis.

2.1. Data

2.1.1. Spaceborne instruments

Data from two types of spaceborne sensors are used in the study, namely, a) weather radar, and 2) brightness temperature from Indian geostationary satellite Kalpana-1.

2.1.1.1. CPR and PR

The PR and CPR are two spaceborne weather radars flying in space since 1997 and 2006, respectively. Their technical specifications are given in Table 2.1. The PR is a Ku-band radar (wavelength 2.2 cm; frequency 13.8 GHz) on board non-sun-synchronous satellite TRMM at an altitude of 402.5 km (post orbit boost in August 2001, and the orbit height was 350 km when launched in 1997) from the Earth's geoid (Kummerow *et al*. 1998; Kummerow *et al*. 2000). The TRMM is a joint venture between NASA and JAXA. The TRMM's orbit covered the latitude range from 38°S to 38°N, and having a non-sun-synchronous orbit, it visited a geographic region several times a day (the number of visits is a function of latitude (see e.g. Kummerow *et al*. 1998 and Chapter 3). Of interest to this study are PR's spatial coverage and measurement capabilities in clouds. This work uses PR data for the July 2006 to December 2010 period and hence I consider the PR characteristics for this period only. The PR has a swath of 250 km, made of 49 beams of 0.7^{o} width with a foot print size of 5 km in the horizontal at zenith and vertical resolution of 0.25 km and 80 vertical levels. The basic measurement of the PR is the equivalent radar reflectivity factor Z_e (defined in Section

2.1.2.1). The dynamic range of the PR is ~70 dBZ with the minimum detectable signal strength of ~17 dBZ. The CPR is W-band (wavelength 3.2 mm; frequency 94 GHz) radar on board NASA's A-Train (polar orbiting sun-synchronous) satellite constellation at an altitude of 705 km. Swath width of the CPR is 1.4 km and its vertical resolution is 0.24 km. Its minimum detectable signal strength is -29 dBZ and dynamic range is ~70 dBZ. Thus common measurement range of the PR and the CPR is from 17 to 41 dBZ.

2.1.1.2. Kalpana-1 satellite

Kalpana-1 satellite is the first geostationary meteorological satellite launched by Indian Space Research Organisation in the year 2002 (http://www.isro.gov.in/Spacecraft/Kalpana-1). It features very high resolution scanning radiometer (VHRR) having three channels namely visible, thermal infrared (TIR) and water vapor bands with spatial resolutions of 2 km at nadir for visible and 8 km for TIR and water vapor channels with temporal resolution of 30 minutes at the altitude of 35,786 km above Earth's surface. The main datasets provided by Kalpana-1 satellite are infrared brightness temperature (T_B) and outgoing longwave radiation (OLR).

Table 2.1. Technical specifications of CloudSat CPR and TRMM PR.

Characteristics	CloudSat CPR	TRMM PR
Frequency, GHz	94	13.8
Pulse Width, µsec	3.3	1.6
Pulse Repetition Frequency, Hz	4300	2776
Minimum Detectable Signal, dBZ	-29	17 (18)*
Dynamic Range, dBZ	~70	≥70
Vertical Resolution, m	240	250
Cross-track foot print, km	1.4	4.3 (5.0)*
Along-track foot print, km	2.5	4.3 (5.0)*
Swath width, km	1.4	217 (247)*

* TRMM orbit height was boosted from 350 km to 403 km in August 2001. Numbers inside the brackets correspond to post orbit height increase.

2.1.2. Ground-based instruments

2.1.2.1. Non-polarimetric DWR

DWR is the best known active device to observe cloud properties in 3-dimensional space with high temporal resolution (typically one radar volume scan every 10 minute). IMD operates several DWRs in different parts of India. Data of available DWRs were made accessible to research community in India for the summer monsoon seasons of 2012 and 2013 under the CTCZ (Continental Tropical Convergence Zone) program (a sub-program of the Indian Climate Research Programme). The main objective of the CTCZ programme is to understand the space-time variation of precipitation over the monsoon zone (CTCZ, 2009).

The present study uses DWR data collected during the 2013 monsoon season. Requiring good temporal continuity of data, I selected five DWR stations meeting the requirements, namely, Delhi (DLI), Hyderabad (HYD), Kolkata (KOL), Nagpur (NGP) and Patiala (PTL) (Figure 2.1). The technical specifications of DWRs are given in Tables 2.2 and 2.3. IMD procured two Vaisala C-band polarimetric DWRs in the year 2010 and installed them at Delhi (28.6°N, 77.2°E) and Jodhpur (26.2°N, 73°E). The non-polarimetric radar has single polarization and gives radar reflectivity (Z_e: a proxy for the hydrometeor concentration in clouds; Houze 2014, pp. 83) radial component of Doppler velocity (V_R: component of velocity of target along the radar beam) and spectrum width (W: distribution of velocities within single radar volume).

One of the primary products of a DWR is the radar reflectivity factor (Z) which is proportional to the 6th moment of the diameter of hydrometeors present in the sampling volume (Houze 2014, pp 83). Z is given by (e.g., CIMO 2008)

$$Z = \frac{\sum_i D_i^6}{V_p} = \frac{1024(2\ln 2)}{10^{-18}\pi^3 c}\left[\frac{\lambda^2}{P_t \tau G_o^2 \Theta\Phi}\right]\left[\frac{r^2 \overline{P_r}}{|K|^2}\right], \quad (2.1)$$

where V_p is radar beam volume, D_i diameter of hydrometeors occupying the volume, c speed of light, λ radar beam wavelength, P_t transmitted power, G_o radar antenna gain, K dielectric constant of water, r the range (distance between antenna and target), Θ and Φ radar beam width in horizontal and vertical and τ is radar pulse duration. Few key assumptions are made while deriving Eqn. (1), important ones being (*a*) beam intensity attenuation caused by the atmospheric constituents (gaseous and hydrometeors when present) is negligible, and (*b*)

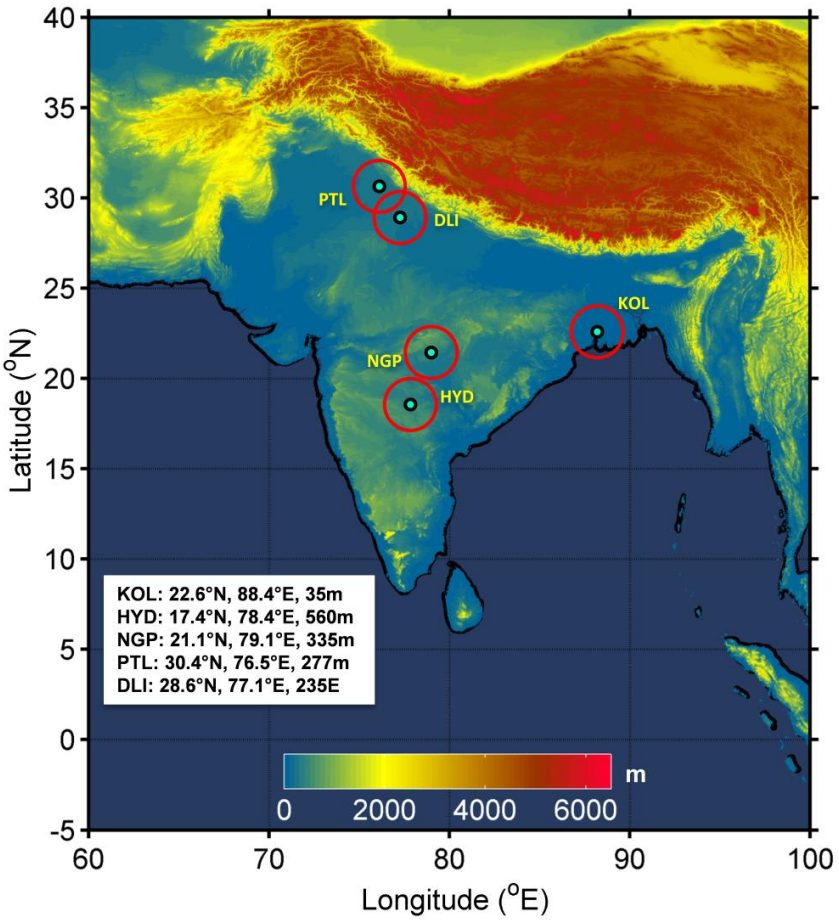

Figure 2.1. Geo-locations of S-band DWRs overlaid USGS global 30 arc-second terrain elevation. Radius of the outer circle around each radar location is of 150 km. Abbreviations used here are the following: DLI-Delhi, HYD-Hyderabad, KOL-Kolkata, NGP-Nagpur, PTL-Patiala.

scattering by cloud drops/droplets is Rayleigh (CIMO 2008). When attenuation is not negligible, corrections are applied while Z is given out as a product (Iguchi and Meneghini 1994; Testud *et al*. 2000; Gorgucci and Chandrasekar, 2005). The definition of Z accounts for differences in λ, antenna characteristics, transmitted power, and distance of target from the radar, hydrometeor type, etc. Sampled volume may contain liquid, ice, melting ice particles or mixture of these depending on the conditions of the cloud. In ordinary radar measurements, the numbers of particles, composition and shape are not known and an *equivalent radar reflectivity factor* (Z_e) is defined by assuming that the backscattering particles are spherical water drops. For single polarized radars, Z_e is given as a product, and it is implicitly understood that it is property of a cloud, in particular, a measure of the amount of condensed water per unit volume (Houze 1993). It is observed from Eqn. (2.1) that Z is defined in two

ways, namely, the 6th moment of the hydrometeor diameters per unit sampling volume, and from radar hardware characteristics, returned power P_r and phase of hydrometeors in the sampling volume. The former is uniquely defined for a given drop size distribution (DSD, $N(D)$), i.e., number of hydrometeors between diameter D and $D+dD$ in a unit volume of cloud air which is given by

$$\mathrm{Z} = \int_0^\infty N(D) D^6 dD. \tag{2.2}$$

The latter is measured by the radar assuming hydrometeors to be liquid drops. Rain rate R (see Doviak and Zrnic 2006) is given by

$$\mathrm{R} = \frac{\pi}{6} \int_0^\infty N(D) D^3 w dD \tag{2.3}$$

where w is the fall speed of the hydrometeors which is a function of diameter D and air density (Gun and Kinzer 1949). Hence for a given DSD, Z and R are uniquely related, and this forms the basis of the reflectivity-rainfall (Z-R) relationships (Marshall and Palmer, 1948) which does not explicitly include radar characteristics.

2.1.2.2. Polarimetric DWR

Details of polarimetric radar can be found in Bringi and Chandrasekhar (2001) and Doviak and Zrnic (2006). Briefly, a polarimetric radar sends beams that are horizontally and vertically polarized, and from the returned signals received in two polarizations, polarimetric variables are calculated. A polarimetric DWR gives separate Z values corresponding to power transmitted in both horizontal and vertical polarizations (namely Z_h and Z_v). When hydrometeors present in sampling volume are non-spherical, then the two beams experience different hydrometeor cross sections, path lengths in condensed water, etc. A polarimetric DWR provides three important variables in addition to Z and radial component of Doppler velocity. (a) Differential reflectivity (Z_{dr}) which is defined as the difference between horizontal and vertical reflectivity in dBZ units. It is expressed in decibel (dB) unit. The expression for Z_{dr} is $Z_{dr} = 10\log_{10}\left(\frac{Z_h}{Z_v}\right)$; If Z_{dr} is positive then it indicates that the hydrometeors are horizontally oriented while negative values show vertical orientation of

Table 2.2. Geo-locations of the S-band DWRs, their technical specifications, scan angles and data availability.

Specifications	**Station**				
	KOL*	HYD*	NGP*	PTL*	DLI*
Geo-location (Lat*, Lon*, Alt*)	(22.6°N, 88.4°E, 35 m)	(17.4°N, 78.4°E, 560 m)	(21.1°N, 79.1°E, 335 m)	(30.4°N, 76.5°E, 277 m)	(28.6°N, 77.1°E, 235 m)
Wavelength (cm)	10.43	10.52	10.43	10.52	10.62
Scan elevations (°)	0.2°/0.49°, 0.99°, 1.99°, 2.99°, 4.49°, 5.99°, 8.99°, 12°, 16°, 21°				
Azimuths (°)	0° - 359°				
Gate Size (m)	500	500	250	500	250
Beam Width	1°				
No. of volume scans	355	202	337	377	97
Date of Available MCSs	20-Aug-2013 21-Aug-2013 02-Sep-2013	03-Jun-2013 05-Jun-2013	10-Jun-2013 13-Jun-2013 23-Jun-2013	11-Jun-2013 08-Jul-2013 08-Aug-2013	13-Jun-2013 14-Jun-2013

**Abbreviations Lat, Lon, Alt, KOL, HYD, NGP, PTL and DLI refer to latitude, longitude, altitude, Kolkata, Hyderabad, Nagpur, Patiala and Delhi respectively. Abbreviations Jun, Jul, Aug and Sep refer to June, July, August and September respectively.*

Table 2.3. Specifications, provided products and data availability of C-band polarimetric DWR.

Specifications	
Geo-location (Lat, Lon, Alt)	28.6°N, 77.2°E, 253 m
Wavelength	5.33 cm
Scan elevation angles	0.49°, 0.99°, 1.99°, 2.99°, 4.49°, 5.99°, 8.99°, 12°, 16°, 21°
Azimuths	0° -359°
Gate Size	300 m
Beam Width	0.95°
Products used	Z_h, Z_{dr}, K_{dp}
Data used	10-June-2013, 11-June-2013, 13-June-2013, 14-June-2013, 15-June-2013, 16-June-2013

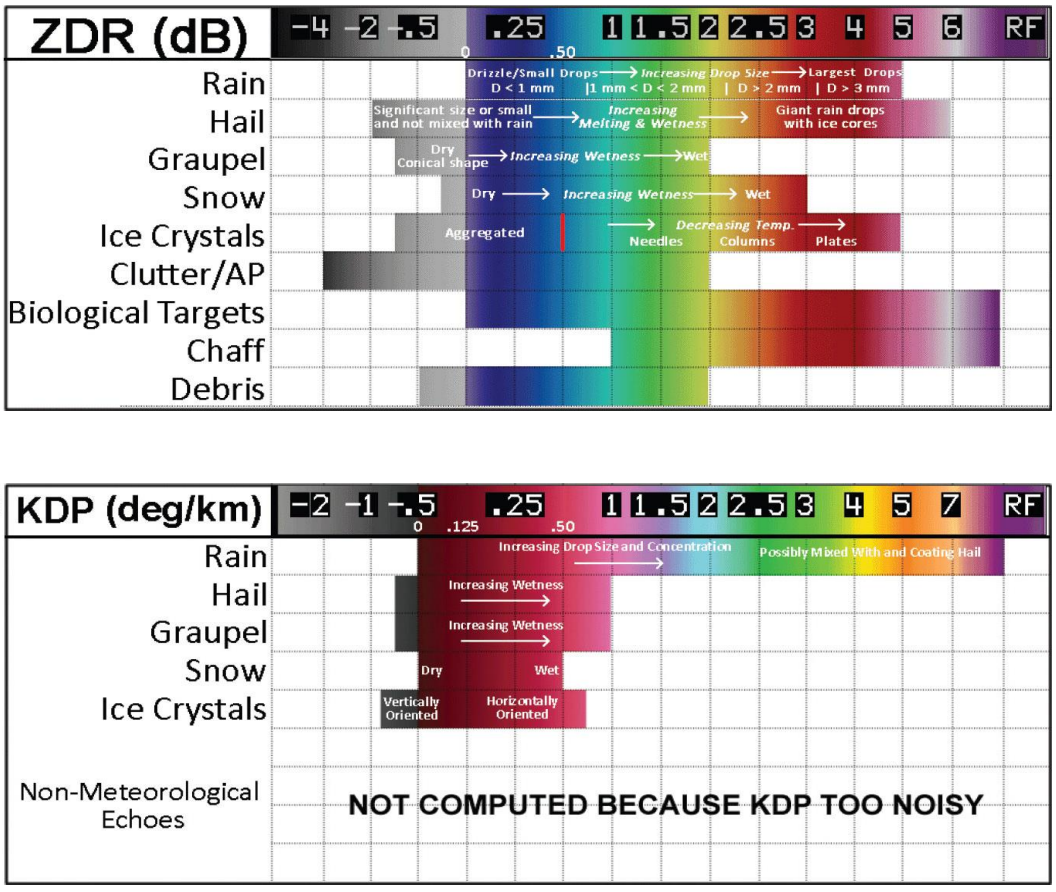

Figure 2.2. Typical ranges of Z_{dr} and K_{dp} and corresponding target characteristics (Courtesy: National Weather Service, USA).

hydrometeors in cloud volume. b) Differential propagation phase Φ_{dp} (=Φ_h - Φ_v), which is the phase difference between horizontal and vertical polarized returned signals. c) Specific phase (K_{dp}): It is range derivative of differential propagation phase i.e.,

$$K_{dp} = \left(\frac{\phi_{dp}(r_2) - \phi_{dp}(r_1)}{2(r_2 - r_1)} \right) \tag{2.4}$$

The K_{dp} has unit in deg km^{-1}. It is independent to attenuation and less sensitive to variations in drop size distributions (DSDs) compared to Z_h. The main advantage of a polarimetric DWR is that it not only measures hydrometeor concentration but also characterizes the hydrometeor type. Some typical examples of hydrometeor types provided by National Weather Service (NWS), USA are shown in Figures 2.2. It can be noticed that interpreting hydrometeor type from Z_{dr} and K_{dp} is not trivial and often combined with additional information (e.g., altitude of zero degree isotherm, cloud base height, etc.) to characterize hydrometeors more accurately.

A snap shot of clouds sampled by the polarimetric radar at Delhi is shown in Figure 2.3. It shows the projection of columnar maximum radar reflectivity Z_h (top panel), differential reflectivity Z_{dr} (mid-panel) and specific differential phase K_{dp} (bottom panel) observed on 11 June at 0712 LST. The corresponding vertical sections taken along line AB are shown in panels (b), (d) and (e), respectively. The color bars on right refer to Z_h (in dBZ), Z_{dr} (in dB) and K_{dp} (in deg km^{-1}), respectively. Vertical section (Figure 2.3 b) does not show the presence of a melting layer suggesting that the MCS was in the development/growth stage at that time instant. Z_{dr} varied in -0.5 to + 3 dB range (Figure 2.3 c, d). A positive Z_{dr} implies an oblate object with larger size in the horizontal. However, associating a given Z_{dr} with hydrometeor type is not trivial (Fig 2.2). For example, large rain drops, wet graupel and wet snow can have a Z_{dr}> 0 dB (Ryzhkov and Zrnic, 2006). K_{dp} is sensitive to oriented oblate rain drops while spherical hailstones do not contribute to K_{dp} (Bringi and Chandrasekar, 2001. pp 390). Generally higher K_{dp} values correspond to areas of heavy rain or the presence of ice crystals, while light rain and aggregated dry snow have small K_{dp} (Ryzhkov and Zrnic, 2006). Z_h>45 dBZ, Z_{dr}>1 dB and K_{dp}>2 deg km^{-1} together imply that heavy precipitation dominated by large rain drops were present at this time in the lower troposphere. K_{dp}>2 deg km^{-1} and Z_{dr} ~ 0 dB suggest the dominance of ice crystals in the upper troposphere in areas away from deep clouds and nearer to location B (Figure 2.3 e, f).

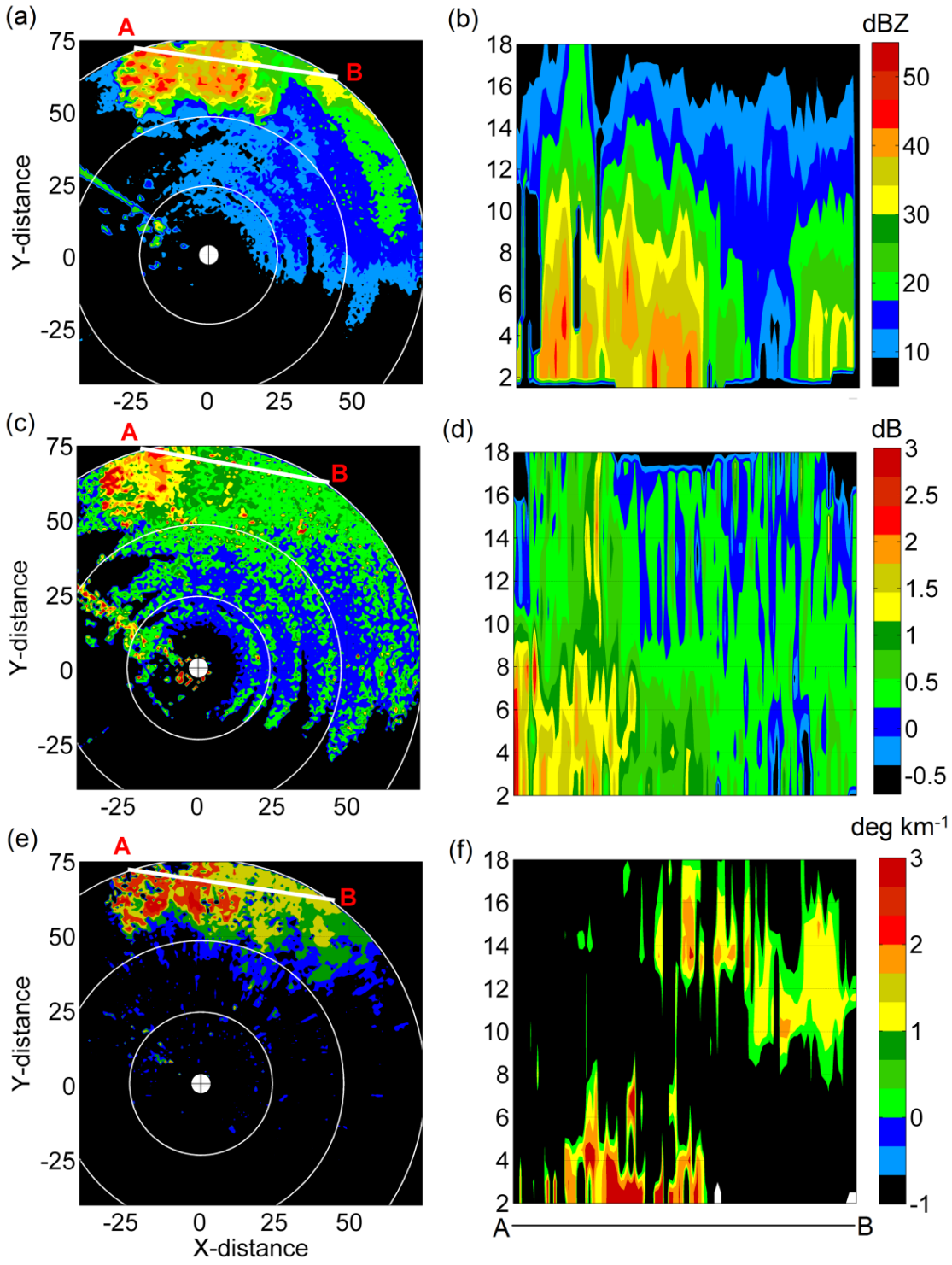

Figure 2.3. Projection of column maximum of radar reflectivity Z_h, differential reflectivity Z_{dr} and specific differential phase K_{dp} are shown in panels (a), (c) and (e) respectively observed on 11 June at 0712 LST. The corresponding vertical sections taken along line AB are shown in panels (b), (d) and (e), respectively. The color bars on right refer to Z_h (in dBZ), Z_{dr} (in dB) and K_{dp} (in deg km^{-1}) respectively.

2.2. Quality control of DWR data

Except for the DWR at Kolkata (manufactured by Selex ES GmbH Germany and installed in 2002), other DWRs (manufactured by *Beijing Metstar Radar Co., Ltd, China)* are new and installed in or after 2011. IMD follows a regular calibration procedure, and the main steps include internal calibration (linear receiver calibration, phase calibration along with monitoring of transmitter peak power and system noise once every volume scan cycle) and (external) sun calibration (http://metnet.imd.gov.in/projects_doc/sop_dwr.pdf). Further, Z_e data are passed through a quality check procedure to remove possible noisy echoes. Data within 150 km range of radar are only considered to avoid super refraction and radar beam widening effects (which increase with radar range, e.g., Booker, 1946; Donaldson, 1970). Z_e values below 1 km altitude are discarded to avoid the contamination by echoes generated from multiple reflections from ground (Fabry, 2015, pp. 55). Echoes having their radial component of velocity $V_R = 0$ all the time correspond to reflections from fixed objects (such as tall buildings and mountains) and have been removed using clear sky echoes.

Radar volume scan data is available every 10 minutes and is in the spherical polar co-ordinate system. Original Z_e values are converted to three-dimensional (3D) Cartesian co-ordinate gridded data using *Radx*-algorithm (version 20141125) developed at the Research Applications Laboratory, National Centre for Atmospheric Research, USA (Dixon, 2014). Re-gridded data have 40 vertical levels, each separated by 0.5 km, and the horizontal pixel size is 2 km × 2 km.

2.3. Definition of mesoscale convective system

Cumulonimbus (Cb) cloud systems exist in a hierarchy of scales and the most studied among them is mesoscale. Mesoscale spans a large range in horizontal dimension (from less than 10 km to more than 1000 km, e.g., Orlanski, 1975). Houze (2004) defined MCS as a cumulonimbus cloud system that produces a contiguous precipitation area ~100 km or more in at least one direction. For the present study period, it was observed that the number of cases satisfying this criterion is few, and thus not convenient to study the temporal evolution of Cb cloud systems. Basically, the early evolution stage of MCS is missed. After some trial, following procedure is adapted for identifying cloud systems from the re-gridded radar reflectivity data. A pixel is identified as cloudy if Z_e>10 dBZ, a value well above the DWR

noise level within 150 km radar range. Columnar maximum value of Z_e is projected onto a horizontal plane. In this projection, connected cloudy pixels having an area of at least 1600 km^2 and containing at least one pixel with $Z_e \geq 30$ dBZ are identified. No condition is put on the shape of the area. The identified MCS is tracked and included in the study if the system lasted for at least two hours. Its linear dimension exceeds 40 km in at least one direction which falls in the meso-β scale range according Orlanski (1975), and a cloud systems identified with the above procedure is called an MCS. It may be noted that precipitation feature (PF) is another term often used in the study of convective clouds using the PR (e.g., Nesbit *et al*. 2006) and DWR (e.g., Lang *et al*. 2007) data. For example, Nesbit *et al*. (2006) fit an ellipse that encompasses connected cloudy pixels and take twice the length of the major axis as its linear dimension, a definition also followed by Lang *et al*. (2007). For the present MCS, if an ellipse were to be fitted to the area and twice the major axis taken as its size, then that number would come close to Houze's (2004) minimum size criterion. Owing to its limited range, radar might have sampled a portion of a large MCS and including such cases in the analysis is not desirable. A case study was carried out with DWR and Kalpana-1 satellite T_B data when both are simultaneously available. Contour lines of T_B were projected onto radar's maximum Z_e map (Figure S1). Examination of several such plots revealed that the best area overlap between CSs derived from radar and satellite data occurs for the latter's contour defined by $T_B = 220$ K. An MCS is included for a detailed analysis if good overlap is visually observed between radar and satellite data derived cloud systems. This, along with the life span criterion of at least two hours, reduced the total number of MCSs that could be studied to 13 (2 each at Delhi and Hyderabad, and 3 each at Kolkata, Nagpur and Patiala). Sample structures of MCSs are shown in Figures 2.4 and 2.6.

2.4. Convective echos identification algorithm

The maximum updraft speed inside a cloud characterizes if it is convective or stratiform type (Houze 2014, 142-143 pp.) with the former having higher (>5 m s^{-1} during growth and early mature stages) and the latter having lower (typically <1 m s^{-1}) values. Operational DWR scan elevations (e.g., the maximum elevation angle is 21° in IMD's volume scans, see Table 2.2 and 2.3) are not suitable for deriving updraft speeds. Hence, the precipitation type is

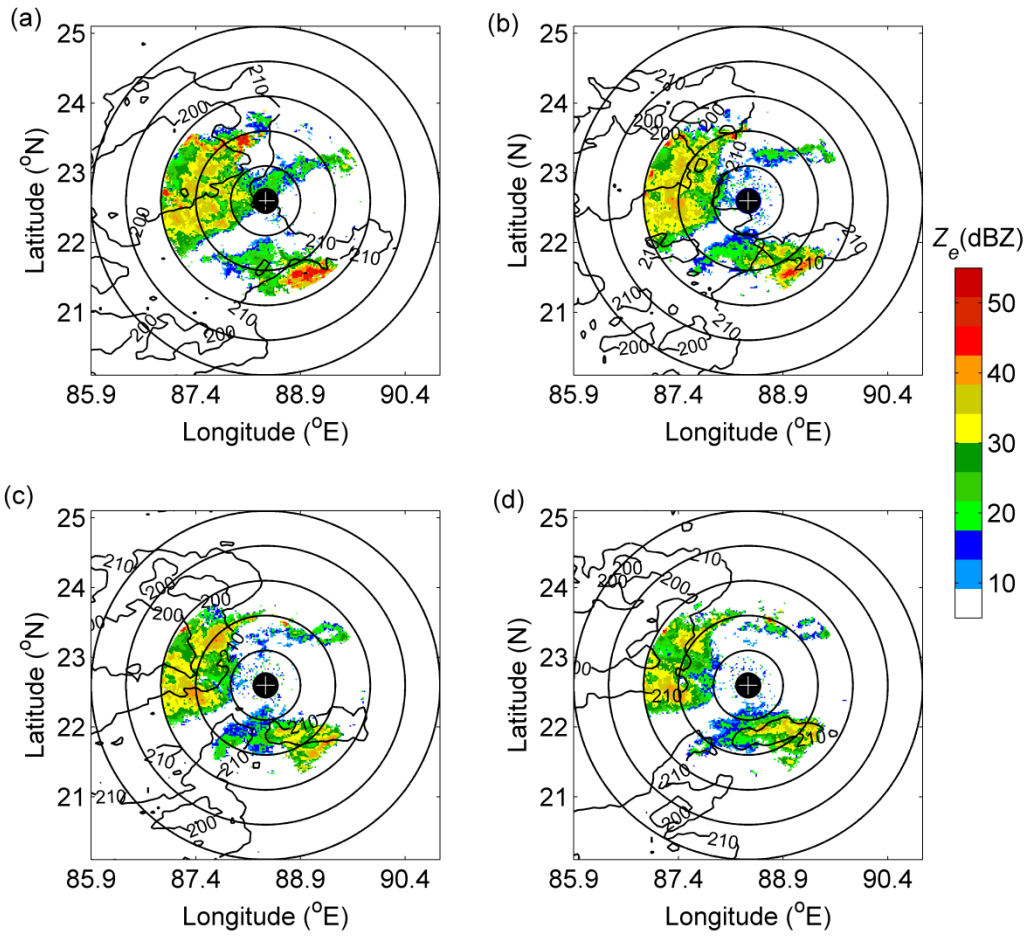

Figure 2.4. Contour lines of infrared brightness temperature overlaid onto the horizontal projection of the maximum Z_e of all vertical levels for an MCS observed over Kolkata on 2 September, 2013. Different plots correspond to time (a) 0730 UTC, (b) 0800 UTC, (c) 0830 UTC, and (d) 0900 UTC.

inferred from the Z_e field. There are several algorithms discussed in the past studies which are used to identify convective and stratiform precipitation types from operational DWR measurements. These utilize certain features of the Z_e field normally associated with MCSs. For example, the stratiform part of an MCS contains a melting layer/bright band (e.g., Houze 2004). Compared to the stratiform portion of MCSs, the convective portion contains higher amount of hydrometeors per unit volume (and therefore high Z_e). Furthermore, convective ascents are confined to relatively narrow areas (Houze 2014, pp. 152). High values of Z_e (away from the melting band) as well as larger horizontal gradients in Z_e characterize convective clouds. Algorithms for identifying convective and stratiform precipitation pixels make use of one or more such features of the Z_e field. A few of the CS-algorithms used the bright band method to identify stratiform precipitation (e.g., Rosenfeld *et al.* 1995). Some early studies

on CS classification used a fixed threshold for Z_e, and pixels with Z_e above a prescribed threshold value are declared as convective and the remaining pixels become stratiform (e.g., Houze 1973; Churchill and Houze 1984; Steiner and Houze 1993). Steiner *et al.* (1995) added a peakedness criterion in which pixels having their Z_e below the threshold but stand out compared to their immediate neighbors are also treated as convective. Biggerstaff and Listemaa (2000) considered the bright band fraction (BBF) and horizontal (∇_H) and vertical (∇_z) gradients of Z_e to classify convective and stratiform echoes.

The present algorithm has been developed taking further the ideas proposed in Steiner *et al.* (1995) and Biggerstaff and Listemaa (2000). To begin with, a 2-dimensional (2D) map of Z_e field is constructed for each volume scan by taking the maximum Z_e between 2 and 3 km altitudes (includes 2, 2.5 and 3 km levels of the re-gridded data) at each horizontal grid of the cloud system (Figure 2.5). It may be noted that high Z_e values are not uncommon in the bright band (i.e., stratiform) region of an MCS. To avoid sampling near the melting level (which is typically between 4 and 6 km over the study area during the summer), the 2-3 km height band has been chosen for the 2D map. Convective clouds are highly transient and hydrometeors concentration at any given level changes with time. Basing the CS separation on an instantaneous Z_e field at one fixed height may not correctly reflect the true convective nature of the cloud system. Hence the present algorithm combines information from three levels. Convective pixels are identified from the following three steps.

1) A pixel with $Z_e \geq 40$ dBZ is taken as convective (follows Steiner *et al*. 1995).

2) Apply the background reflectivity (BG) criterion (follows the spirit of Steiner *et al*. 1995).

For each pixel with $Z_e < 40$ dBZ, mean of nonzero echoes (Z_{bg}) within a rectangular area of 484 km^2 and containing the pixel at the center is calculated. Let $\Delta Z_e = Z_e - Z_{bg}$. Pixels satisfying the criterion $\Delta Z_e > 10 - Z_{bg}^2/180$ ($0 \leq Z_{bg} < 40$ dBZ) are treated as convective.

3) Horizontal gradient criterion (follows Biggerstaff and Listemaa 2000). For the remaining pixels, horizontal gradient of reflectivity (Z_s) is calculated from the equation,

$$Z_s = \left| \sqrt[2]{Z_x^2 + Z_y^2} \right| \tag{2.5}$$

where Z_x ($=\partial Z/\partial x$) and Z_y ($=\partial Z/\partial y$) are gradients (calculated using central difference m*eth*od) along *x*- and *y*-directions, respectively. A pixel is considered convective if its $Z_s \geq 3.5$ dBZ km^{-1}. This threshold value was arrived at after visually examining horizontal and vertical sections of several MCSs and seeking good agreement between manual judgment and what the algorithm gives. Sum of the pixels obtained from the above three steps gives the total number of convective pixels in the 2D map, and along with their entire column of cloudy pixels constitute convective part of the cloud system. The remaining pixels (and columns) are treated as stratiform. Figure 2.5 shows how each step of the algorithm contributes to the convective pixels. For the cloud system shown in figure 2.5, the maximum number of convective pixels is identified by the BG criterion. Figure 2.6 shows an example of convective and stratiform areas identified by the algorithm.

2.5. Definition of storm

2-D projections of Z_e (e.g., Figures 2.3, 2.4 and 2.6) show that the high values of Z_e are confined to a few to several pockets within the areas identified as 'convective'. These pockets contain active convective clouds at that time instant. Dixon and Weiner (1993) defined a 'storm' as a set of connected pixels having Z_e above a prescribed threshold and the total volume of these pixels is at least 50 km^3. Dixon and Weiner (1993) took radar data collected near Denver and explored Z_e threshold values between 30 and 40 dBZ, and adopted 35 dBZ to identify storms. In a study of storms that formed in the Sidney area, Potts *et al.* (2000) used a 30 dBZ threshold and called them 30-dBZ storms. Johnson *et al.* (1997) used multiple reflectivity thresholds (WSR- 88D Build 9.0 storm algorithm known as SCIT algorithm) which in their opinion performed better than the single Z_e threshold of 30 dBZ followed in the WSR- 88D Build 7.0 storm algorithm. In this study, 30-dBZ storm (henceforth 'storm') is defined as a set of connected pixels in 3D space with a reflectivity threshold of 30 dBZ and the threshold criterion is satisfied in a volume of at least 50 km^3. Storm is extracted considering only those echoes which are identified as convective and using the TITAN (Thunderstorm Identification Tracking Analysis and Nowcasting - a set of applications developed at RAL, NCAR, Dixon and Wiener, 1993). The *TITAN-algorithm* is used to track

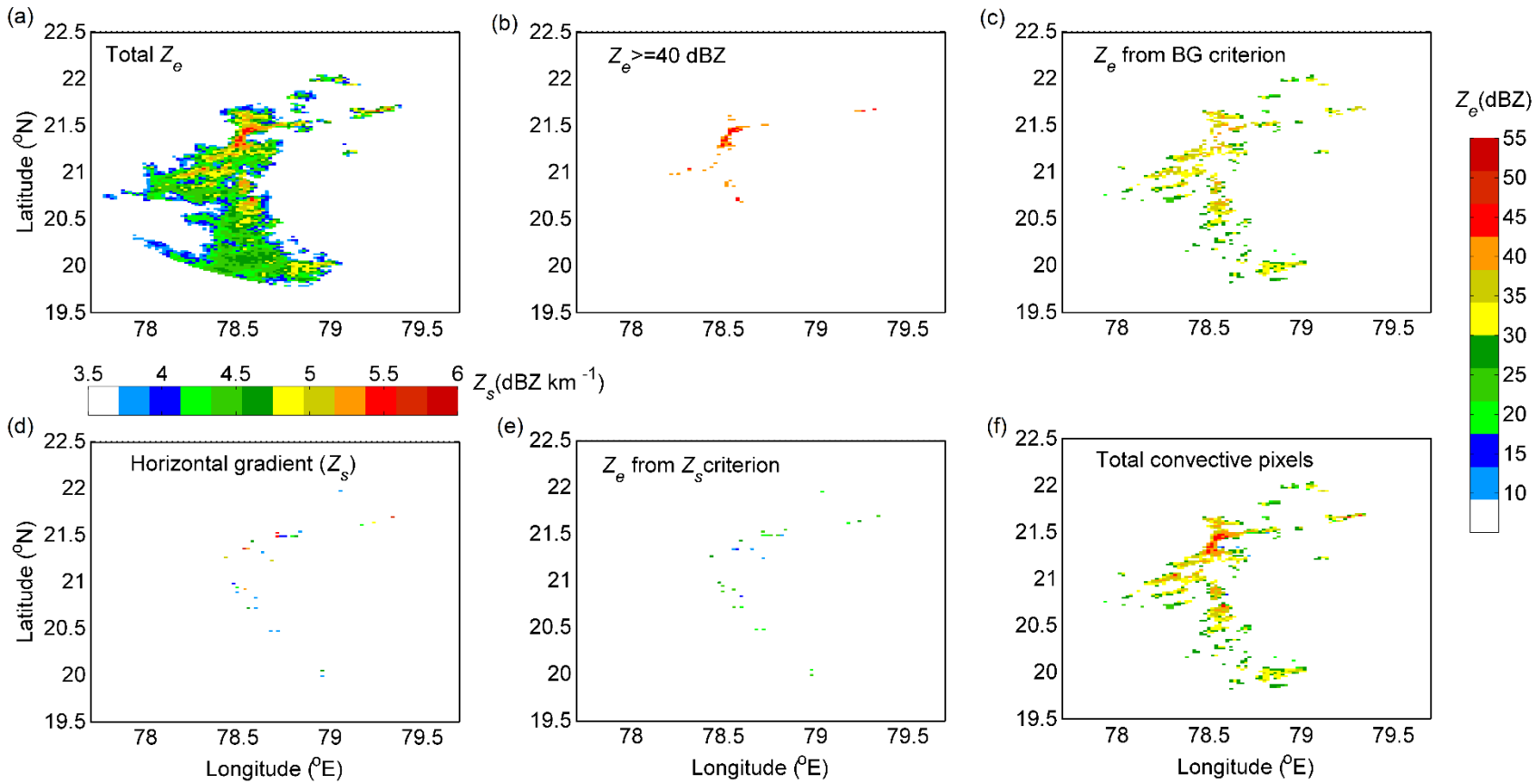

Figure 2.5. Illustration of the steps involved in the identification of convective pixels in MCS. The cloud system was observed over Nagpur at 1330 LST on 14 June 2013: (a) projection of maximum Z_e between 2 and 3 km (b) pixels having $Z_e \geq 40$ dBZ (convective). (c) convective pixels resulting from the BG criterion. (d) horizontal gradient in Z_e. (e) convective pixels resulting from the Z_s criterion and (f) total convective pixels.

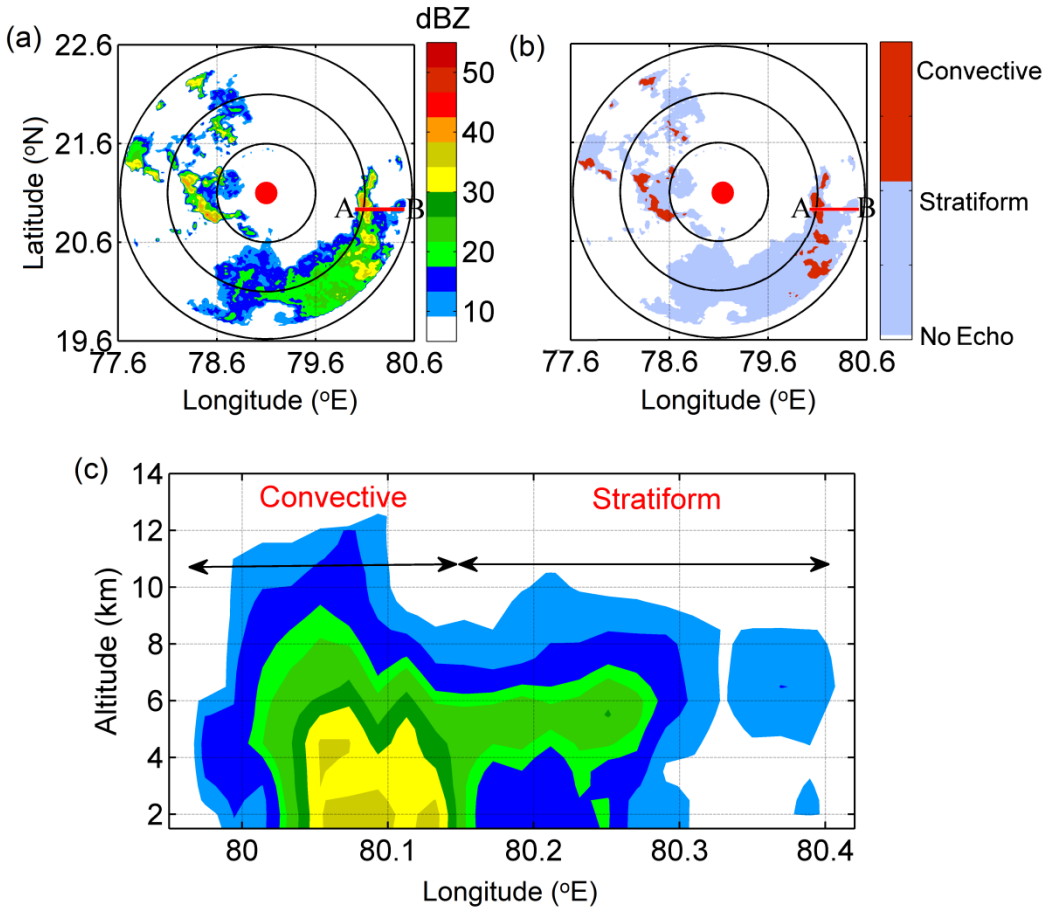

Figure 2.6. (a). Projection of the maximum Z_e between 2 and 3 km for an MCS observed at 2120 LST on 14 June, 2013 over Nagpur. (b) Convective and stratiform areas for the cloud system shown in (a). (c) Vertical cross section along the line AB in panel (b). In (a) and (b) filled red circle shows location of radar.

Table 2.4. Relationships used for estimating rain rate R (mm hr^{-1}).

No.	Relationship	Symbol	*a*	*b*
1.	Iguchi *et al.* 2000 $Z_h=aR^b$	R_{IG}	$^{\dagger}(148)_c,(276)_s$	$(1.55)_c,(1.49)_s$
2.	Hunter *et al.* 1996; $^{@}$MP 1948 $Z_h=aR^b$	R_{HMP}	$(300)_c$, $(200)_s$	$(1.4)_c$, $(1.6)_s$
3.	Bringi and Chandrasekhar 2001 $R(K_{dp})=a(K_{dp}/f^{*})^b$	R_{BC}	129	0.85
4.	Doviak and Zrnic 1993 $R(K_{dp})=a(K_{dp}{}^{\#}\lambda)^b$	R_{DZ}	5.1	0.86

$^{@}$ MP-Marshall and Palmer (1948); †foot suffixes *c* and *s* denote convective and stratiform precipitation; $^{*}f$ is radar frequency =5.62 GHz for the Delhi C-band radar; $^{\#}\lambda$ is radar beam wavelength= 5.33 μm

Table 2.5. Relationships used for estimating cloud liquid water content M (gm m^{-3}).

No.	Relationship	Symbol	c	d
1.	Greene and Clark 1972 $M(Z_h)=cZ_h^d$	M_{GC}	0.57	3.44×10^{-3}
2.	Bringi and Chandrasekhar 2001 $M(K_{dp})=c(K_{dp}/f^*)^d$	M_{BC}	3.565	0.77
3.	Doviak and Zrnic 1993 $M(K_{dp})=c(K_{dp}\lambda^\#)^d$	M_{DZ}	0.34	0.702

*f is radar frequency =5.62 GHz for the Delhi C-band radar; #λ is radar beam wavelength= 5.33 μm

the storms and a threshold of 30-dBZ is initially applied. It may so happen that this volume contains two or more closely spaced but distinct convective cells. A second threshold of 40 dBZ is applied to identify such cases to separate distinct storms and further extend outer boundary to 30 dBZ. All identified storms are tracked using *Tracks2Ascii* algorithm which provides instantaneous as well as aggregate characteristics (e.g., duration, area, volume, track etc.) of each storm. This data is used to understand the relationship between storm characteristics and MCS evolution.

2.6. Z-*R* and Z-*M* relations

Radar does not measure precipitation directly and empirical relations between instantaneous R and Z_e expressed in the form $Z_e = aR^b$ (e.g., Marshall and Palmer, 1948; Rosenfeld and Ulbrich, 2003) are inverted for estimating precipitation. Coefficients '*a*' and '*b*' are not unique and depend on DSD and drop fall velocities (Marshall and Palmer, 1948, Atlas *et al*., 1999). Table 2.4 lists some of the rain rate relationships employed for estimating *R* in this work. The present study uses the convective and stratiform rain relations $Z=148R^{1.55}$ and $Z=276R^{1.49}$, respectively (here Z is expressed in mm^6m^{-3} units), i.e., the same as that given by Iguchi *et al.* (2000) adopted in TRMM 2A25 rainfall version 5 dataset. These Z-*R* relations are further improved by Iguchi *et al*. (2009) which are adopted in 2A25 rainfall version 7 dataset but vast literature based on PR data used Z-*R* relations from Iguchi *et al*. (2000). Hence to assess the consistency of our results, the same Z-*R* relations are used for precipitation estimation comparison. Other Z-*R* relationships for convective and stratiform precipitation are adopted from Hunter *et al*. (1996) and Marshall and Palmer (1948), respectively. Using K_{dp},

the rainfall estimates are obtained from R-K_{dp} relations from Bringi and Chandrasekhar (2001) and Doviak and Zrnic (1993). Amount of condensed water in precipitation form is of great meteorological interest. From the data of ordinary radars, the so called Z-M relation (e.g., Greene and Clark 1972), where M is cloud liquid water content (units: g m^{-3}) is used to estimate M knowing Z. One major advantage of polarimetric radar is that its data products Z_{dr} and K_{dp} contain information about M and relations for M have been derived using these variables (e.g., Bringi and Chandrasekar, 2001, Ch. 8). Here M is estimated using three different relations which are listed in Table 2.5.

2.7. Contoured frequency by altitude diagram, area time integral, radar estimated rain volume, precipitation amount

The contoured frequency by altitude diagram (CFAD) was first introduced by Yuter and Houze (1995) for studying the average characteristics of several convective clouds measured by radar. At each height, frequency of occurrence of reflectivity is generated in different bins considering all Z_e profiles for each cloud, and then a 2D map created combining data at different levels. In the present study, the reflectivity bin size is kept at 5 dBZ. The height intervals for CPR and PR are kept fixed 0.24 and 0.25 km, respectively while for DWRs data, the height interval is kept at 0.5 km. Further, the number of cases in a reflectivity bin at each level k is normalized by the total number of cases (N_k) at that level. Normalized individual histograms are combined and contours of frequency of occurrence are plotted with reflectivity along x-axis and height as ordinate. CFAD provides a method of pictorially representing the vertical variations in cloud systems. This is alright as long as values of N_k at different levels are comparable. However, when the sample number becomes small, the statistics obtained is not representative or robust. In order to avoid the inclusion of cases with small N_k, Yuter and Houze (1995) imposed the condition that number N_k should not be less than 10–20% of N_m, where N_m is the maximum value among all N_ks. In this work, if N_k is less than 10% of N_m (i.e., $N_k/N_m \geq 0.1$) then that level data is excluded from CFAD structure.

Convective area fraction (CAF, i.e., fraction of the total echo area within MCS occupied by convective echoes) is calculated taking the 2D map constructed for identifying the convective pixels within an MCS. R is computed taking CAPPI (constant altitude plan position

indicator) at 1.5 km height. For each volume scan, precipitation rates for convective and stratiform echoes are estimated separately by applying respective Z-R relations and precipitation volume rate (*PVR*) is obtained. The ratio of convective to total PVR gives CPF. Area time integral (ATI) combines spatial extent and life span of a precipitation event (Doneaud *et al.* 1981) and is defined by the sum

$$ATI = \sum_i A_i \Delta t_i \tag{2.6}$$

where A_i is the area over which rain is detected at i^{th} time instant and Δt_i is the time interval between two consecutive observations.

The radar estimated rain volume (RERV) is the rain rate integrated over an area A during time T. The expression for *RERV* (Doneaud *et al.* 1984) is given by

$$RERV = \int_T \int_A R \, dA \, dt, \tag{2.7}$$

where *R* is the instantaneous rain rate (in mm hr^{-1}), dA and dt are the infinitesimal area and time increments and the double integrals are taken over entire area '*A*' (in km^2) covered by radar beam during time span of *T* (in hour) (Atlas *et al.* 1990). Using mean value theorem, the expression for *RERV* can be re-written as

$$RERV = R_c \int_T \int_A dA \, dt \approx R_c \sum_i A_i \Delta t_i, \tag{2.8}$$

where integral over area and time is defined by $\sum_i A_i \Delta t_i$, known as ATI. R_c is the average rain rate in the space time volume which is obtained only in the precipitation area '*A*' which is enclosed by a threshold value of Z_e. Here, *ATI* is approximated by finite summation (Atlas *et al.* 1990).

ATI and *RERV* are related in the form of power law relation, i.e.,

$$RERV = K(ATI)^b \tag{2.9}$$

where K and b are the coefficient and exponent which are unique for data of peculiar ATI and RERV values. From expressions (2.6), (2.8) and (2.9),

$$R_c = RERV/ATI = K(\mathrm{ATI})^{b-1} \tag{2.10}$$

Hence from above relation, the average rainfall rate using *K* and *b* is estimated. if b<1, then larger storms with longer durations will give lower average rainfall rates (See Doneaud *et al.* 1984 for more details).

Precipitation amount '*P*' is expressed as mass of rain water accumulated during storm lifetime and is calculated from

$$P = \rho_w \int_T \int_A R\,dA\,dt \tag{2.11}$$

where ρ_w is the density of water (~1000 kg m^{-3}) and R is rain rate. The double integration is performed over storm area '*A*' and over storm duration '*T*'.

2.8. Vertical profile of radar reflectivity

Tall Cb clouds connect the boundary layer to the upper troposphere and play a major role in the vertical transport of energy in the atmosphere. Hence knowing the vertical structure of Cb clouds becomes important. Vertical profile of radar reflectivity (VPRR) is a method proposed by Zipser and Lutz (1994) to extract vertical profiles from a radar volume scan. Maximum Z_e is searched among the pixels identified as convective in the 2D map (Figure 2.5). Keeping the column containing this pixel at the centre, maximum Z_e is searched in a box of 6 km×6 km at different levels, and the cloud cell is assigned this value at respective heights. A cloud cell so obtained is called a VPRR. The rationale behind searching neighboring columns is that Cb clouds are often not perfectly vertical owing to wind shear and a Cb cloud might have been captured in neighboring columns in a radar volume scan. The Z_e values in all the nine columns associated with the cloud cell already constructed are set to zero, and the procedure repeated till no more convective pixels remain.

3

Properties of clouds over the Tibetan Plateau and comparison of CPR and PR reflectivities

3.1. Motivation

Tibetan Plateau works as elevated land heat source and associated upper air circulation influences the Indian monsoon (Rao, 1976; Boos and Kuang, 2010; Chen *et al.* 2014, etc.). Not much information was available in the literature on the cloud systems over this region including how clouds over the Tibetan Plateau evolve with season. This thesis work started with analysing cloud systems over the Tibetan Plateau by examining their horizontal and vertical organisation using the CPR data. First let us look at the seasonal evolution of moist static energy (MSE) over the Tibetan Plateau region. If moist air from near the surface rises and forms a cloud conserving its MSE, then the height to which its cloud top reaches is approximately the level at which MSE of cloud air equals that of the environment. Figure 3.1 shows the vertical profiles of MSE from May to September. Lhasa is at an elevation of about 3.6 km above sea level. Here depending on the month, MSE decreases with height in the lowest 3 to 4 km layer of the atmosphere. July and August months have the highest MSE at the surface and in the lower troposphere. At Nagquo, if the lowest (i.e., surface) level is not considered, MSE increases with height in May, and thus not favorable for convection. June and September months have well mixed MSE structure in the lowest 2 km layer of the atmosphere. It is seen from Figure 3.1 that in all these months, top most height of clouds is about 10 km or less. Next let us see next what CPR data shows.

Figure 3.2 shows Kalpana-1 IR brightness temperature on 25 May, 2009. The large scale clouds over the region were associated with the tropical cyclone Aila. The thick line shows the path of descending overpass of CPR on the same day, and the corresponding

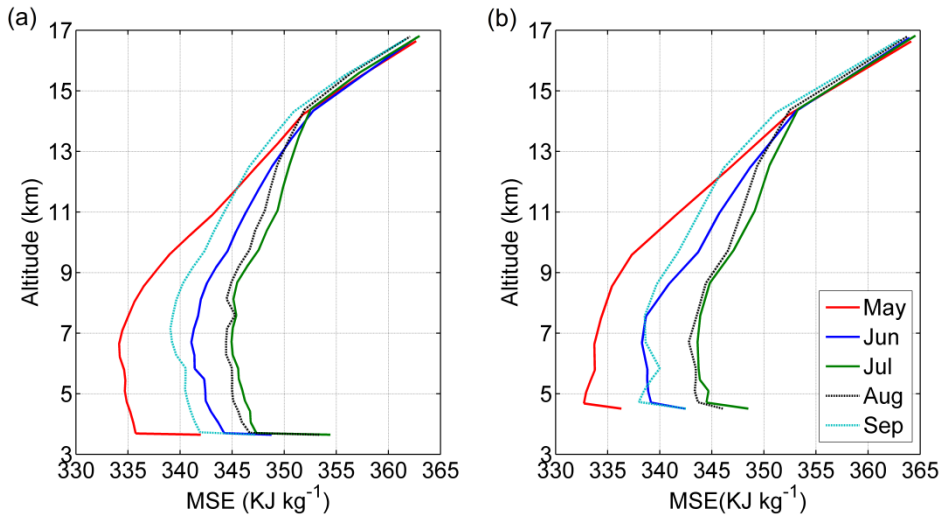

Figure 3.1. Average vertical profiles of moist static energy measured at upper air stations in the Tibetan Plateau region during May to September months in the year 2008. Left: Lhasa (29.6°N, 91.1°E) and, right: Nagquo (31.4°N, 92°E). The radiosonde data is obtained from the University of Wyoming for both the locations.

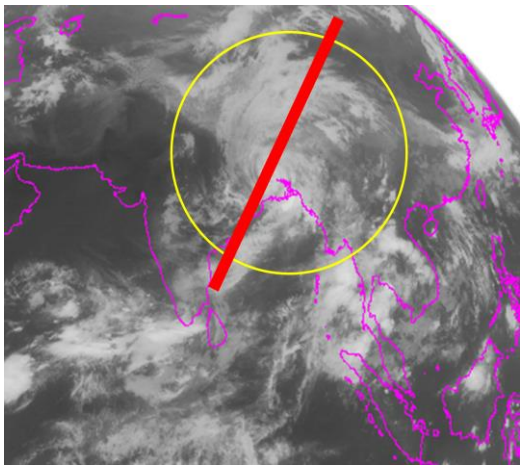

Figure 3.2. Brightness temperature measured by Kalpana-1 satellite over Indian region. The red line shows the descending overpass of CPR through the cyclone AILA observed at 18:30 LST on 25 May, 2009.

vertical distribution of Z_e is shown in Figure 3.3. The cloud band is more than 1000 km in the horizontal, and vertical extent is more than 10 km but less than 15 km. Some vertically inclined individual convective cells can be identified in the section in the southern sector and extensive stratus clouds in the northern sector. Data below the plateau surface is noise. The maximum Z_e within deep convective clouds is less than 25 dBZ. As the season progresses, vertical extent of convective clouds become deeper and echo top heights exceeding 17 km are observed (Figure 3.4). Vertical profiles of monthly mean of maximum

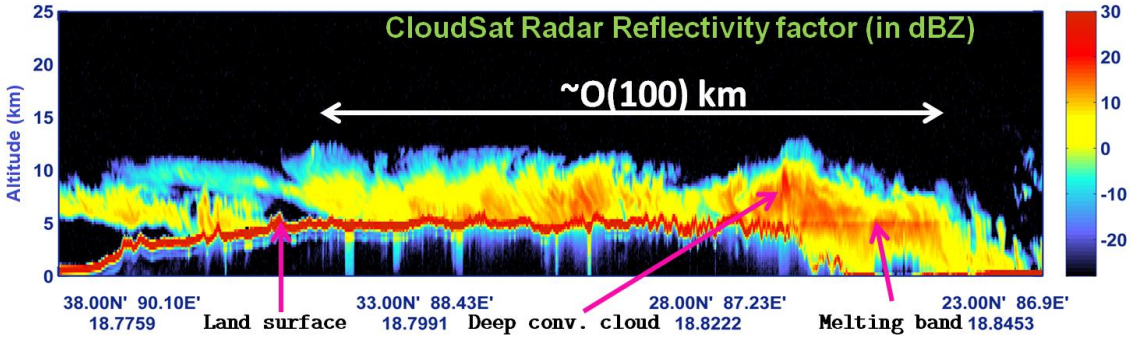

Figure 3.3. Vertical section through a cloud system over the Tibetan Plateau captured with the CPR. The colorbar coded here is CPR radar reflectivity in dBZ units. The signatures of deep convective cloud and melting band (around 5 km altitude) are captured. Thick red line shows the land surface elevation of Tibetan Plateau along the section.

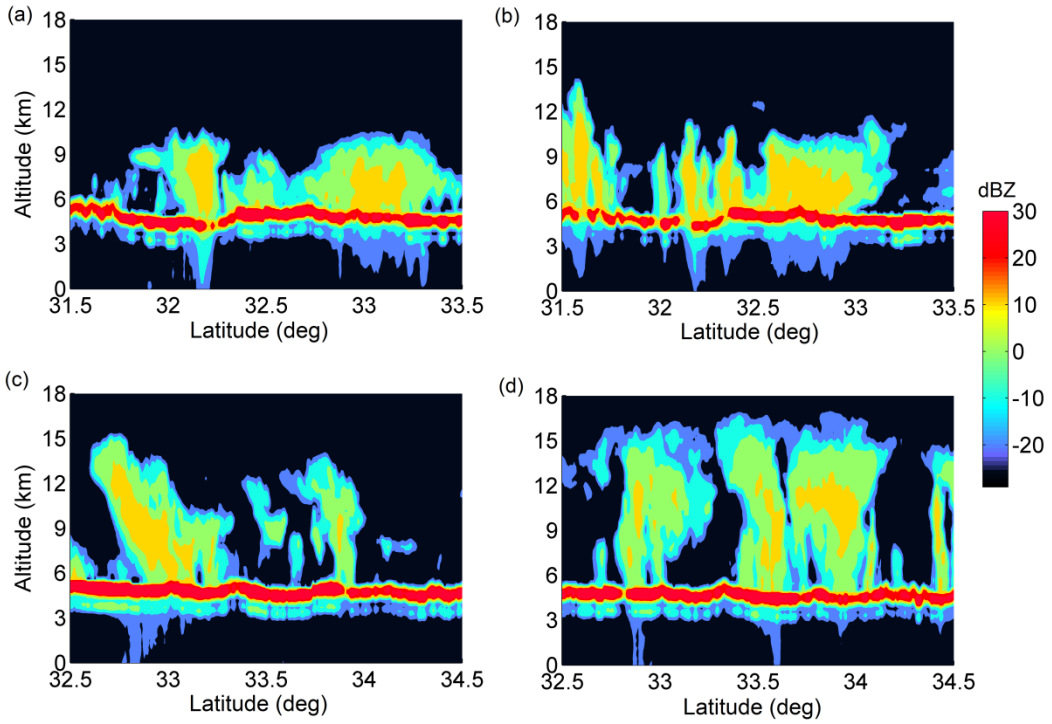

Figure 3.4. Cloud systems over Tibetan Plateau observed by CloudSat on (a) 7 August, 2007, (b) 13 July, 2008, (c) 19 July, 2008 and (d) 10 August, 2010. The colorbar coded here is radar reflectivity in dBZ.

Z_e at different levels are also prepared and shown in Figure 3.5. The Z_e values reach maximum in the peak monsoon month of July and August and decrease prior and after these months. Average maximum echo top heights are as high as 15 km in July and August which correspond to very deep clouds, and such deep echo top height is much higher than that based on the MSE profile analysis. There could be three reasons for this. There is variation

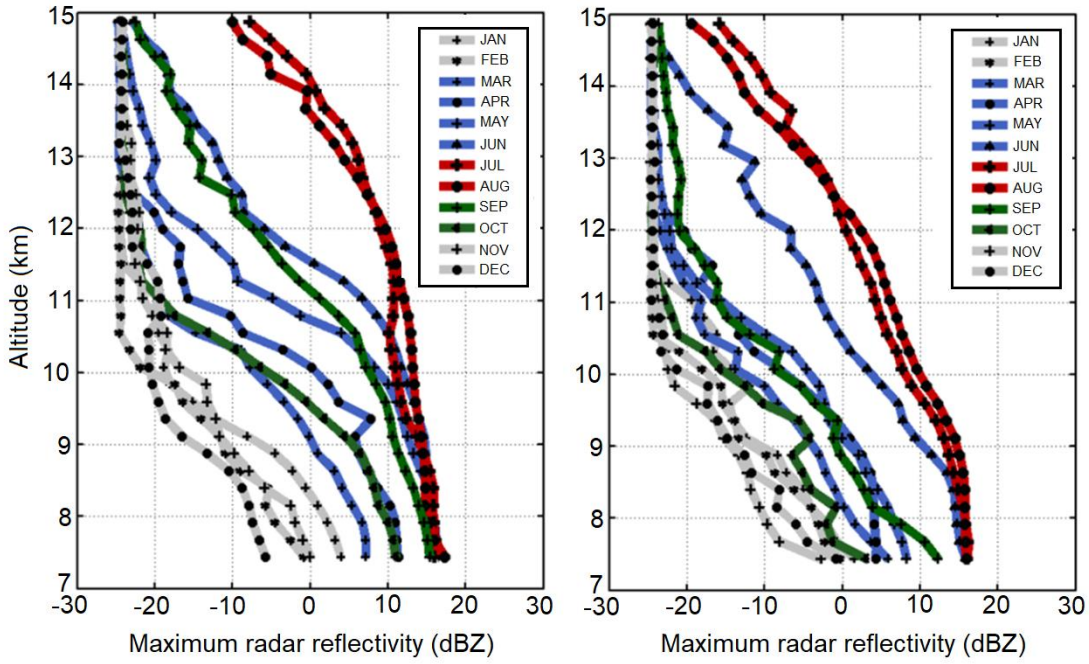

Figure 3.5. Vertical profiles of monthly mean of maximum Z_e over Tibetan Plateau during for the year 2008. Each profile corresponding to each month is mean of all vertical profiles of the maximum Z_e during that month. Panels (a) and (b) are corresponding to CPR ascending and descending overpasses over Tibetan Plateau.

in the vertical profile of MSE on synoptic time scales. The soundings shown in Figure 3.1 correspond to that taken at 00 UTC, which is early morning (near sunrise) over the Tibetan Plateau area. Diurnal variation is large over the land surface and that could make the surface MSE much more unstable in the afternoon hours. Lastly, MSE is calculated using phase change of water from vapor to liquid. Glaciation at sub-freezing temperatures adds additional heating to the air parcel and can also enhance the cloud parcel buoyancy.

Thus deep convective (Cb) clouds are present over the Tibetan Plateau during July-August months. One point of concern is that the maximum Z_e never exceed 25 dBZ. Previous studies (Steiner *et al*. 1995, Houze 2004 etc.) suggest that convective echoes have Z_e more than above 35 dBZ. Values of maximum Z_e in Figure 3.5 are well below this and two questions, namely: a) do deep convective clouds over the Tibetan Plateau really have low Z_e and hence hydrometeor concentration?, or b) low value of maximum Z_e an artifact of high attenuation of the CPR beam in convective clouds?

To address these questions, I compared vertical profiles of Z_e obtained from the CPR and the PR. To my knowledge a study that compares PR and CPR reflectivities was not available in

the public domain and this study is aimed at filling the gap by using coincident (collocated and near simultaneous) data from both satellites.

3.2. Coincident CPR and PR measurements

For a fair comparison, it is important that both satellites measure a given sampling volume near simultaneously. PR and CPR have different swath widths, footprint sizes and orbital trajectories. Because the satellite carrying the former is non-Sun-synchronous and that carrying the latter is Sun-synchronous, their orbits do intersect approximately 30 times per day. As part of CloudSat project, 2D-CloudSat-TRMM Product is made available at www.cloudsat.cira.colostate.edu (a note prepared by Carty and Kuo in 2008 and available at the website gives product details). In this product, intersect is defined as both TRMM and CloudSat observing the same geographic location on the surface of the Earth with time difference of 50 minutes or less. The intersection of CloudSat path with the midpoint of PR swath is taken as the point of intersection. The present work uses the CPR reflectivity product 2B-GEOPROF and PR attenuation corrected reflectivity product TRMM 2A25, both archived under 2D-CloudSat-TRMM dataset. Two data subsets are prepared around the point of intersection. For the PR data, PR blocks data that includes the entire PR swath from 10 scans before and 10 scans beyond the region of intersection. The PR curtain data, a subset of PR block data containing interpolated PR data along the CloudSat track using a simple nearest neighbour approach to match the CPR horizontal resolution, but no vertical resolution matching is performed. CPR curtain data includes the CPR track data 50 scans before the point of intersection to 50 scans beyond the point of intersection. These are called coincident overpasses. 2D-CloudSat-TRMM dataset spans July 2006 to December 2010, i.e., approximately 4 years and 6 months, providing ~29,000 coincident overpasses. Figure 3.6 shows a few examples of PR and CPR coincident overpasses. Because of the difference in their pixel sizes, sampling volumes do not completely overlap. Basically CPR slices through clouds and provides a vertical section along its track, whereas PR captures the 3D structure ~250 km across. Figure 3.7 is a pictorial representation of intersection points of CRP and PR coincident overpasses. It is seen that the entire latitudinal belt of 38°N-38°S is covered more or less uniformly with coincident overpasses.

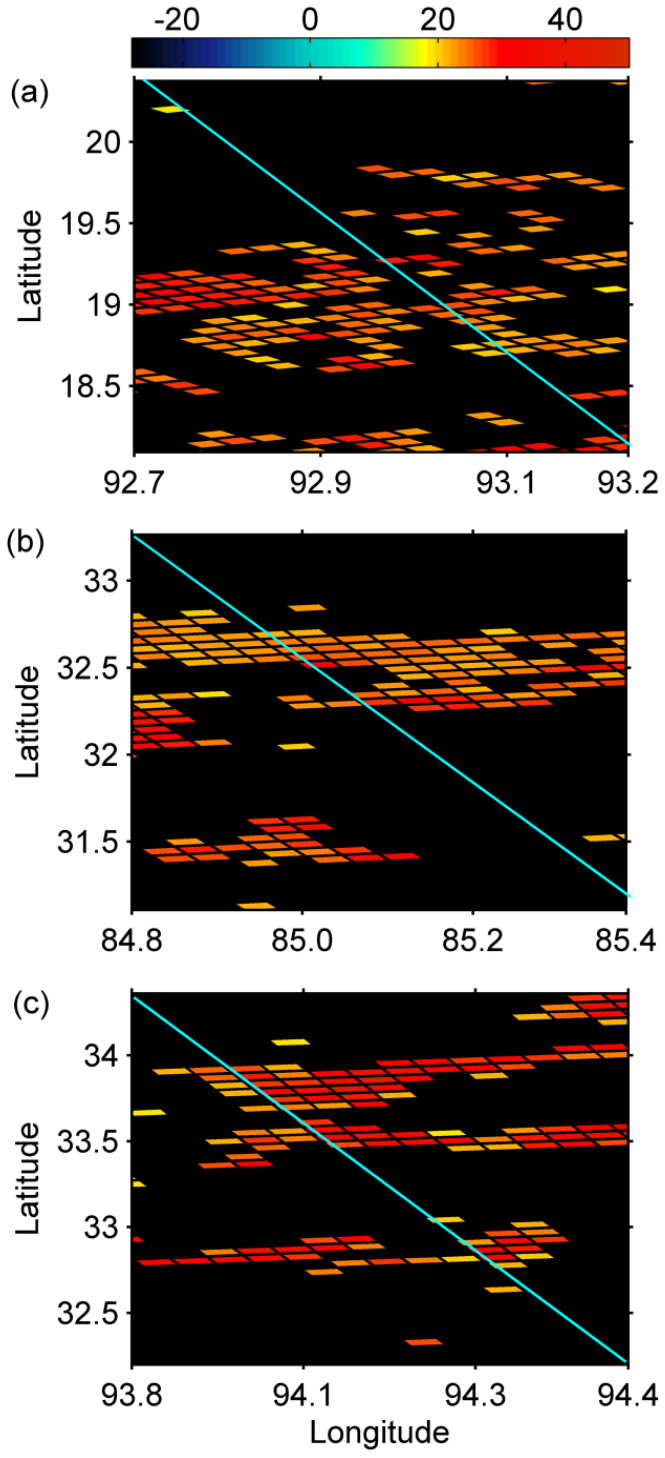

Figure 3.6. Example of TRMM PR and CloudSat CPR coincident overpasses observed on 8 July 2008 over Bay of Bengal (top); 13 July 2008 over Tibetan Plateau (middle), and 10 August 2010 over Tibetan Plateau (bottom). Continuous lines show the path of CloudSat and parallelograms PR footprints. For PR, the maximum reflectivity in each vertical column of the grid is projected onto the plane. Color bar on the top refers to PR Z_e in dBZ units.

3.3. Methodology

PR and CPR sampling volumes (footprint sizes in particular) are different and there could be a time delay of up to 50 minutes, thus making one-to-one comparison of instantaneous Z_e profiles from these two radars not very meaningful. However, the statistics of their Z_e values can be compared for the coincident overpasses for the following reasons. In most of the results presented here, cases are included where clouds were precipitating by requiring that PR $Z_e \geq 25$ dBZ at least at one vertical level (moderate rain and heavy snow expected e.g., Houze 1993). As seen from Figure 3.7, oceans dominate the study area where

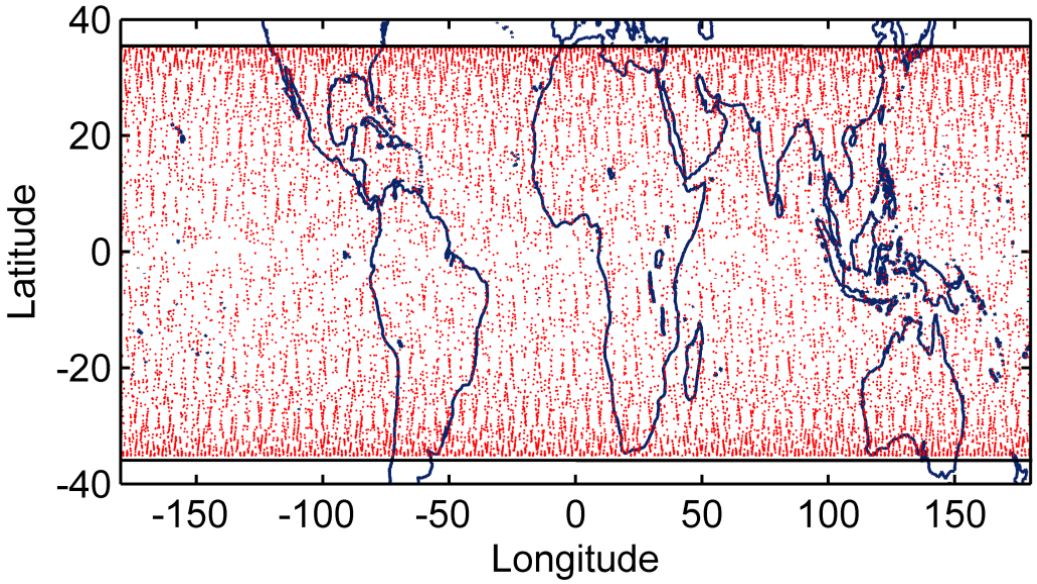

Figure 3.7. Intersection points of coincident CPR and PR overpasses for the period July 2006 to December 2010.

precipitating clouds are normally found in the presence of large scale low level convergence (e.g., Cotton and Anthes 1989) which tends to be a synoptic scale feature. Then major changes in the properties of cloud population within an hour are not expected. Since PR is not Sun-synchronous, there is equal probability of PR sampling before and after a CPR pass. Thus, there is no bias in the sampling time difference between PR and CPR coincident passes. Present study uses a large number of coincident overpasses spanning four and half years. Therefore the statistics so obtained is expected to represent average properties of precipitating cloud population in the study region. In the following, analysis is performed considering two cases:

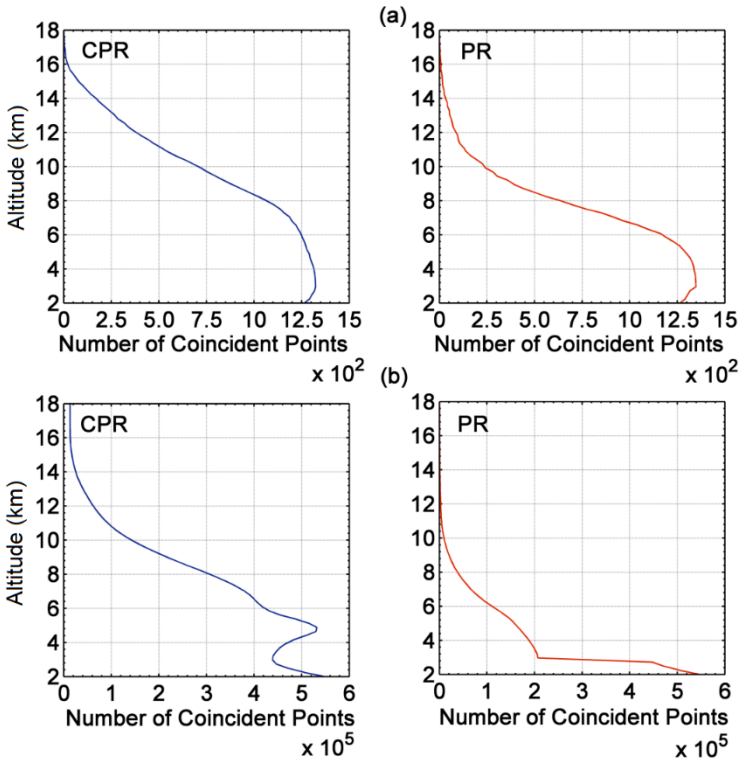

Figure 3.8. Number of coincident points at different vertical levels for case 1 and case 2. For case 1, both CPR and PR show similar trend but not exactly identical owing to the difference in their footprint sizes. Numbers of coincident points are very few above 15 km. For case 2, CPR shows a peak around the freezing level and at 2 km height, whereas PR has peak at 2 km and numbers drop drastically above 10 km.

Case 1: Includes data from coincident passes where both PR and CPR share common sampling volume, i.e., collocated. Further, the PR volume contains $Z_e \geq 25$ dBZ at least at one vertical level.

Case 2: Includes data from grids surrounding the collocated point as well. Thus majority of the volumes are not collocated but both radars sampled the same area near simultaneously. No condition is imposed on magnitude of Z_e. Layer of the atmosphere between 2 and 18 km altitude range is considered with the lower limit imposed to avoid possible ground contamination, and the upper limit to save computational time since probability of getting valid Z_e is very small above this height (Figure 3.8).

3.4 Results and discussion

Figure 3.9 shows the CFADs of CPR and PR reflectivities. Horizontal extent at any given height gives the observed range of Z_e and maximum indicates the most frequently

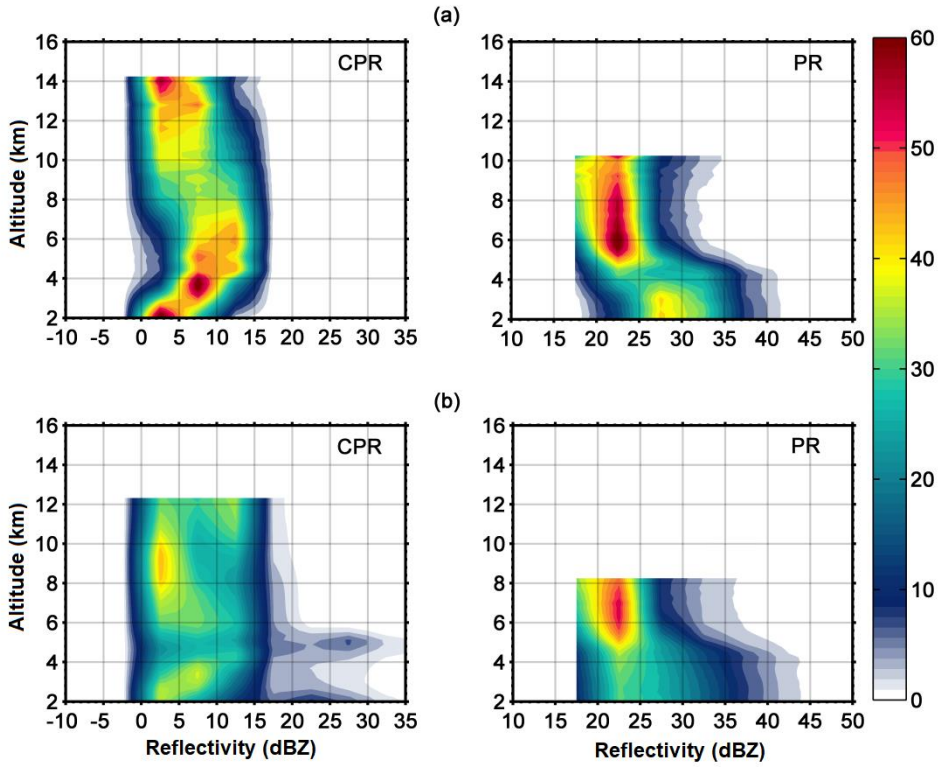

Figure 3.9. Contoured frequency by altitude diagrams (CFADs) of reflectivities for case 1 (top) and case 2 (bottom). The bin size for Z_e is 5 dBZ and height intervals are 0.24 km and 0.25 km for CPR and PR respectively. The color bar shows the frequency (in %) of reflectivity occurrence. Differences in the maximum heights of the contours and abrupt ending are due to the number of points falling below the 10% criterion used in CFADs (see text for details). The contours' values lower than the minimum detectable limit of 17 dBZ has been discarded in PR CFAD.

measured value (related to the cloud type) at that height. The most striking feature observed in Figure 3.9 (a) is that the peaks in CFADs are distinctly different for CPR and PR so much so that it seems that these two radars are sampling different class or populations of clouds. The differences in the horizontal range are far outside the claimed accuracies of ~ 1-2 dBZ of CPR and PR and their modes are separated by more than 10 dBZ below 10 km height. CPR mode bends towards lower values of Z_e below 4 km height whereas PR shows the opposite (Figure 3.10 a). Nature of the vertical variation of maximum frequency of occurrence of CPR and PR reflectivities are also different (Figure 3.10). CPR has two maxima, one at lower (~2 km) and another at higher (~14 km) altitudes. The maximum frequency at the higher altitude indicates that CPR captures the anvil clouds associated with MCSs, and the other peak is likely to correspond to low level convective clouds (perhaps precipitating

cumulus congestus and low level stratus). PR Z_e shows a peak frequency of occurrence between 6 and 7 km height centered on Z_e = 22.5 dBZ while there is no peak in CPR CFAD in this height range. CFADs of CPR and PR reflectivities for case 2 look different but the main observation made earlier, namely the two radars appear to sample different cloud populations holds good here too (Figure 3.10 b). The total area considered in the analysis included tropics and mid-latitudes, and cloud systems may exhibit different vertical variations in cloud hydrometeor properties in these two regions. To explore if the agreement is better in the tropics, analysis was repeated considering the tropics only (i.e., 30˚S-30˚N). Results more or less reproduced the features observed above and thus the conclusions remain the same for the tropics as well. Figure 3.10 (c) shows the frequency distributions of CPR and PR reflectivities for case 1 considering all levels between 2 and 18 km. CPR Z_e is slightly negatively skewed whereas PR Z_e is positively skewed. The maxima in the reflectivity distributions of CPR and PR are approximately at 9 and 22.5 dBZ, respectively. Number of occurrences of Z_e values above 20 dBZ is negligible in CPR measurements. As per the technical specifications (Table 2.1) measurement range of CPR is -30 dBZ to +40 dBZ , while the PR Z_e values start at ∼17 dBZ. Therefore some overlap of CPR and PR distributions is expected but not observed in Figure 3.10 (c). This suggests that the W-band radar signal gets strongly attenuated in precipitating clouds, especially below 6 km height where PR Z_e shows higher values. Figure 3.10 (c) reveals that CPR range ends where PR begins, i.e., PR and CPR cover two ends of precipitating clouds, namely PR measurement capability limited to active precipitating clouds, and CPR more reliable in measuring the spatial extent of cloud systems but not their hydrometeor concentrations (e.g., anvil clouds away from convective core). Matrosov (2014) examined a precipitating event using near-coincident data from CPR and KGWX WSR-88D radars and found that both CPR and WSR-88D radars are able to capture the high cloud tops due to their higher sensitivities (lower detectable Z_e<-28 dBZ) however CPR misses the severe precipitation features at lower altitude levels (<4 km). Another study by Matrosov (2015) compared CPR profile with KSHV WSR-88D radar and revealed that CPR is able to capture the bright band level but it is missed by WSR-88D radar. They also found that both radars are able to sense the anvil portion of the clouds due to their higher sensitivity limits. Vertical extent of the clouds captured by CPR is higher than PR as reported previously (Li and Schumacher 2011).

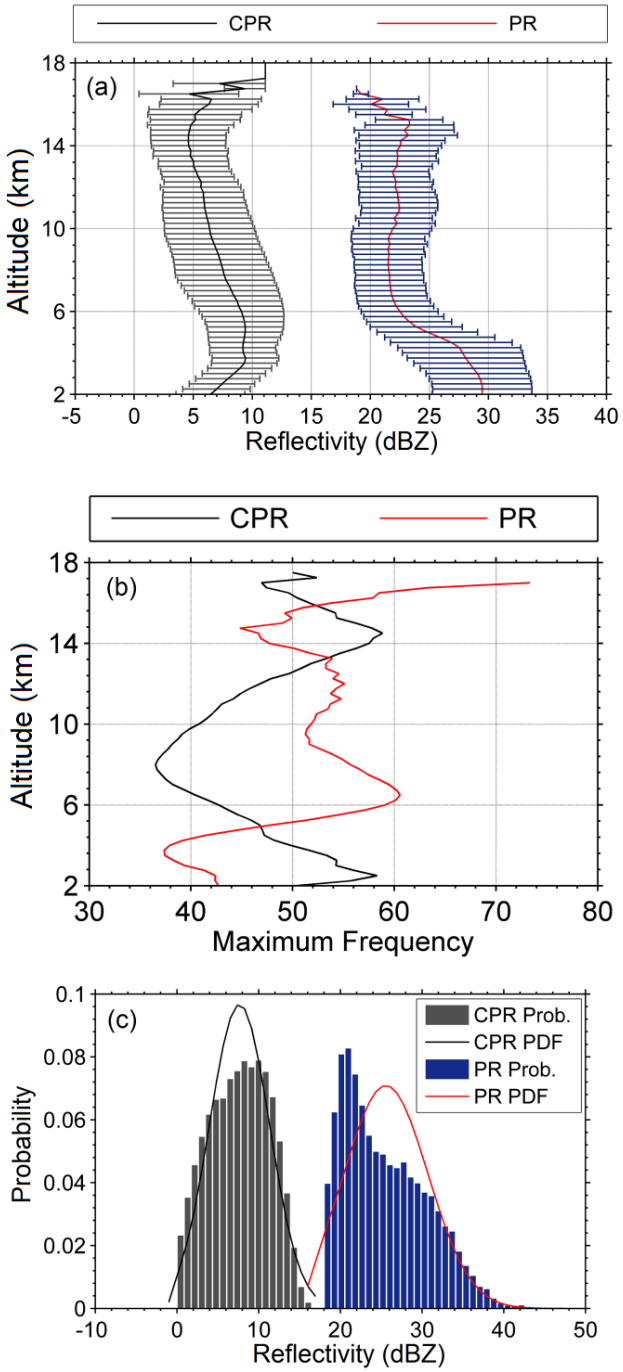

Figure 3.10. (a) Vertical variation of the mean reflectivity for CPR and PR for case 1. The error bars correspond to one standard deviation about the mean. At no height, two measurements come close to each other, and mean trends are in opposite directions below 6 km level. (b) Vertical variation in the maximum frequency of occurrence of CPR and PR reflectivities for case 1 indicating the preference for a certain Z_e to occur more frequently at that height, and the mode itself a function of height as shown in Figure 3.9. (c) Histograms of the reflectivities for CPR and PR for case 1. Reflectivity values at all heights are taken into consideration while constructing these histograms. Curves (in red and black colors) are the probability density functions obtained by fitting normal distribution function.

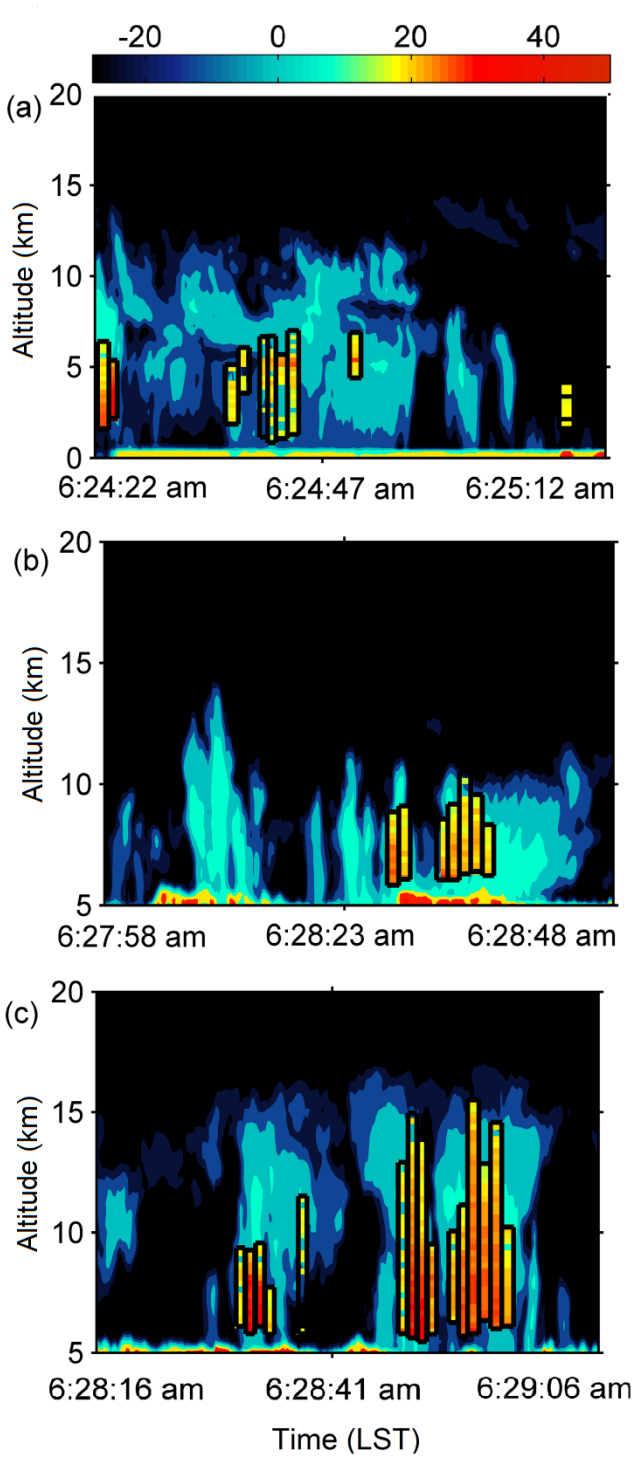

Figure 3.11. Vertical cross sections of PR Z_e superimposed on that of CPR along the CloudSat path for the cases shown in Figure 3.6 in the same order. Discrete vertical bars and blue color correspond to PR and CPR reflectivities, respectively. High values at the bottom may be due to surface reflectance (especially over the Tibetan Plateau). The color bar shows the radar reflectivity values in dBZ.

Hence combining data from these two radars may lead to more realistic picture of the spatial structure of convective cloud systems. For example, PR curtain reflectivity is superimposed over the CPR curtain reflectivity in Figure 3.11. In this case, PR data reveals convective towers while the CPR a much extended region of cloudiness.

3.5. Summary

Very deep convective cloud systems form over the Tibetan Plateau during July-August months. This understanding was made possible by data of spaceborne radars, namely the CPR and the PR that provided vertical profiles of clouds globally. However, both CPR and PR have measurement limitations. Here the coincident 2D-CloudSat-TRMM product for comparing the radar reflectivities of CloudSat CPR and TRMM PR radars is used. The PR, essentially meant to measure characteristics of precipitating clouds, misses the anvil part of mesoscale convective systems, and the full spatial extent of MCSs is not covered. The CPR captures the cloud spatial coverage better. However, CPR reflectivity values are much lower due to the strong attenuation suffered by the radar beam operating in W-band specifically below the melting layer (~4 to 5 km above ground level). CPR signal gets attenuated severely in precipitating clouds, more so below 6 km height. Stephens (1994) attributed this attenuation to 'non-Rayleigh scattering regime' mainly caused by scattering of radar wave by large hydrometeors when their sizes become comparable to or greater than the radar wavelength. Kollias *et al.* (2007) have reported that the radar signal attenuation is more prominent as radar wave frequency increases.

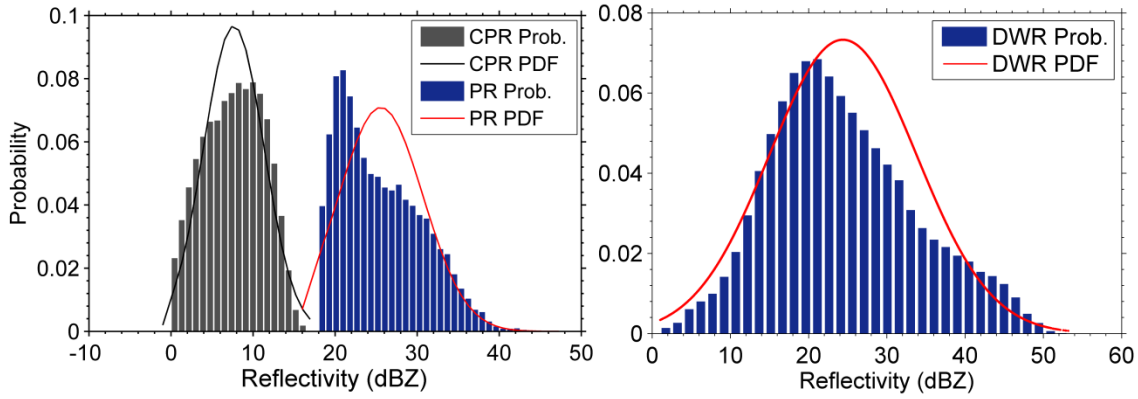

Figure 3.12. Intercomparison of probability distributions of radar reflectivity obtained from CloudSat CPR, TRMM PR and DWR.

Therefore, although the technical specifications of the two radars indicate that their measurements have common overlap region in 17 to 40 dBZ range, the actual data show very little overlap in their measured Z_e values. These limitations are to be considered while deriving conclusions on cloud properties from PR and CPR data. Having realised the limitations of the CPR, especially below 8 km altitude, I decided not to interpret the cloud microphysical processes responsible for producing the average CPR profiles observed, say in Figure 3.5. It is felt that ground radar may provide more correct information on the vertical structure of monsoonal clouds. Figure 3.12 shows the probability distribution of CPR and PR Z_e values. It is observed that the probability distributions of CPR and PR reflectivities have very little overlap. A significant portion of reflectivity values are missing between these two. The ground weather radar reflectivity distribution covers the gap area between the distributions from CPR and PR. Thus ground radars provide more accurate information on the true nature of clouds. DWRs have very high sampling frequency (1 volume scan/10 minute) but have a limited spatial coverage (useful data limited to typically 150 km radius around the DWR location). Hence the PR and ground radars complement each other.

4

Characteristics of mesoscale convective systems

4.1. Preface

Seasonal (June to September) monsoon rainfall over India was 106% of its long period average in the year 2013, and eighteen monsoon synoptic systems formed during the season (Pai and Bhan 2013). Many cloud systems formed around the five DWRs considered in this study, however, majority of them formed elsewhere, came within DWR range for some time and then moved out. The key objectives of this work are to understand the temporal evolution of MCSs and their interconnections with storms. For this purpose, a case of MCS is studied if MCS either evolved and dissipated within the radar range or spent at least major fraction of its life within this area.

The typical 2D and 3D structure of MCS is shown in Figure 4.1 and 4.2. The data is for MCS observed over Patna on 14 August in the year 2012 at 8:42 UTC. The color in 2D structure is the maximum radar reflectivity factor at all vertical levels and the ellipses are the areal coverage of the storms. Here storms are identified using single threshold identifications using T_z=30 dBZ. It shows the merging of two storms that formed at nearby locations. After a period of 40 minutes (4 consecutive radar scans), these two storms merge together and become one big storm which has large areal coverage as well as high vertical extent (>14.5 km) compare two the earlier existed storms (~12.5 km). After merging of these two storms, the bigger storm moves in the direction of the movement of MCS. It is a classic example of how two storms merge together within MCS. The vertical structures of MCS across the storm track at different time instants are shown in Figure 4.2. Each panel is distant at the interval of 10 minutes. It can be seen how the storms within the MCS form, evolve and decay with time. One storm forms and merges with the other and become bigger one. As time progresses further, the bigger storm decays and formation of another storm takes places. This process of formation and decay and merging and splitting of storms happens

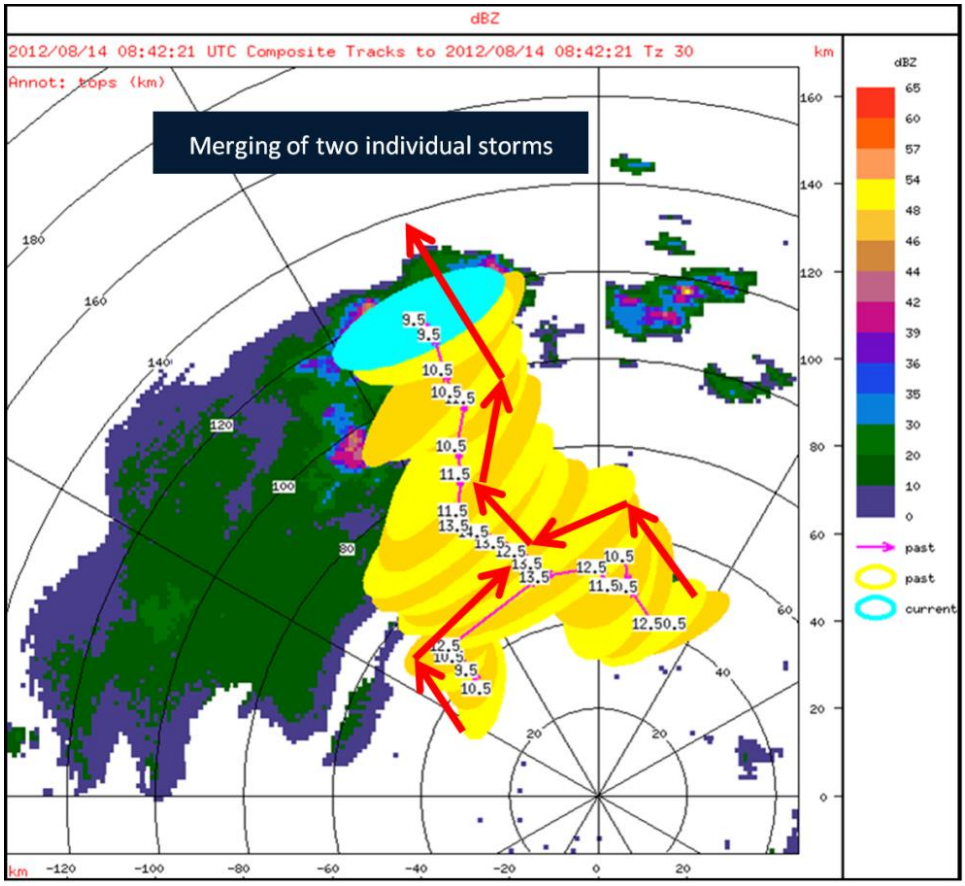

Figure 4.1. Merging of two storms within the MCS observed over Patna on 14 August in the year 2012 at 8:42 UTC.

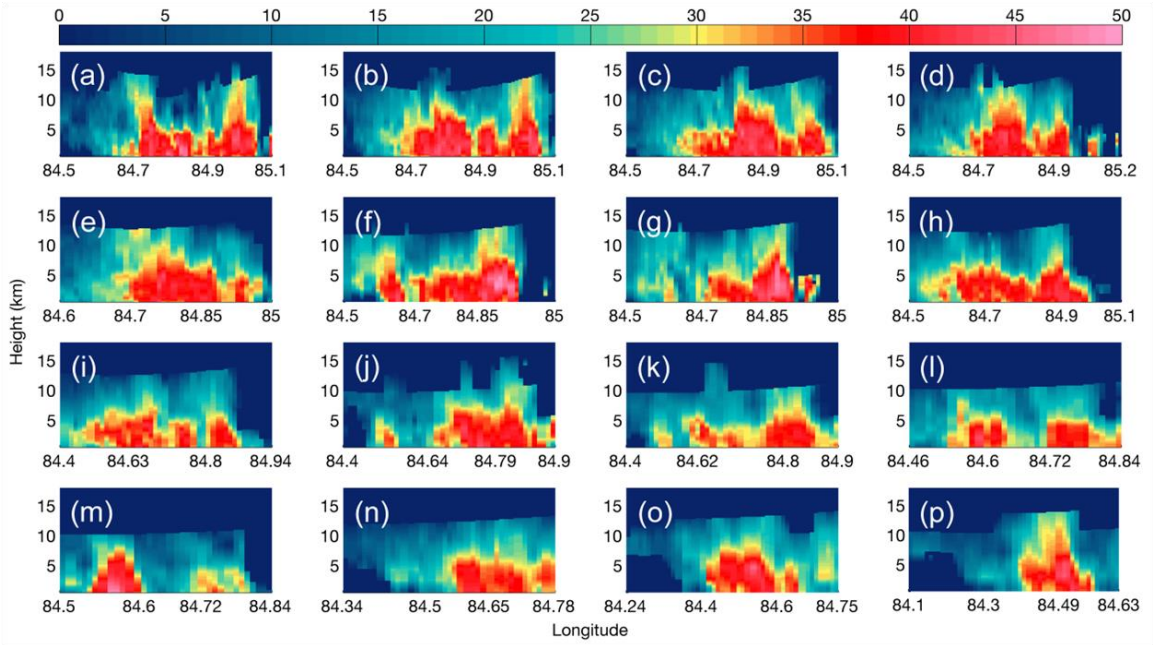

Figure 4.2. Vertical structures of storms within MCS. Each panel is obtained at the interval of 10 minutes.

within the lifetime of MCS. How the number of storms within the MCS varies and how they behave within the lifetime of MCS? How much these storms contribute in total convective area? How much the convective echoes contribute in total area and precipitation within MCS lifetime? Are these MCS formed over different DWR locations show spatial differences? How much they differ in vertical dimension? All these issues are looked in detail in this chapter.

The total 13 MCSs (2 each at Delhi and Hyderabad, and 3 each at Kolkata, Nagpur and Patiala) are selected (see section 2.3 for details). I start with presenting the case of the longest observed MCS at each of the five stations. Figure 4.3 shows temporal evolution of area of the MCSs. The longest observed MCS among these is at Kolkata, seen for nearly eight hours (Figure 4.3 a). Here, the MCS was first detected around 07 LST, its area rapidly increased in the next two hours, fluctuated around a mean for the next three hours and rapidly decreased in the last two hours. In the current study, these three time intervals are associated respectively with growth, mature and dissipation stages of the MCS. MCSs at other DWR stations had substantial stratiform area when they were identified for the first time, and moved out of radar range before fully dissipating. Figure 4.4 shows IMD radiosonde measured temperature profiles when the above MCSs were observed.

4.2. MCSs case studies

Temporal evolutions of MCSs (1 each at Kolkata, Hyderabad, Nagpur, Delhi and Patiala are shown in Figures 4.5 to 4.9, respectively. Each figure includes a satellite imagery depicting the position of the MCS in the large scale setting (e.g. Figure 4.5 a), projection of the columnar maximum Z_e showing an instantaneous 2-D structure of the MCS (Figure 4.5 b), pixels identified as convective (Figure 4.5 c) and rain rate at 1.5 km altitude (Figure 4.5 d). Storms correspond to more active convective cells, and temporal variation in the number of storms is included in the figures (e.g., Figure 4.5 e). The next set of sub-plots show total storm and convective areas, CAF and CPF, and associated rain volume rates. Cloud bands seen over Kolkata region on 2 September (Figure 4.5) were not associated with a monsoon synoptic system. A depression had passed over this area about 10 days earlier (Pai and Bhan 2013) and deep convection was mainly confined to east coast of India and foothills of the Himalayas. The MCS developed in an atmosphere having a deep moist layer (Figure 4.4).

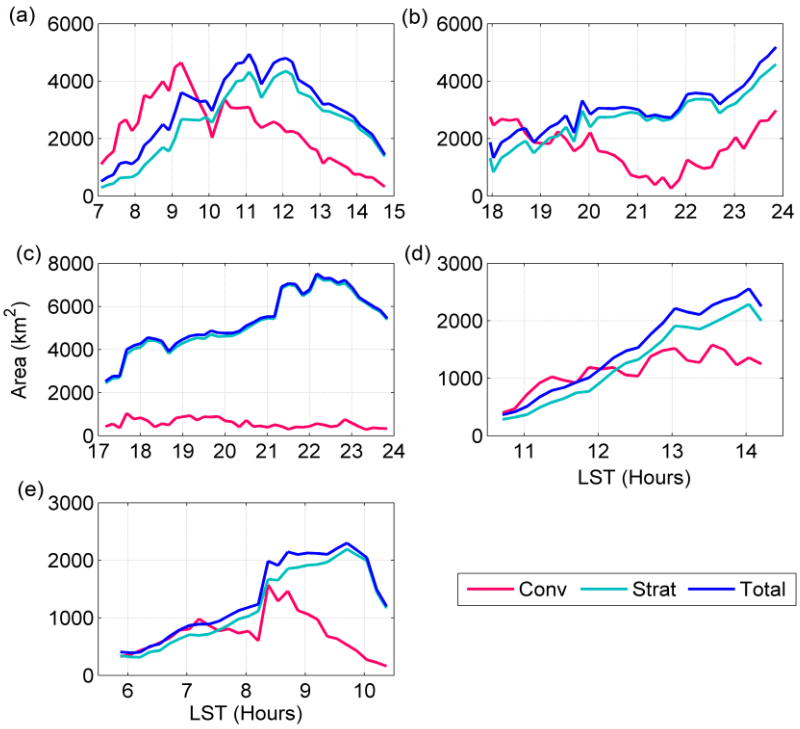

Figure 4.3. Temporal evolution of convective, stratiform and total area of MCSs observed on (a) 2 September 2013 over Kolkata, (b) 5 June 2013 over Hyderabad, (c) 13 June 2013 over Nagpur, (d) 11 June 2013 over Patiala and (e) 13 June 2013 over Delhi. Here the stratiform and total areas are divided by 5 so that areas look comparable and fit in the same graph.

Other MCSs shown, are formed in the northward propagating cloud bands during the monsoon onset phase (i.e., active phase of monsoon). MCS that formed at Kolkata on 2 September 2013 formed and dissipated within the radar range (Figure 4.5), and is discussed first. This MCS developed in the morning hours (Figure 4.5 e and h). Kolkata area has a diurnal variation in convection with more activity observed around 14:30 LST however, morning hours are also not uncommon (Sahany *et al*. 2010). Change in the number of storms between two volume scans is the net difference between new ones added versus old ones decayed within an MCS. It is observed that the number of storms does not increase or decrease monotonically with time during the growth as well as the decay stages (Figure 4.5 e). The growth phase is characterized by a rapid increase in the number, and the maximum of 23 is reached about an hour before the storm (and also MCS) area peaked (Figure 4.3). Convective area increased by more than three times in the first two hours (Figure 4.5 f), and then started decreasing. Nearly half of the convective area is occupied with storms. During the initial stages of development, 40 to 50% of the MCS area was convective which

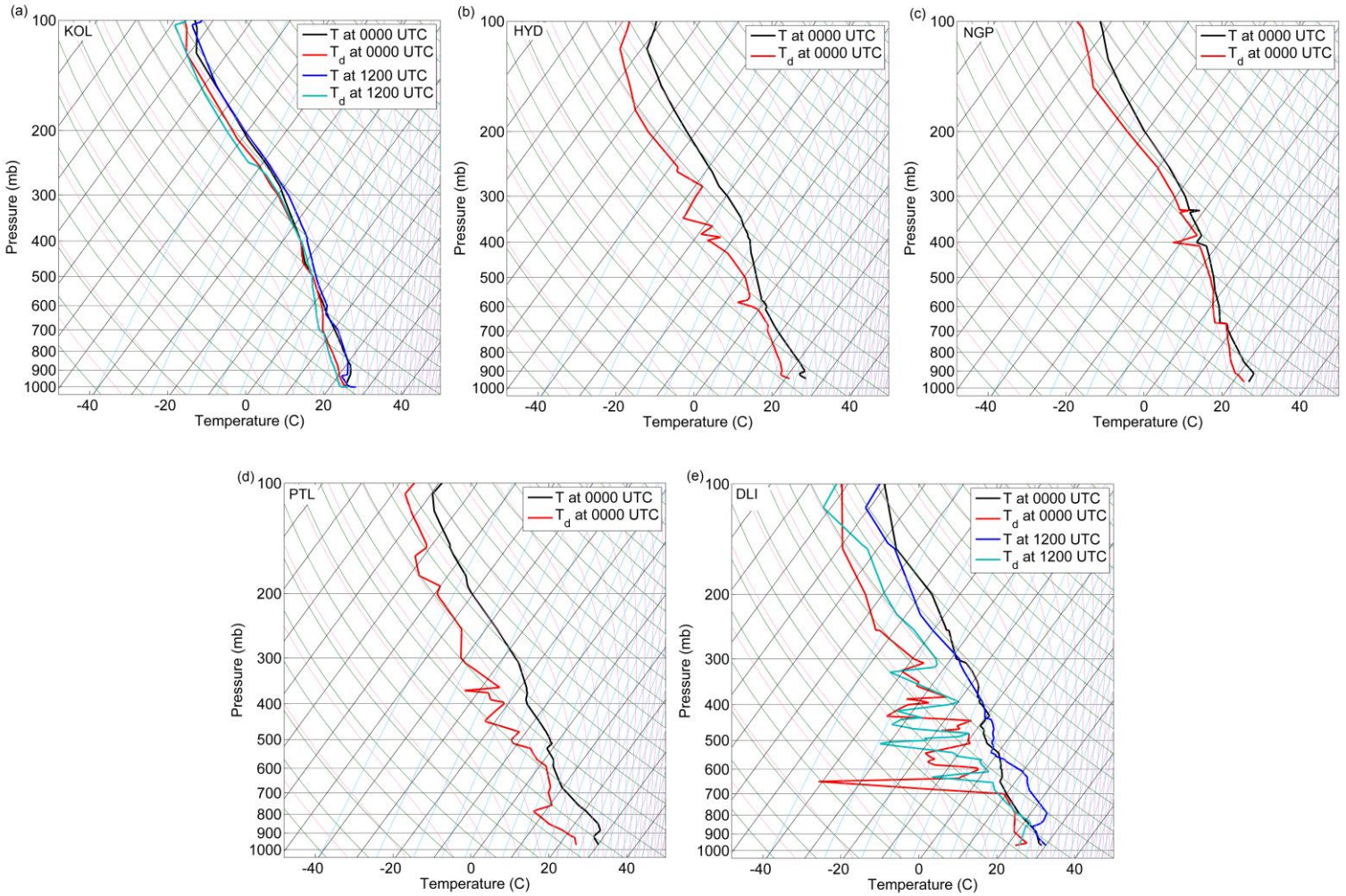

Figure 4.4. Skew-*T* log *p* diagram of temperature and dew-point temperature from radiosonde data measured over (a) Kolkata (2 September), (b) Hyderabad (5 June), (c) Nagpur (13 June), (d) Patiala (11 June) and (e) Delhi (13 June) in the year 2013.

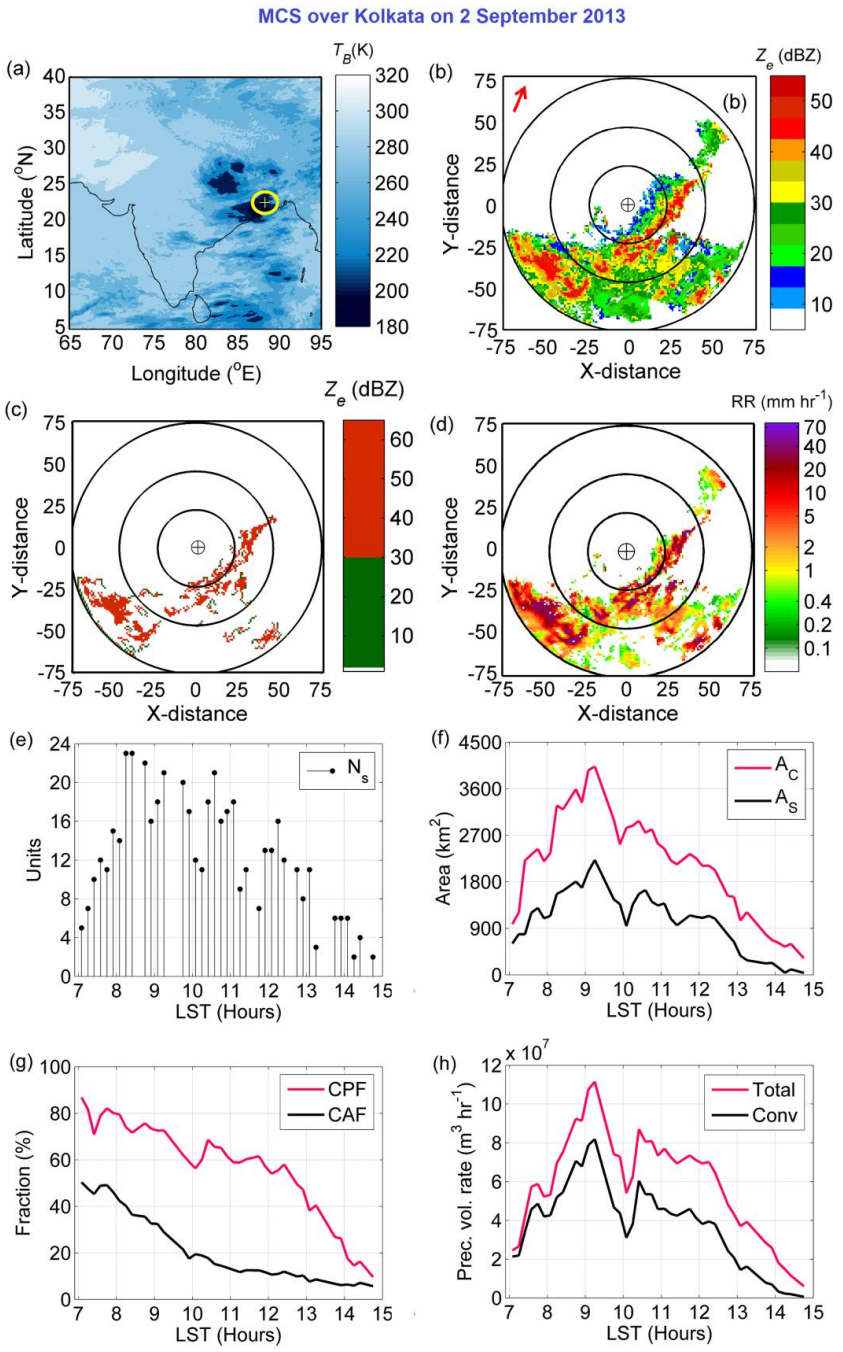

Figure 4.5. MCS observed on 2 September 2013 over Kolkata. (a) Satellite IR brightness temperature at 0904 LST. Circles shown here are 50 km distant each other having radius of outermost circle of 150 km. (b) Spatial extent of the MCS at 0900 LST revealed in the projection of the maximum Z_e between 2 and 3 km. Units of x- and y- distances are the number of pixels of the re-gridded data in respective directions, and the pixel size is 2 km × 2 km. Arrow at the top left corner points in the direction of the gross movement of the MCS around this time. (c) Pixels contain convective precipitation. Many of the pixels marked in red belong to storms. (d) Spatial distribution of the instantaneous rain rate at 1.5 km height. The color bar is in logarithmic scale. (e) Temporal variation in the number of storms embedded in the MCS. (f) Time evolution of total storm (As) and convective (Ac) areas within the MCS. (g) Convective precipitation fraction (CPF) and convective area fraction (CAF) and (h) total and convective precipitation accumulation rates.

contributed ~80% of the total precipitation (Figure 4.5 g). After the first half an hour, CAF started decreasing rapidly with time even as the convective area grew rapidly. This is owing to a faster increase in the stratiform precipitation area (Figure 4.3 a). While CAF reduced below 20% after two hours, CPF remained above 60% and the latter shows a slower decay rate compared to the former in the first 4 hours. Last three hours of the MCS saw rapid decrease in CPF from ~60% to less than 10% while CAF remained ~10%. Temporal variation of rain volume rate at 1.5 km altitude (Figure 4.5 h) closely follows that of the convective area (Figure 4.5 f).

Relative position of convective and stratiform echoes in an MCS is important for it reflects the dynamics behind the formation of new convective cells (Houze 1989). In squall lines for example, a line or row of convective cells are seen at the leading edge (cold outflow driven by downdrafts of precipitating clouds lifts high moist static energy air ahead facilitating development of new cells) with a trailing stratiform area (formed by the merger of old cells), a formation that is common in tropical cloud clusters (Houze 1989). In some of the MCSs, active convective cells are randomly distributed within a cloud system wherein local (e.g., land surface) features aid in the development of new cells (Houze 1989). In the MCSs over the main monsoon zone, both cases are observed (Figures 4.5-4.9). For example, convective echoes are arranged in L-shape with a prominent line formation at Kolkata (Figure 4.5 c). Resemblance of squall line/arch formation is seen at Patiala (Figure 4.8 c) and Hyderabad (Figure 4.6 c). MCS organization is less clear at Delhi (Figure 4.9) while convective pixels are randomly distributed at Nagpur (Figure 4.7). MCSs form both during the active and break phases of monsoon, and the phase of monsoon could influence MCS type. For example, in Australia, MCSs that form during the break monsoon are mostly squalls while convective bands embedded in stratiform regions are common during the active monsoon period (e.g., Cifelli and Rutledge 1998). MCS at Nagpur is not squall type and is dominated by stratiform echoes (Figure 4.3 and 4.7). As shown later, here stratiform precipitation dominates the monsoon seasonal precipitation. In northwest India (e.g., Patiala and Delhi), convection tends to be very intense (e.g., Zipser *et al*. 2006, Kumar and Bhat 2016), result of a combined effect of low level moist air flow originating from the Arabian Sea, local evaporation enhancing moist instability and a stable/drier lower troposphere that allows strong instability to build up (Romatschke and Houze 2011).

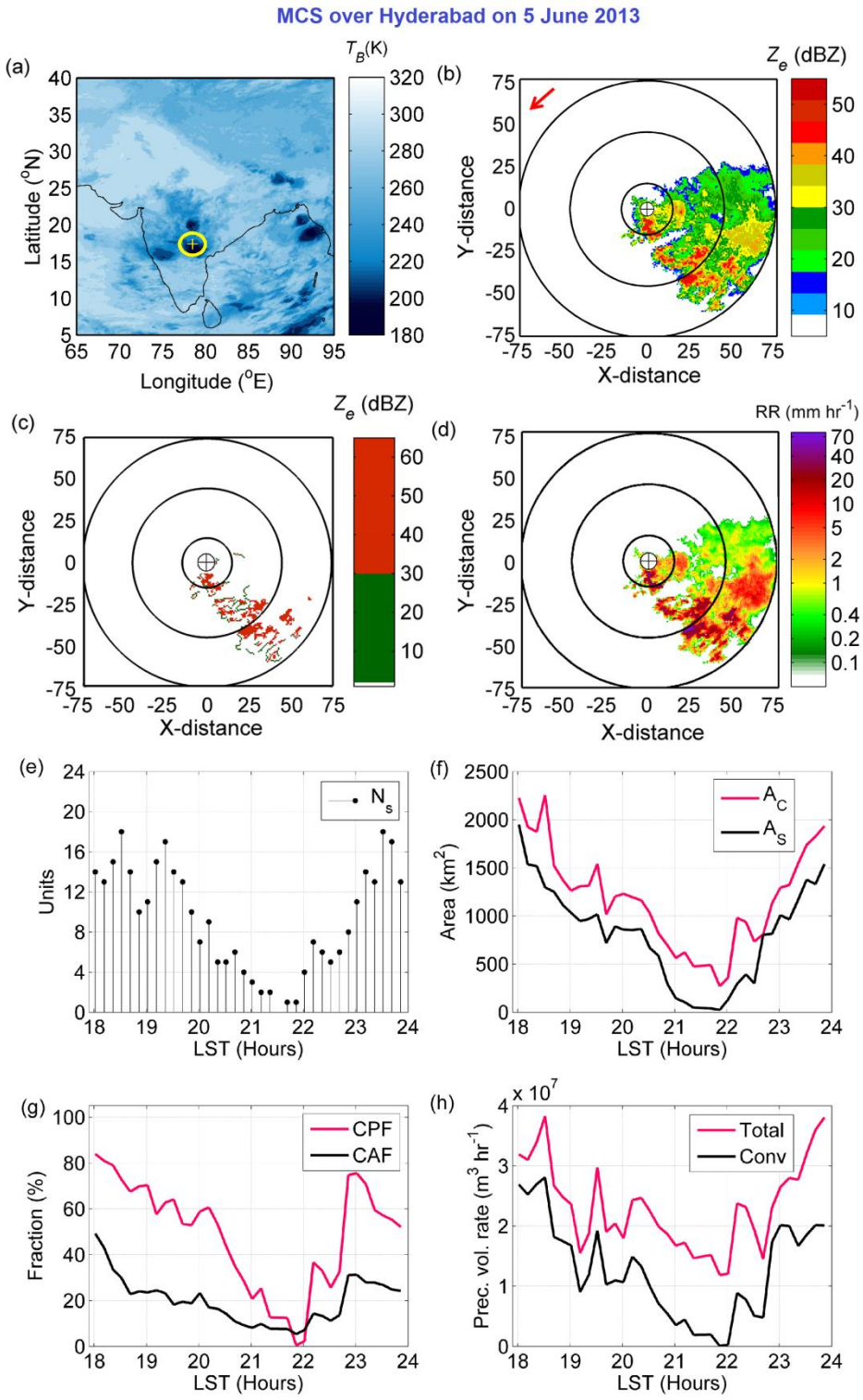

Figure 4.6. As Figure 4.5, but for MCS observed on 5 June 2013 over Hyderabad. Instantaneous snapshot is at 2330 LST.

Close examination of Figures 4.5-4.9 shows that temporal evolution of an MCS inferred from the variation in number of storms can be very different from that based on how MCS area changes with time. Within the life span of an MCS, there can be more than one intensification and decay phases if one goes by the number of storms. For example, the MCS at Hyderabad was past its formation stage when the algorithm first detected it (Figure 4.6) at 18 LST, the number of storms varied between 8 and 18 in the first two hours, thereafter, the number of storms decreased with time and reduced to 1 around 2140 LST (Figure 4.6 e). Number of storms increased after 22 LST again, reaching a maximum of 18 past 23 LST. While this was happening, the stratiform precipitation area was showing an overall a growth trend (Figure 4.3). Somewhat similar behavior is observed in the MCSs at Nagpur and Patiala. Storm is a sub-set of convective echoes. Convective area is mostly made of storms at Hyderabad (Figure 4.6 f), whereas storms occupy a small fraction of the convective area at Nagpur (Figure 4.7 f), and Kolkata (Figure 4.5 f), Patiala (Figure 4.8 f) and Delhi (Figure 4.9 f) fall between these two. CPF has large variation during the life cycle of an MCS. When convection is intensifying, CPF is more than 70% at Kolkata, and then gradually decreased with time, whereas at Nagpur, CPF is below 35% throughout (Figure 4.7 g). It is to be noted that CPF varies from one MCS to another at a given location, and sampling issue to be noted while comparing CPFs in Figures 4.5 to 4.9. This issue will be explored in upcoming section.

4.3. Average convective area and precipitation fraction

Average statistics of CAF and CPF calculated considering other MCSs at respective locations are shown in Figure 4.10 (a, b) respectively. CAF is the highest at Kolkata (mean ~13%) and the least at Nagpur (~4%). Mean CPF at Kolkata, Delhi and Hyderabad is ~40%, and the lowest (average ~13%) is observed at Nagpur. A 25-30% standard deviation of CPF basically arises from the large temporal changes in CPF during the life cycle of MCSs. CPFs shown in Figure 4.10 (a, b) are arithmetic averages (i.e., average of instantaneous CPF values in respective areas), and generally underestimate the actual contribution of convective precipitation to the accumulated rainfall. The ratio of accumulated convective precipitation and total (convective+stratiform) precipitation during the entire life span of the MCS (henceforth CPF_a) gives better estimation of the convective rain contribution. For the

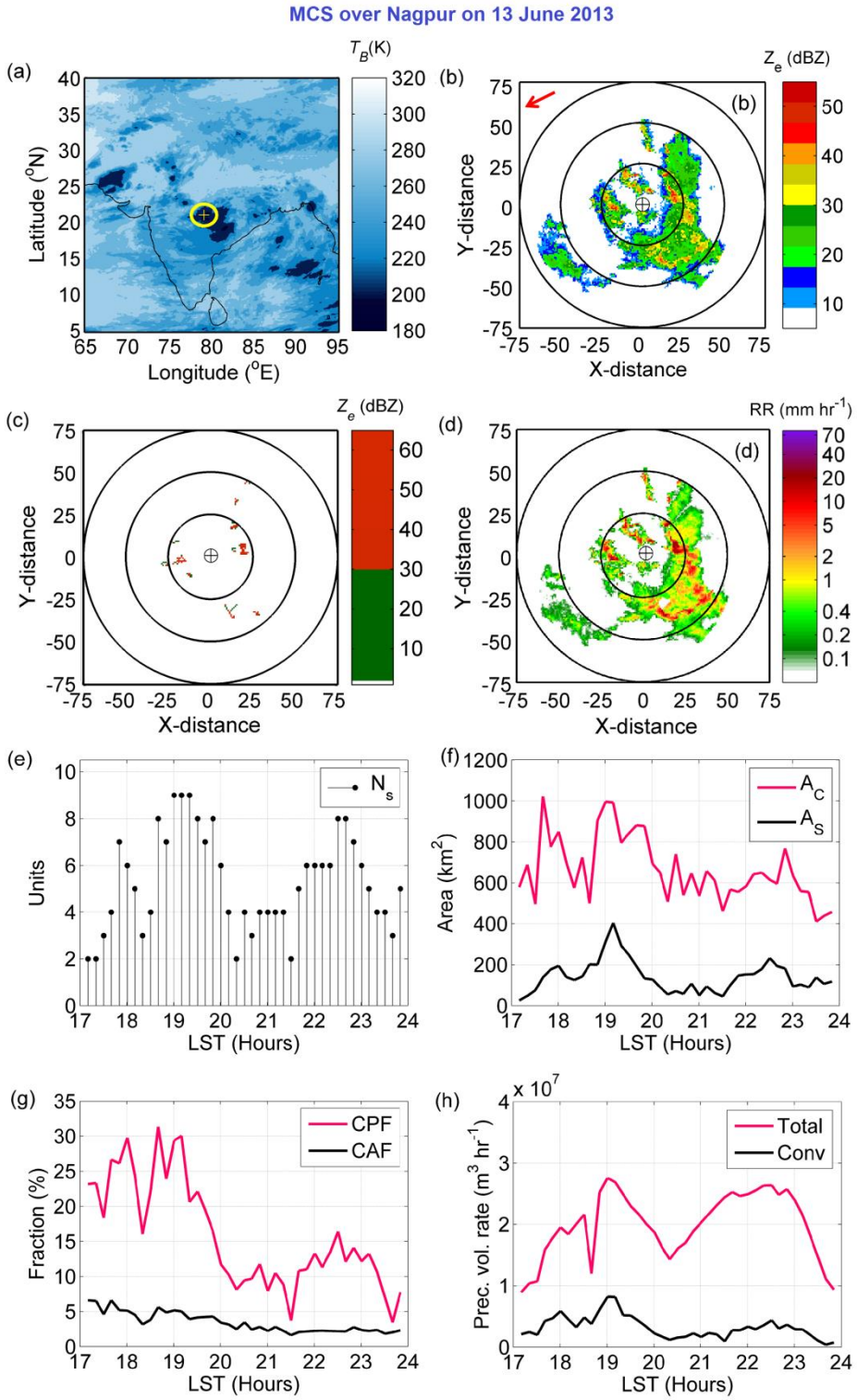

Figure 4.7. As Figure 4.5, but for MCS observed on 13 June 2013 over Nagpur. Instantaneous snapshot is taken at 1830 LST. CAF is rather small here, often less than 5%.

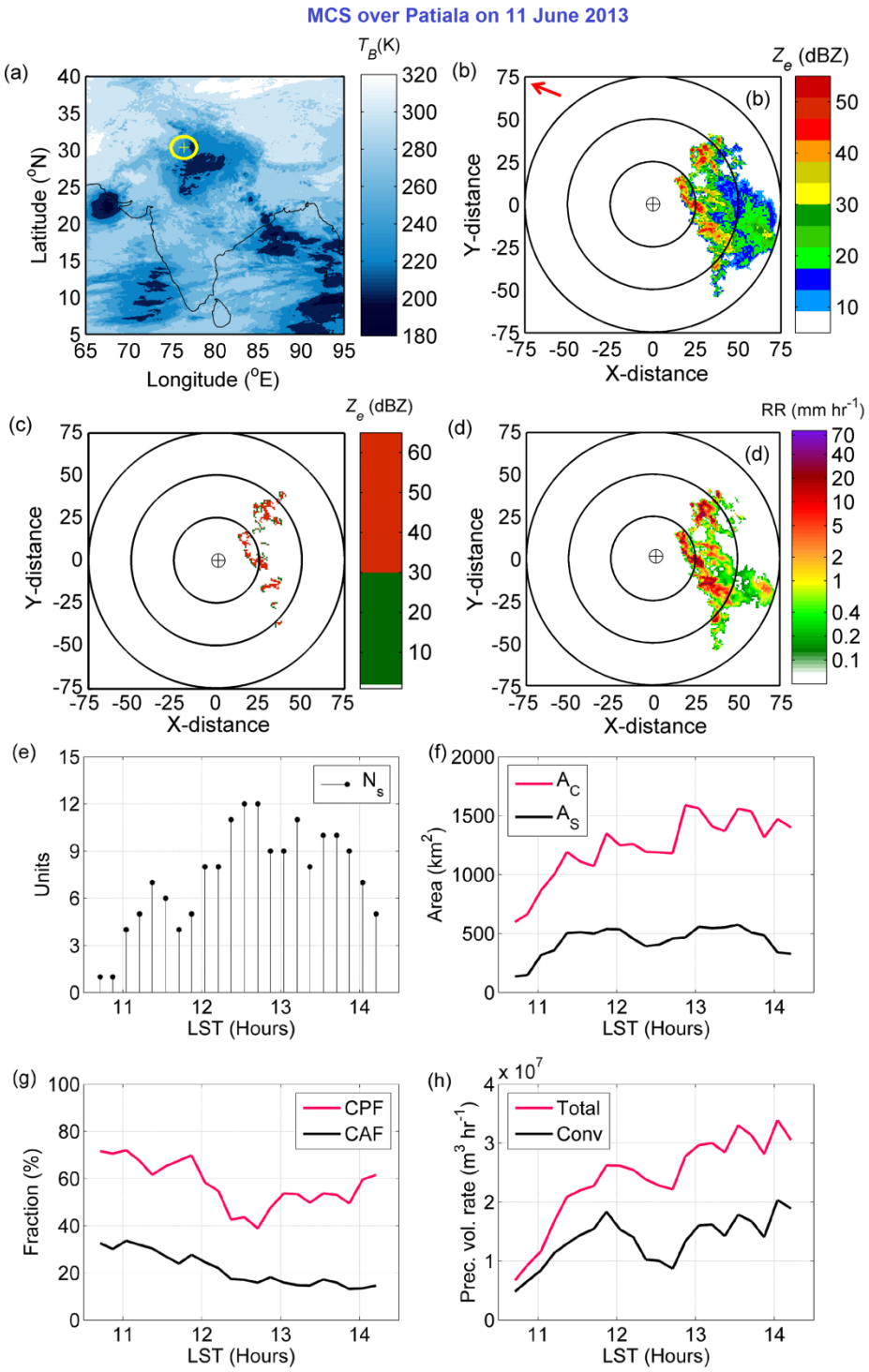

Figure 4.8. As Figure 4.5, but for MCS observed on 11 June 2013 over Patiala. Instantaneous snapshot is taken at 1300 LST.

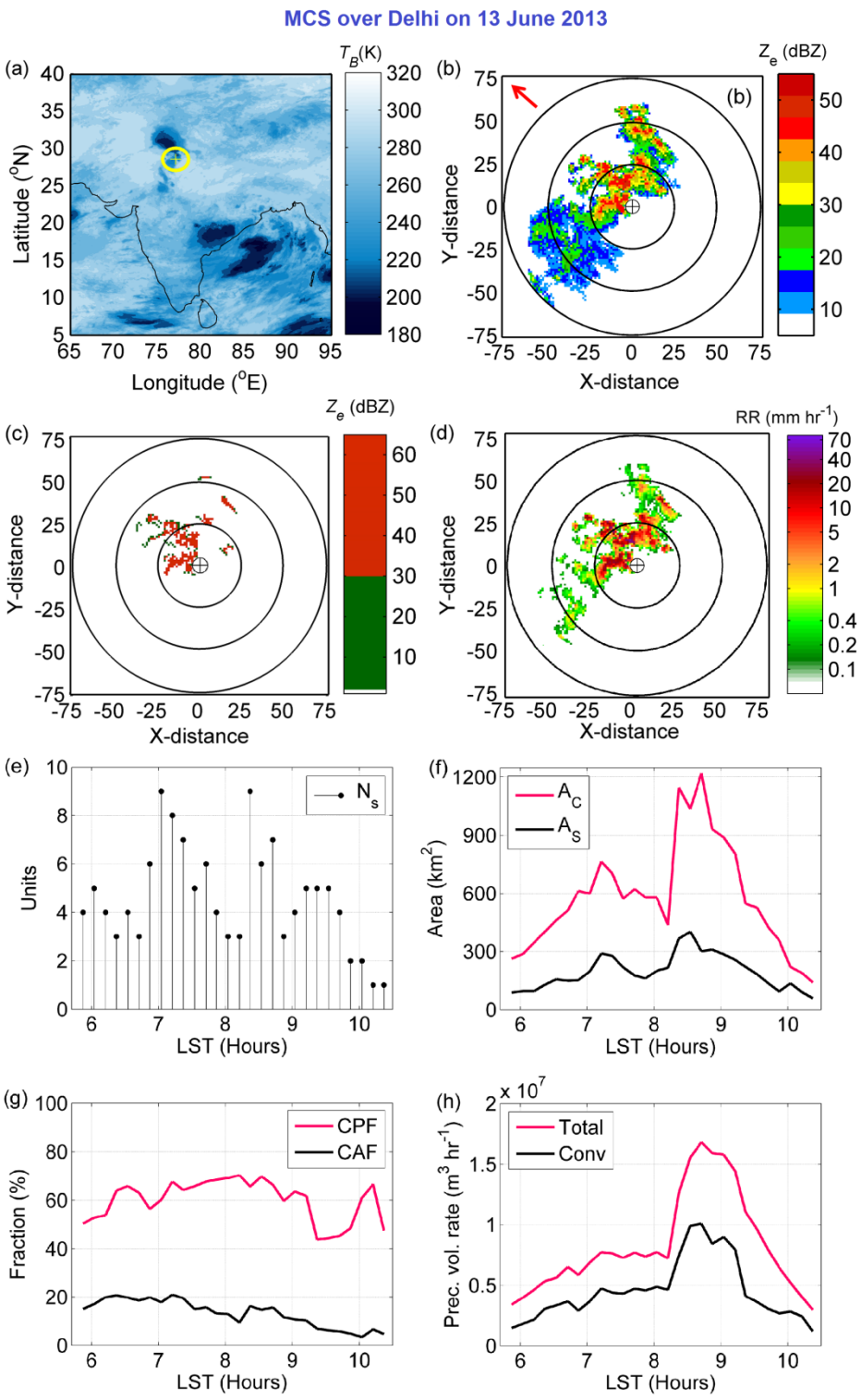

Figure 4.9. As Figure 4.5, but for MCS observed on 13 June 2013 over Delhi. Instantaneous snapshot is taken at 0830 LST.

studied here, CPF_a values are: Kolkata (63%, 39%, 24%); Hyderabad (59%, 54%); Nagpur (35%, 16%, 14%); Patiala (36%, 38%, 56%); Delhi (54%, 30%). One question that arises is the representativeness of CAF and CPF based on a few case studies of MCSs at different stations. Restricting the study to MCSs alone may miss out the true extent of convective contributions. Convective echo algorithm can be applied to any pixel within the radar range area. In order to better characterize the nature of monsoon precipitation, the same 2D map which was used to identify MCSs is considered for identifying convective pixels within the entire radar range area. Remaining cloudy pixels are treated as stratiform. This was carried out for all radar scan volumes of July-August months. This data is used to obtain average CAF and CPF for the two-month period, and the outcome of the exercise is shown in Figure 4.10 (c, d). Average CAF is <10% at all the five locations with Nagpur having the least value (~3%), followed by Hyderabad (4%), Kolkata (6%), Patiala (7%) and the maximum

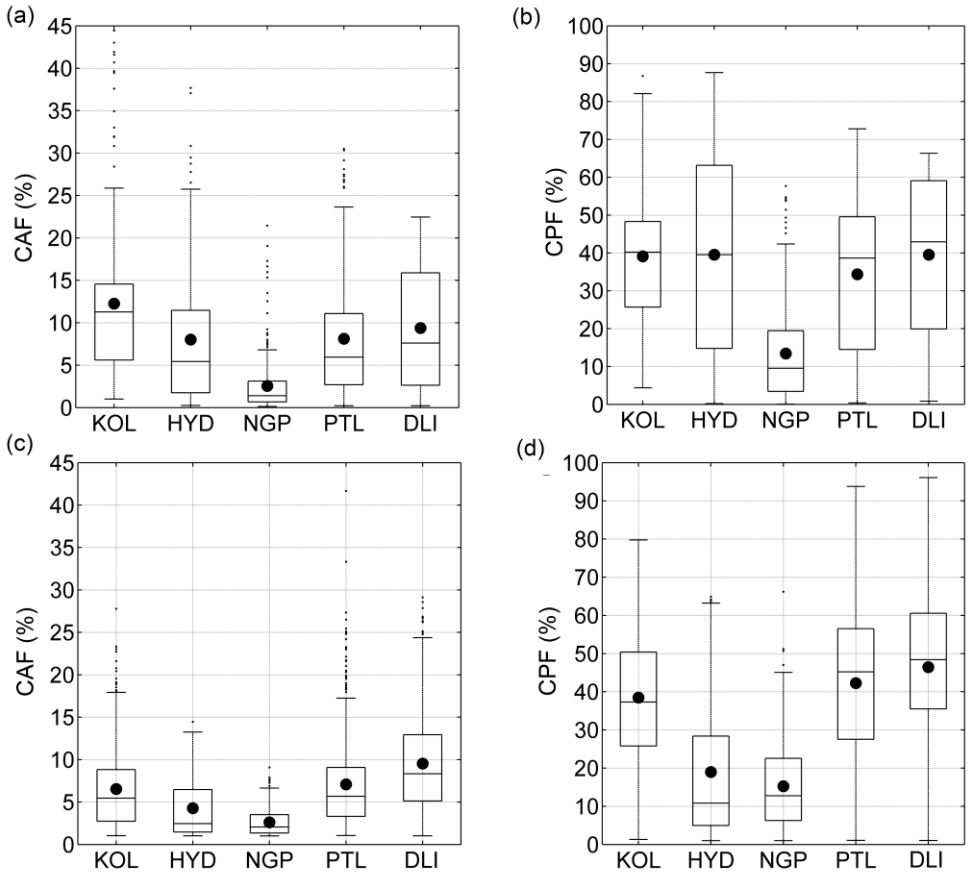

Figure 4.10. Statistics of convective area fraction and convective precipitation fraction for (a) and (b) for MCSs considered for life cycle studies and (c, d) for all clouds within 150 km radar range during July and August. All data are from S-band except for Delhi which is C-band. See Figure 2.1 for the station abbreviations shown along the x-axis. Filled circle and the horizontal bar nearest to it are the average and the median of the population, respectively.

at Delhi (9%). CPF also has the same order, but numerical values are different. Stations in central India, i.e., Nagpur (15%) and Hyderabad (19%) have low CPF, Kolkata and Patiala have ~40% and Delhi close to 50%. Therefore, in the southern part of the monsoon zone, stratiform precipitation dominates and convective precipitation fraction increases towards north. The pattern in the spatial differences seen in the mean values of CPF in Figure 4.10 are in broad agreement with the earlier studies of CPF based on the PR data, i.e., less in the southern parts of the monsoon zone and more in the north and towards the foothills of the Himalayas (Schumacher and Houze 2003; Pokherel and Sikka 2013; Saikranthi *et al.* 2014), however numerical values are different. These CPF values are found lower than those based on the TRMM PR data products.

4.4. Area and height of the storms

Temporal variation of average area of storms for the five MCSs is shown in Figure 4.11 (a). Storm area varied from less than 20 km^2 to more than 160 km^2. At Kolkata and Hyderabad, storm area peaked just before MCSs started dissipating. Average storm area is the lowest at Nagpur (between 20 and 30 km^2) and is more than 50 km^2 in other areas. How storm dimensions in the monsoon zone over India compare with those reported from elsewhere? The thresholds specified for storm identification in different studies are not unique, and therefore, direct comparison is not fair. During North American Monsoon Experiment (NAME) over the coast and Gulf of California, Lang *et al.* (2007) defined storm which contains at least 16 km^2 of convective echoes. Data from same NAME experiment is also used by Rowe *et al*. (2011) which assumes the storm area of at least 10 km^2 to track storms within MCS using TITAN. Despite the differences in the thresholds followed, it turns out that storm areas reported in different regions are not very different and lie in a few tens to a couple of hundred square kilometers range (e.g., Novo *et al.* 2014; Shah *et al.* 2015; Yang *et al.* 2016). In the hierarchy of convective cloud systems, 1-10 km size is called scale-D and cloud cells on this scale are also described as cumulus-scale cores of convective activity (e.g., Houze and Cheng, 1977). Storm height (defined as the average of the maximum height of individual storms in the MCS at any instant) is shown in Figure 4.11

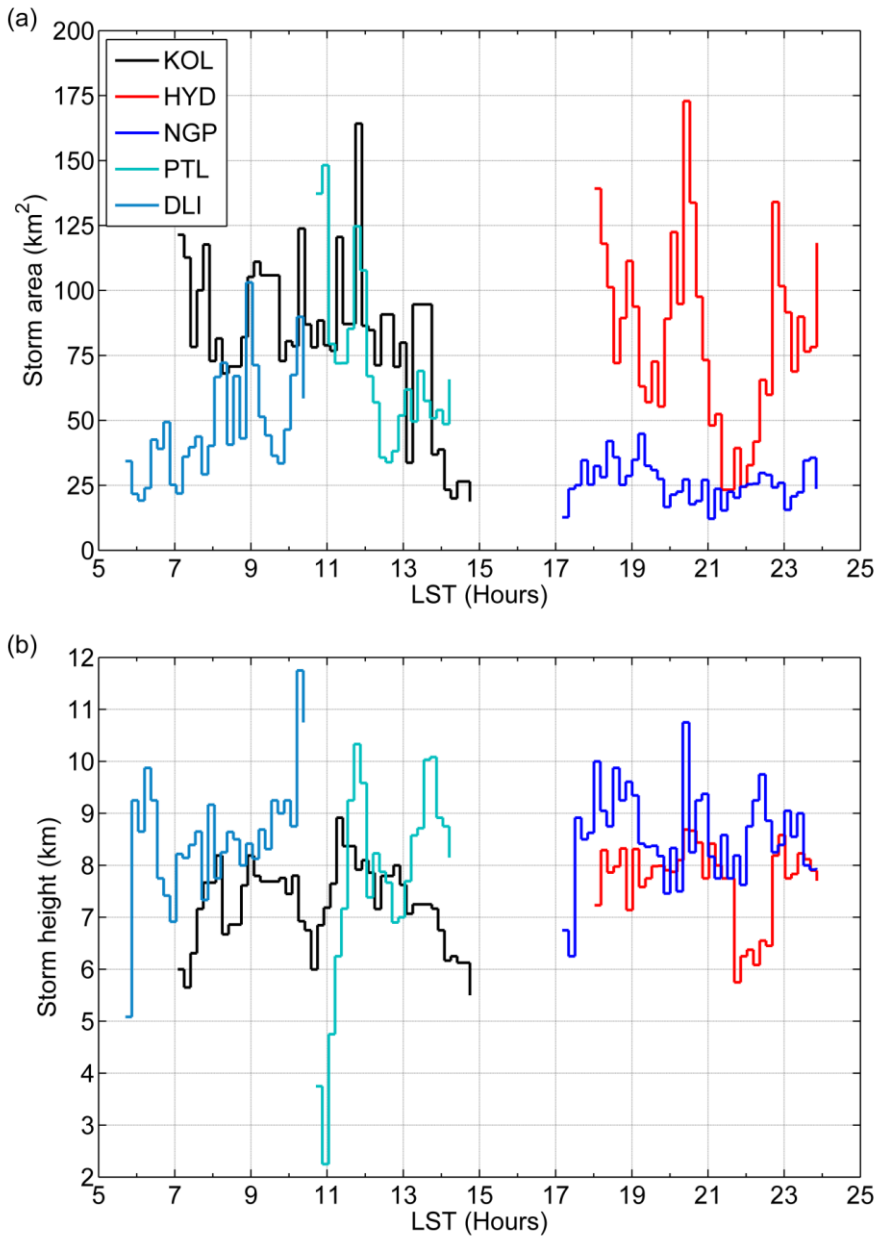

Figure 4.11. (a) Temporal variations of the average area of storms embedded in the MCSs shown in figures 4.5 to 4.9. (b) Average height of the storms. On average, storms at Nagpur are much narrower but their height is marginally more compared to the rest. In the dissipation stage of the MCS at Kolkata, both the number of storms and their area decreased.

(b). Note that storm is defined by the Z_e threshold of 30 dBZ and storm height in a way reflects the average height of the tallest 30 dBZ echoes in the MCS. Average storm height lies in 7 to 10 km range and storm height fluctuates on time scales of less than an hour. The highest storm height is observed at Delhi (11.5 km) and followed by Nagpur (10.5 km). Storm height decreased with time at Kolkata during the dissipation phase. Around the time

when the number of storms is the lowest at Hyderabad (Figure 4.6 e), the storm height is also found minimum (Figure 4.11 a). Previous study by Hirose and Nakamura (2002) suggests that the storm height during the season of May and October is around 6 km over Indian land regions. Mukhopadhyay *et al.* (2005) used IMD DWR observations at Kolkata to study the northwest storms. They found that the maximum storm height (outermost boundary of 30 dBZ echo) is around 16 km which indicates the signature of strong convective and lightning activities. Since MCS moved out of radar range at most locations, nature of storm height variation during the dissipation phase could not be ascertained.

4.5. ETH distributions

The maximum of echo top heights of 30 dBZ (henceforth ETH_{30}) and 40 dBZ (henceforth ETH_{40}) are used as measure of the intensity of convection (e.g., Zipser *et al.* 2006; Heymsfield *et al.* 2010). The presence of ETH30 and ETH40 above 10 km implies the presence of updrafts exceeding 10 m s^{-1} in the cloud (Heymsfield and Schotz, 1985; Heymsfield *et al.* 2010). Figure 4.12 shows the vertical distribution of ETH_{30} and ETH_{40} for convective echoes. The mode of ETH_{30} lies between 6 km and 8 km at Hyderabad, Patiala and Delhi, whereas the mode is around 3 km at Nagpur and below 3 km at Kolkata. ETH_{30} at Kolkata shows a secondary peak at 5.5 km. Patiala has the deepest ETH_{30} and more than 15% of them extend above 10 km, whereas, the corresponding number at Kolkata is less than 1%. Less than 50% of 40 dBZ echoes penetrate above 4 km (Figure 4.12 d), ETH_{40} peaks around 4 km (Delhi being an exception) and a very small fraction of 40 dBZ echoes are found above 10 km. Houze *et al.* (2007) termed 40 dBZ echo extending beyond 10 km altitude in the TRMM PR reflectivity field as deep intense convective echo. It is observed from Figure 4.12 (b) that their frequency is generally low everywhere, however in a relative sense, higher in Delhi and Patiala areas, a result consistent with the PR data based study by Houze *et al.* (2007).

4.6. VPRRs

For more in-depth information on vertical extent of convective part of MCS, the VPRRs for all MCSs observed at each DWR location are prepared. Figure 4.13 (a-e) shows location wise mean VPRRs with 1-standard deviation indicated. The tallest convective clouds are

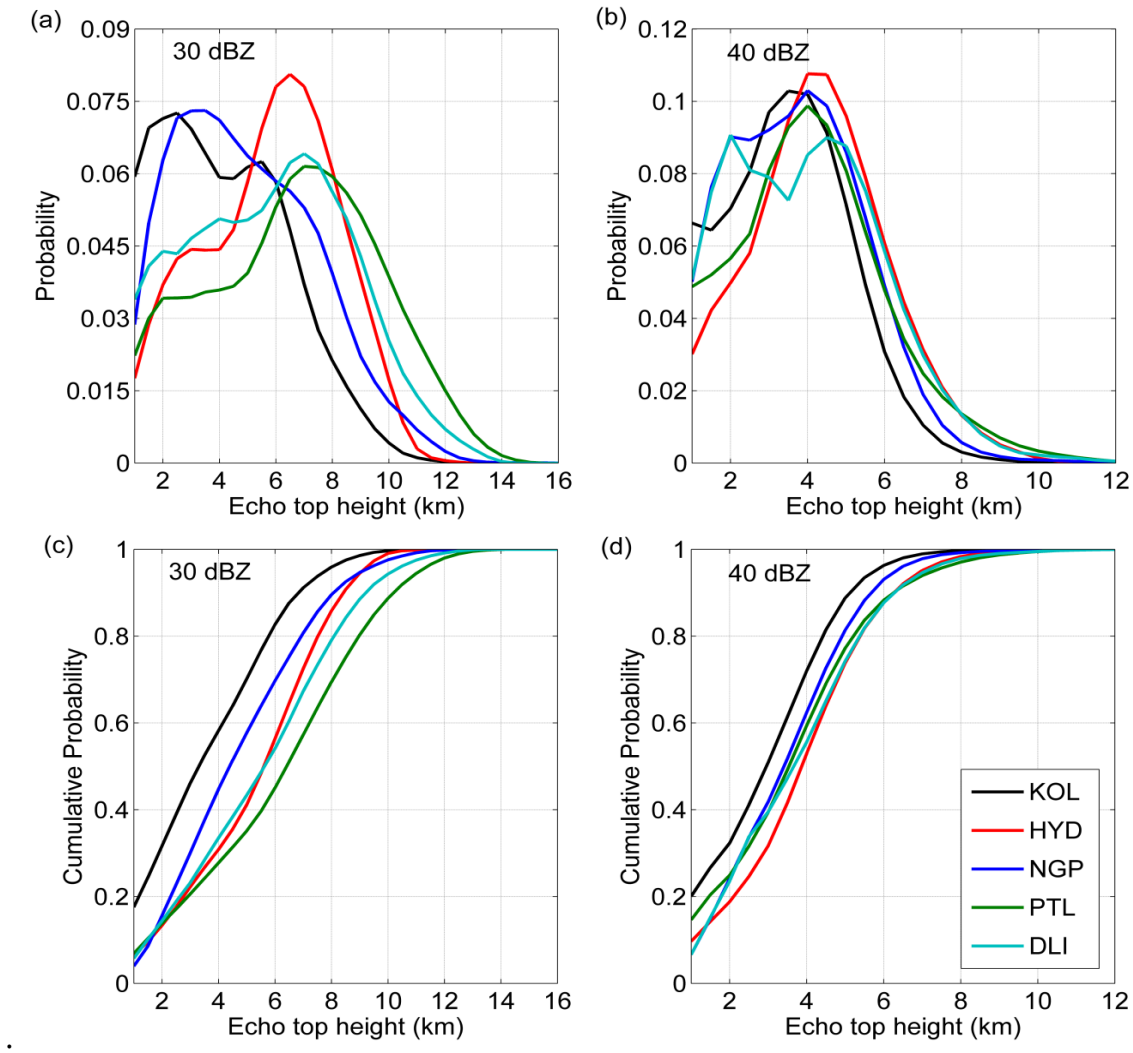

Figure 4.12. Distributions of echo top heights of 30 dBZ and 40 dBZ within convective echoes. (a-b) probability, (c-d) cumulative probability.

observed at Nagpur (~13-14.5 km) and Patiala. Patiala is in the vicinity of Western Himalayan foothills which earlier studies had identified as one of the locations favorable for intense convection (Zipser *et al.* 2006; Romatschke *et al.* 2010). The vertical extent of convective cells is the lowest at Hyderabad. In the mixed phase region (approximately between 5 km and 8 km), average VPRR (Figure 4.13 f) shows a rapid decrease with height at Kolkata and Delhi and a slower rate of decrease at the other three stations. The differences in VPRRs at the five stations are large above 8 km. This is the altitude where echoes of 30 dBZ exist (Figure 4.13 a-e). Patiala and Nagpur are the places, where echoes reaches higher (>14 km), indicates the presence of strong updraft, probably higher convective instabilities.

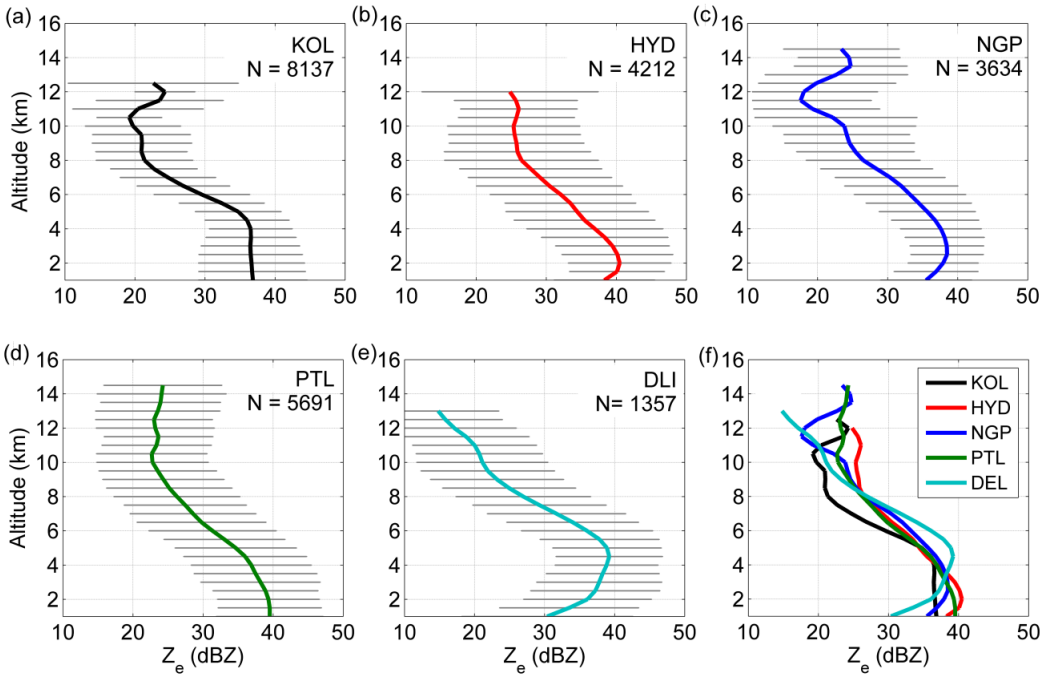

Figure 4.13. (a-e) Vertical profiles of radar reflectivity (*VPRR*) of convective echoes in MCSs. N is the total number of *VPRR*s and thick line is the mean profile of all *VPRRs.* The horizontal lines around the mean curve indicate 1-standard deviation of all *VPRRs*. (f) comparison of mean of all VPRRs at different stations.

The height at which VPRR peaks is also different at different places. VPRR peaks at 2 km at Hyderabad, at 2.5 km at Nagpur, at 5 km at Delhi and near to the surface at Kolkata and Patiala. Many factors are involved in deciding the shape of VPRRs that include phase change of condensed water between liquid and ice (e.g., Fabry and Zawadzki, 1995), cloud microphysical and dynamical processes (e.g., Heymsfield *et al.* 2010), and the humidity structure of the lower troposphere and intensity of convection (e.g., Liu and Zipser 2013). Fabry and Zawadzki (1995) discussed how the change in phase and shape of hydrometeors can change the vertical profiles of reflectivity especially when ice crystals cross the melting band and turn into liquid phase. Heymsfield *et al.* (2010) showed that the updrafts and downdrafts in both land and oceanic convective storms are higher in mid-troposphere (6-8 km) than sea-breeze and tropical cyclone storms. Generally higher values of low-level humidity favor an increasing Z_e towards the surface below the freezing level (e.g., Liu and Zipser 2013) and Kolkata profiles are in agreement with it (Figure 4.4). Delhi has a drier lower troposphere (Figure 4.4) which favors a decreasing Z_e towards the surface. Patiala profile remains a puzzle because the lower troposphere is dry (e.g., compared to Kolkata, Figure 4.4), but Z_e increases in this layer.

4.7. Summary

The temporal evolution of MCSs observed during the summer monsoon season are reported for the first time using the DWR data collected at five different locations in the main monsoon zone over the Indian subcontinent. An important part of the study is the identification and study of storms (convective cells) embedded in MCSs. Our results on CPF are in broad agreement with the results obtained from the PR data. The main findings are as follows. Growth phase is characterized by a rapid increase in the number of storms. Within the life span of an MCS that lasts for more than 5 hours, there can be more than one intensification and decay phases. MCS contains one or more number of storms depending upon their life phase. Storm area varies from less than 20 to more than 160 km^2. Average storm height typically varied in 6 to 10 km range. Average convective area fraction is the least at Nagpur (~4%) and highest (~13%) at Kolkata. Convective precipitation fraction can be as high as 80% during the initial growth phase of MCS and then decreases with time, often not monotonically. During the growth phase of MCS, convective area fraction decreases more rapidly compared to the convective precipitation fraction. Average convective precipitation fraction is 40% or below at all the five locations, higher at Kolkata, Hyderabad and Delhi (~40%) and the least at Nagpur (13%). Arithmetic average generally underestimates the actual contribution of convective precipitation to the total precipitation from an MCS. For example, convective echoes contributed 55% of the total precipitation at Hyderabad, i.e., nearly 15% more than the average value. The mode of 30 dBZ echo height lies between 6 km and 8 km at Hyderabad, Patiala and Delhi, whereas it is around 3 km at Nagpur and below 3 km at Kolkata. A secondary peak is observed near 5.5 km at Kolkata. Patiala has the deepest 30 dBZ echoes with more than 15% of them extending above 10 km. 40 dBZ echo tops peak around 4 km (Delhi being an exception) and only a very small fraction of them are found above 10 km. Average VPRR*s* at Hyderabad, Nagpur and Patiala show similarities in the mixed phase region while differences amplify above 10 km height however dissimilarities are noticed at lower and upper troposphere. These similarities and dissimilarities of VPRRs are governed by the peculiar microphysical and dynamical processes associated with the MCS observed at each DWR stations.

5

Properties of convective clouds measured by a polarimetric DWR at Delhi

It is stated in the literature that use of polarimetric variables improves the rainfall estimation (e.g., Bringi and Chandrasekhar 2001; You and Lee 2015; Yoon *et al*. 2016). A polarimetric DWR data enables better characterization of hydrometeors in clouds (Park *et al*. 2009). Utility of polarimetric DWR has not been tested under the Indian conditions. In this chapter, an analysis of the data collected with IMD's Delhi C-band polarimetric DWR is presented. Delhi is close to the Thar Desert and therefore convection is not frequent but can be intense when it occurs (Sikka 1997; Medina *et al*. 2010). For example, using the TRMM data, Zipser *et al.* (2006) showed that Northwest India and the foothills of the Western Himalayas are among the favorable locations for the occurrence of the most intense convective clouds on the Earth. Here deep and intense convective clouds with 40 dBZ echo area >1000 km^2 in horizontal dimension are known to occur (Houze *et al.* 2007). One of the important findings shown in the previous chapter is that MCSs contain storms which themselves could be made of several individual Cb (convective) clouds joined together. I considered Delhi as an ideal location to study storms using C-band polarimetric DWR data.

Regarding the large scale setting when the measurements were taken, IMD declared the onset of summer monsoon in southern India on 01 June in the year 2013, which happens to be the climatological onset date, and then the monsoon covered the entire country by 16 June, nearly a month ahead compared to the normal (Pai and Bhan 2013). Associated with the rapid progress of the monsoon, Delhi region experienced significant convective activity during June 10-16, 2013. This Chapter focuses on the convective

clouds that formed during the above period. Figure 5.1 shows a couple of satellite imageries captured by the Indian geostationary satellite KALPANA-1 and atmospheric vertical thermal structure for four days. Lower troposphere was moist during this period. Mid-troposphere was moister in the evening compared to morning, and the upper air thermal structure is characterized by rapid changes during this period, including a strong diurnal component.

Results are presented in the following order. In section 5.1, vertical structures of convective and stratiform echoes are presented. Storms properties (e.g., duration, area, size, etc.) are discussed in section 5.2. Section 5.3 gives the precipitation accumulation estimates using Z_h and polarimetric variable along with inter-comparison of both with rain gauge data. Vertical profiles of cloud liquid water content in storms are presented in section 5.4.

5.1. Vertical structure of convective and stratiform echoes

Figure 5.2 shows horizontal and vertical sections of cloud systems captured by the C-band DWR at three instants. In the top panel, randomly distributed pockets of convective areas are observed and the MCS in its early mature stage. Top of the convective clouds extend beyond 18 km, and the 30 dBZ echoes have penetrated 13 km. An hour later (middle panel), previous convective cells have weakened/merged, a few deep convective cells are present but cloud top height has decreased. The MCS is in late mature stage. An hour after this (bottom panel), area dominated by convective cells is occupied by stratiform echoes. It is not clear if the system was dissipating or moved out of the radar range. To see how Z_h is distributed vertically in these two classes of echoes at Delhi, VPRRs of convective and stratiform echoes during the period 6 June and 10-16 June are extracted and their CFADs are shown in Figure 5.3. Note that CFAD shows the spread among radar echoes at each altitude. It is observed from Figure 5.3 that the minimum value of convective echo, which is around 22 dBZ at lower levels increases with height

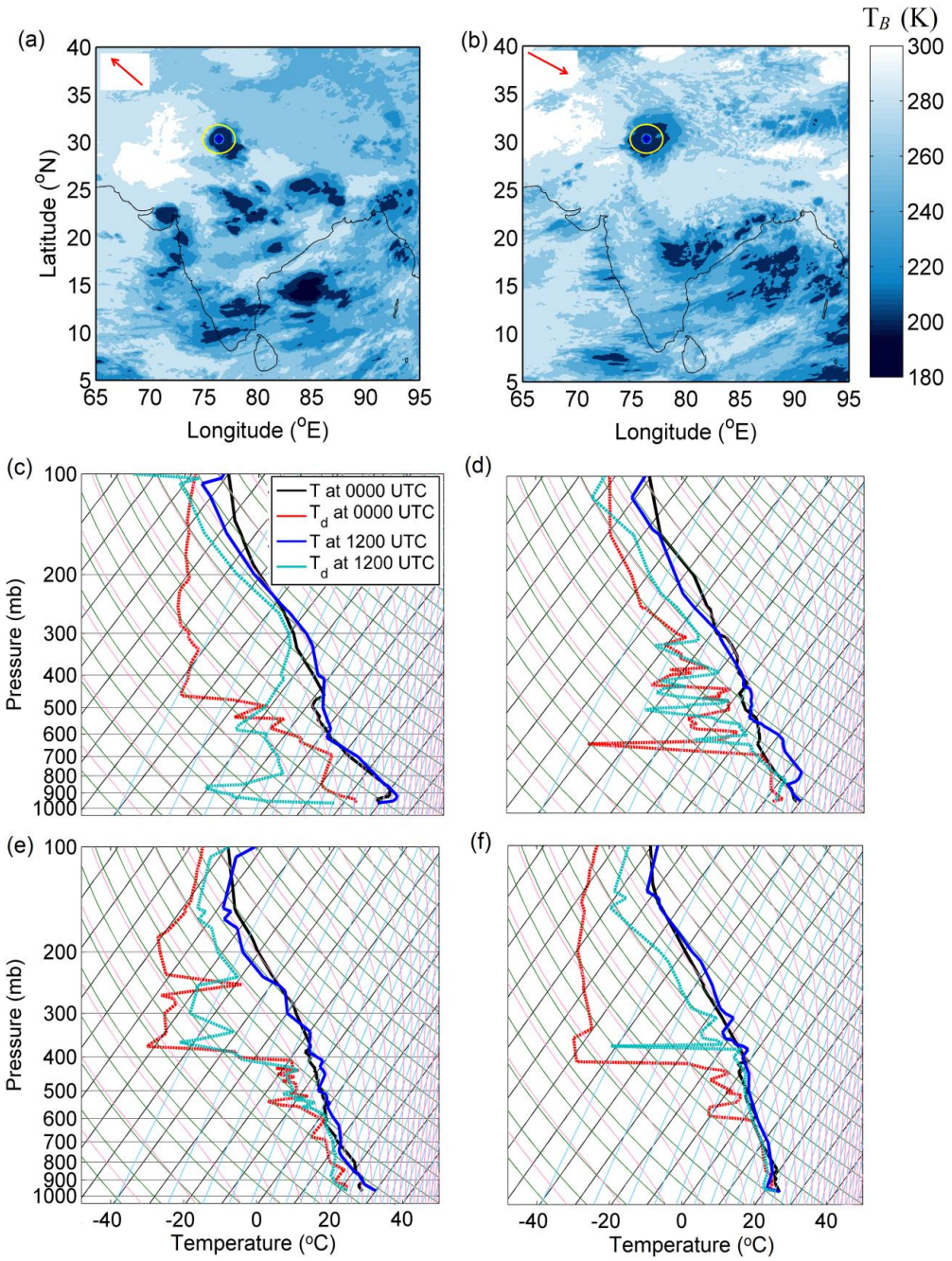

Figure 5.1. Top: KALPANA-1 IR brightness temperature, left: 11 June, 2013 at 1300 LST; right: 13 June, 2013 at 0830 LST. Lower panels: Skew-*T* log*p* diagrams of temperature and dew-point temperatures at Delhi on 10, 11, 13 and 14 June in the year 2013. Line legend is same in all sub-plots.

to 35 dBZ at 4 km, whereas the maximum value of Z_h increases from ~52 to ~54 dBZ in the same height range. Above 4 km, both the minimum and maximum values of Z_h decrease with height, the minimum more rapidly. Since Z_h values below 10 dBZ are not included in this plot, change in slope of the minimum Z_h as well as the natures of CFADs are not accurate above 8 km.

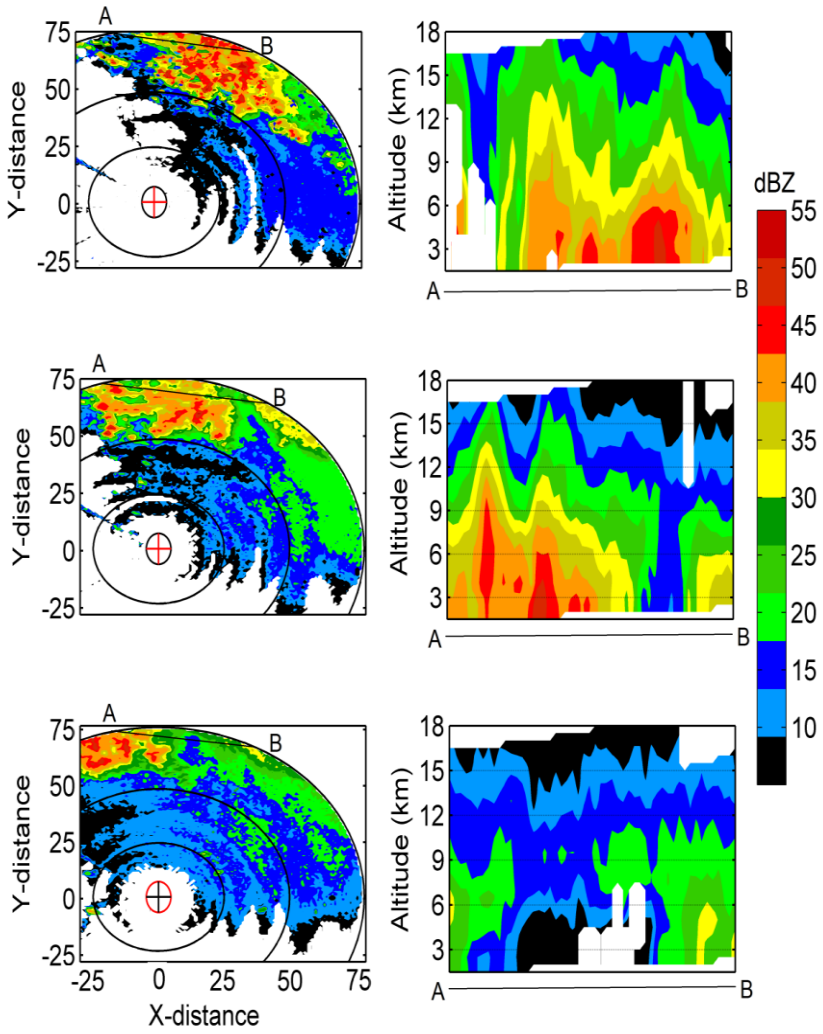

Figure 5.2. Left panel shows the projection of column maximum Z_h. Right panel a vertical section long line AB shown in left panel. Date is 11 June 2013 and top, middle and lower panels were observed at 0530 IST, 0630 IST and 0730 IST, respectively.

For the same reason, in the CFAD of the stratiform echoes, the lower limit could be biased. The maximum value of stratiform Z_h increases with height from 30 dBZ to ~38 dBZ at 4 km, then decreases with height and reaches at minimum Z_h value of 12 dBZ near 12 km. The highest reflectivity values in both the cases are observed around 4 km height. Altitude of the 0°C isotherm is ~4.8 km during the study period. Noting that the radar beam width increases with distance and is more than 1.5 km at 100 km range, radar cannot capture the height as well as the thickness of the melting layer or bright band accurately. Given this limitation, the peak Z_h seem to be located in the melting layer, and the bulge around this height in the CFAD contours of stratiform echoes suggests the

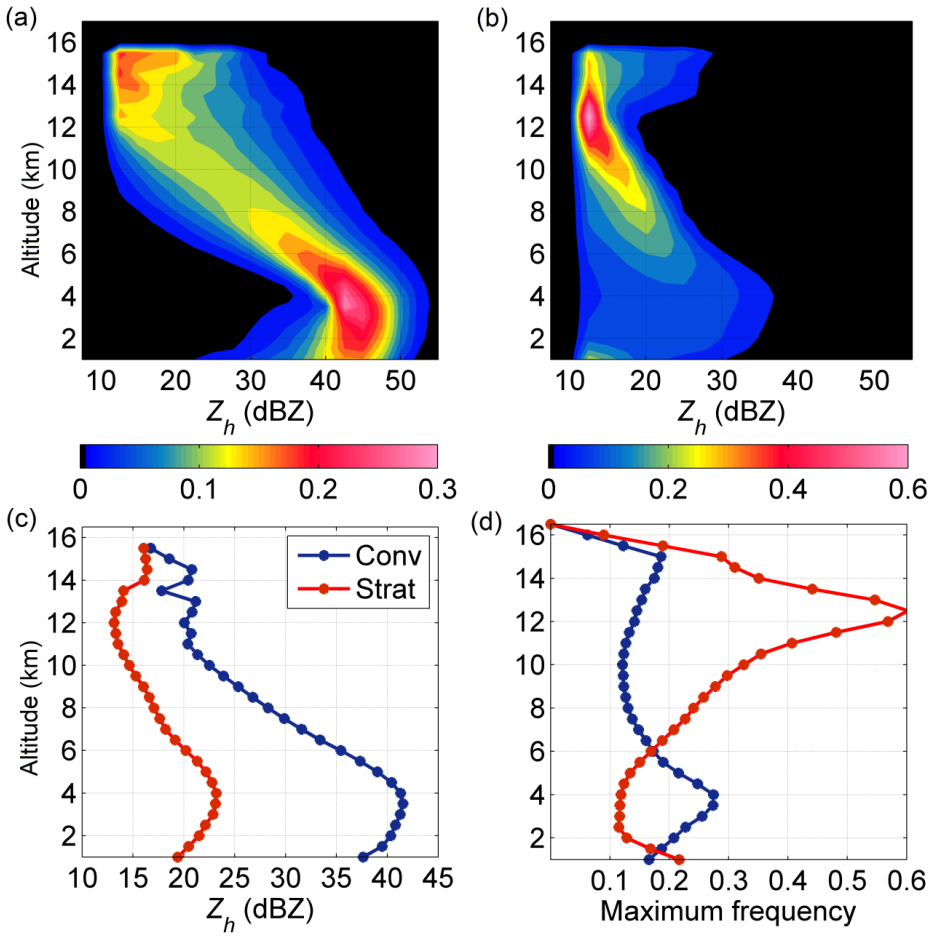

Figure 5.3. Contoured frequency by altitude diagrams (CFADs) for (a) convective and (b) stratiform cells. Variable used is Z_h. Color bars for panels (a) and (b) show the frequency of radar echoes. Panels (c) and (d) show the vertical profiles of mean Z_h and the maximum frequency of occurrence of Z_h, respectively.

presence of bright band (Figure 5.3 b). The mean of convective CFAD shows an increasing value with height between 2 and 4 km, and then decreases rapidly above 4 km (Figure 5.3 c). Peak frequency of occurrence in the distribution of Z_h increases with height initially, peaks at 2.5 km and then rapidly decreases with height for convective clouds (Figure 5.3 d). The shape of the average Z_h profile is closely related to cloud microphysical processes, cloud dynamics and phase change of water between liquid and ice (Fabry and Zawadzki 1995; Bhat and Kumar 2015). Shape of the average profiles in Figure 5.3 are similar to that obtained from S-band DWR data except for the altitude of highest reflectivity (which is at 5 km for the S-band DWR (Figure 4.13e) while is noticed at 4 km from C-band DWR). Maximum reflectivities in the mean profiles differ by ~4 dBZ (see Figures 4.13e and 5.3c). The average profile of stratiform echoes shows a peak around 4 km, a rapidly decreasing trend towards the surface. Both evaporation (if the sub-cloud layer is dry) and break up of rain drops make Z_h to decrease towards the

surface below the cloud base (Liu and Zipser 2013). Increasing frequency of occurrence in the distribution *of* Z_h implies that more number of clouds is similar to each other at that altitude. The trend is opposite for the stratiform clouds with a maximum between 14 and 15 km.

5.2. Storm properties

In this section, the statistics of the instantaneous and average properties of storms are discussed. The total number of individual storms identified during 6 June and 10-16 June 2013 is 507. Figure 5.4 (a) shows the distribution of storm duration. It is found that the storm survives typically for an hour while few exceed 3½ hours. More than one-third of these individual storms propagated at speeds of 30 km hr^{-1} or more whereas majority of the storms move with speeds of 25 km hr^{-1} or less (Figure 5.4 b). The typical movement of the storms is in northwest and southeast directions (Figure 5.4 c). Few storms have their peak area as large as 400 km^2 (Figure 5.4 d). The horizontal structure of Z_h and a vertical section through an intense storm observed at 0700 LST on June 11 is shown in Figure 5.4 (e, f). All the pixels in this storm are connected in 3D space and pixels having Z_h>42 dBZ constituted an area of 480 km^2 (in horizontal projection) and have maximum vertical extent of 8 km. These are massive storms or intense convective clouds.

The temporal evolution of properties of the long-lived storm (3½ hours) is shown in Figure 5.5. The maximum Z_h (Z_{max}) remained above 52 dBZ for more than 3½ hours, with the peak value of 62 dBZ (Figure 5.5 a). The echo top heights (ETHs) of 30 dBZ and Z_{max} echoes are more than 16 km and between 2 and 5 km respectively (Figure 5.5 b). The mean Z_h varied between 40 and 46 dBZ. These numbers indicate that this storm was very severe and intense in nature. The Z_{max} occurred around and below the 0°C isotherm with an average height ~4.5 km. Except for the early 30 minutes or so of storm's life span, ETH of the 30 dBZ echo remained above 10 km. When 30 dBZ echo is observed at 10 km level, it suggests strong lightning activity (Zipser and Lutz 1994; Liu *et al.* 2012). The storm area remained more than 100 km^2 most of the time and attained a maximum size of 450 km^2 (Figure 5.5 c). The storm volume and area together (Figure 5.5 c) suggest that the thickness of the storms (i.e., average depth of 30 dBZ reflectivity layer) was nearly 10 km.

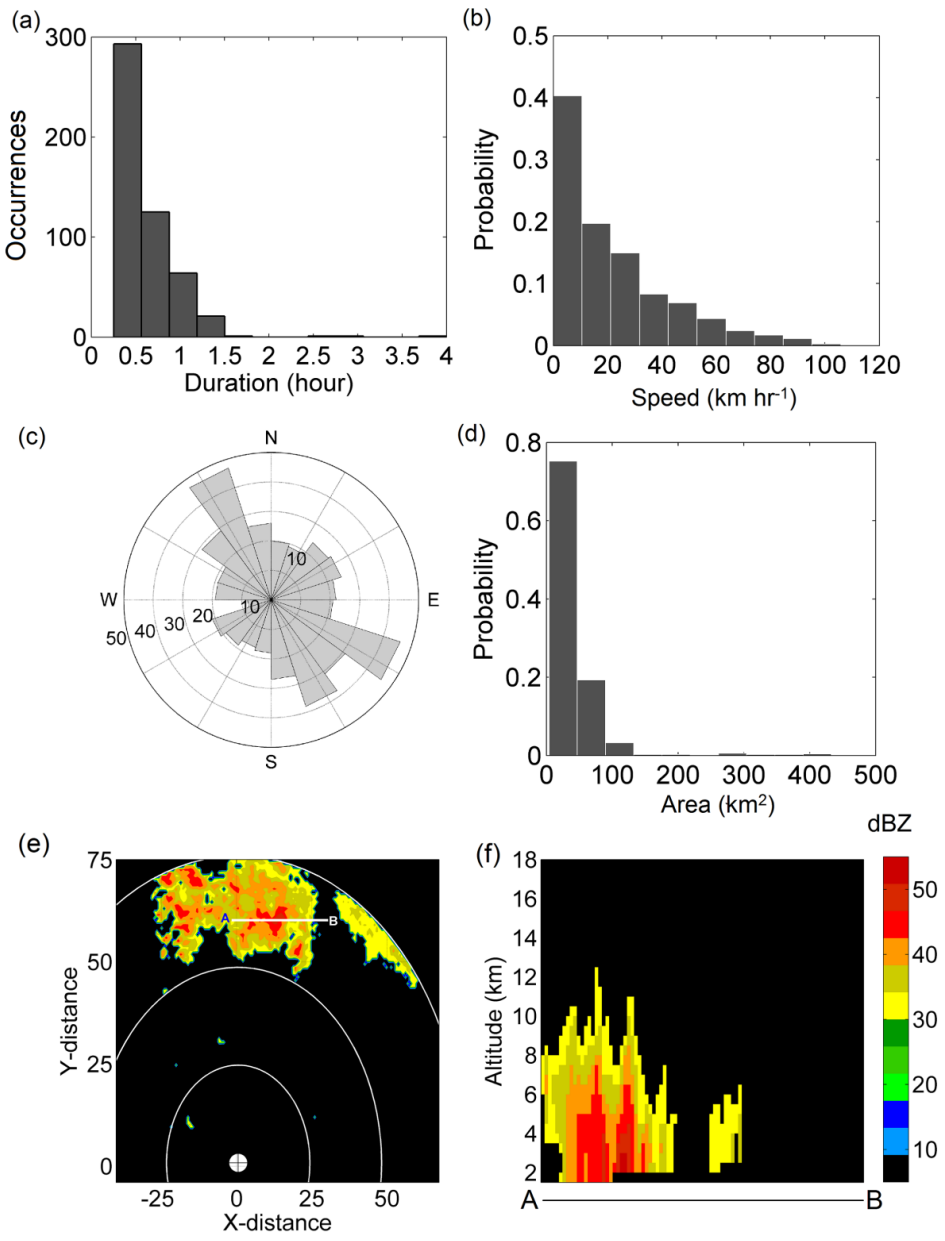

Figure 5.4. Storms characteristics: (a) Life duration, (b) Propagation speed, (c) Propagation direction and (d) area. (e) Horizontal projection of the columnar maximum Z_h and (f) Vertical section taken along line AB for storm observed on 11 June at 0700 LST whose area exceed than 400 km^2.

Figure 5.6 illustrates the relationship among few of the properties of storms averaged over their life duration. To understand if any relation exists between average area of storms and their duration, their scatter plot is shown (Figure 5.6 a). It is found that there is no clear relation between the two, however those that lived longer than 1.5 hours had attained an average area of more than 100 km^2. The average precipitation amount resulting from storms shows an increasing trend with the area time integral (*ATI*)

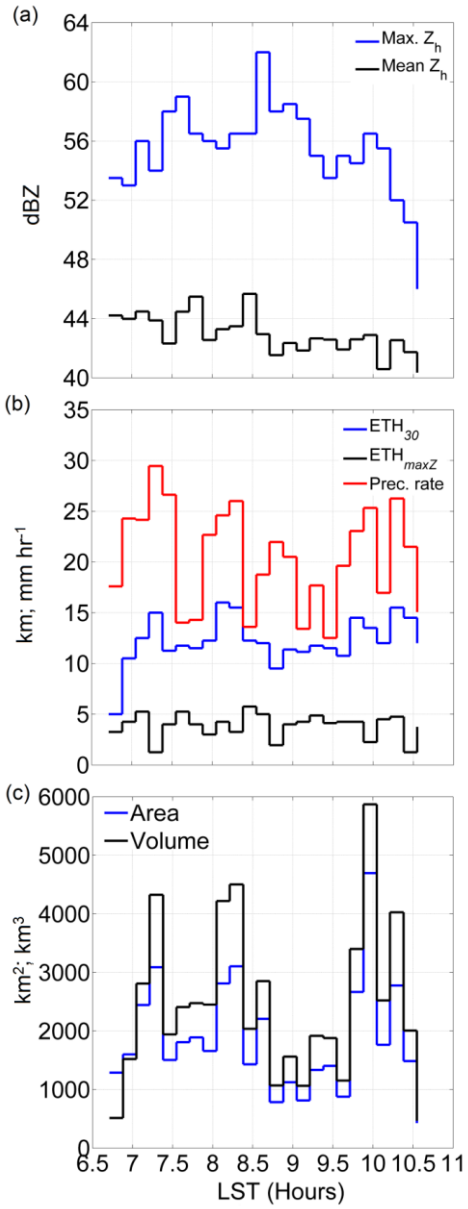

Figure 5.5. (a-c) Temporal evolution of properties of long-lived storm (~3½ hours) observed on 13 June 2013. (a) Maximum and average values of Z_h, (b) ETH of 30 dBZ and Z_{max} echoes and precipitation rate calculated at an altitude of 1.5 km. Precipitation rate is expressed in mm hr^{-1} units, (c) Area and volume. Note that the area is multiplied by 10 to fit the two curves in the same plot.

especially for storms having large average area and longer duration (>1.5 hours) (Figure 5.6 b). There is no relationship between average precipitation amount and maximum ETH (Figure 5.6 c). It suggests that even if a storm attains high vertical extent, it may not yield higher precipitation amount. It also must be noted that the precipitation amount is calculated referring to Z_h field at 1.5 km altitude and it may not exhibit any relation with ETH. The relationship between *ATI* and radar estimated rain volume (*RERV*) is almost

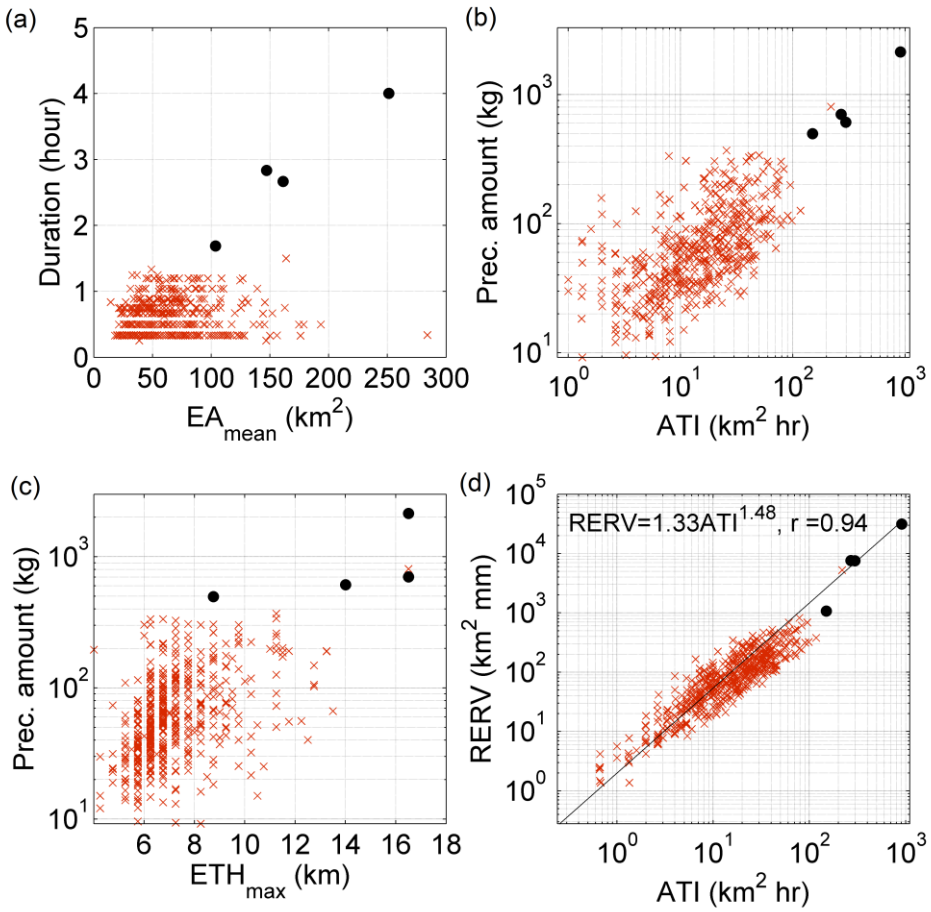

Figure 5.6. Average characteristics of storms: (a) Scatter plot between mean echo area (EA_{mean}) and storm life duration. (b) Scatter plot between mean echo area and area time integral ATI. (c) Scatter plot between maximum echo top height and total precipitation amount expressed as mass of rain water. (d) Scatter plot between ATI and total precipitation amount. The symbols '×' and 'filled circles' correspond to storms with life duration of less and more than one and half hour, respectively.

linear on the log-log scale implying a power law relation between the two (Figure. 5.6 d). The calculation based on coefficient obtained from their power law estimates, the average precipitation rate in storms is in 5 to 34 mm hr^{-1} range (see section 2.7 for calculations).

5.3. Total accumulated precipitation

One of the main advantages of a polarimetric DWR over single polarization DWR is a better estimation of cloud liquid water content and precipitation (Bringi and Chandrasekhar, 2001). To understand the impact of including polarimetric variables in the estimation of rain rates and total accumulated precipitation, four different relations

for R using Z_h and K_{dp} are considered (Table 2.4) To find how much amount of precipitation is received over Delhi during June 6 and June 12-16, the total accumulated precipitation (P_{acc}; in mm) is derived. The precipitation is calculated at CAPPI of 1.5 km altitude. The probability and cumulative probability distributions of rain rates derived from Z_h and K_{dp} variables are shown in Figure 5.7. Probability of rain rate estimates derived from Z_h is higher at lower rain rates and rapidly decrease as R increases. In case of K_{dp} derived R, the probability is less for smaller R, shows much smaller decrease with R as R increases beyond 20 mm hr^{-1}. K_{dp} derived R estimations show higher rain rates, with a maximum up to 120 mm hr^{-1} (Figure 5.7 a). About 90% of Z_h derived R lies below 40 mm hr^{-1} while more than 35-40% of K_{dp} derived R is found beyond the 40 mm hr^{-1} (Figure 5.7 b). The maximum P_{acc} derived from K_{dp} is found up to 250 mm or more however P_{acc} calculated from Z_h is found less than 25 mm (Figure 5.8). To check which estimate is better, rain gauge rainfall data of IMD rain gauge network is compared with DWR derived rainfall (Figure 5.10). The rain gauge locations around Delhi DWR are shown in Figure 5.9. For comparison of gauge rainfall with that derived from DWR, the mean and standard deviation of the precipitation of all 9 pixels (each pixels' area is 4 km^2) at CAPPI of 1.5 km around each rain gauge location are estimated. It is observed that the P_{acc} from Z_h using (1) Iguchi *et al.* 2000 and (2) Hunter *et al.* 1996 (for convective precipitation) and Marshall and Palmer (1948) (for stratiform precipitation) as adopted by National Weather Service (NWS) are highly underestimated compared to rain gauge rainfall. The normalized bias and root

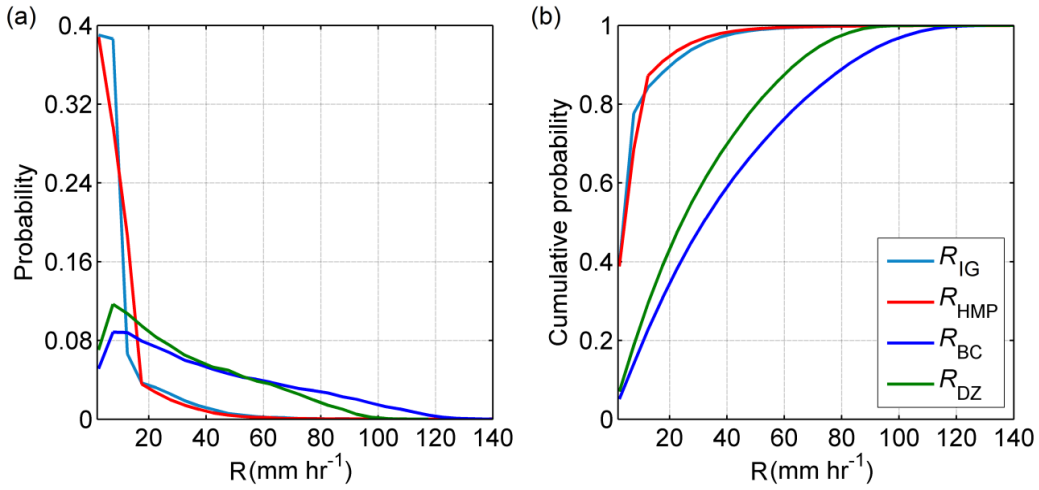

Figure 5.7. (a) Probability and (b) cumulative probability distribution of precipitation rates derived from different Z-R relations (see Table 2.4).

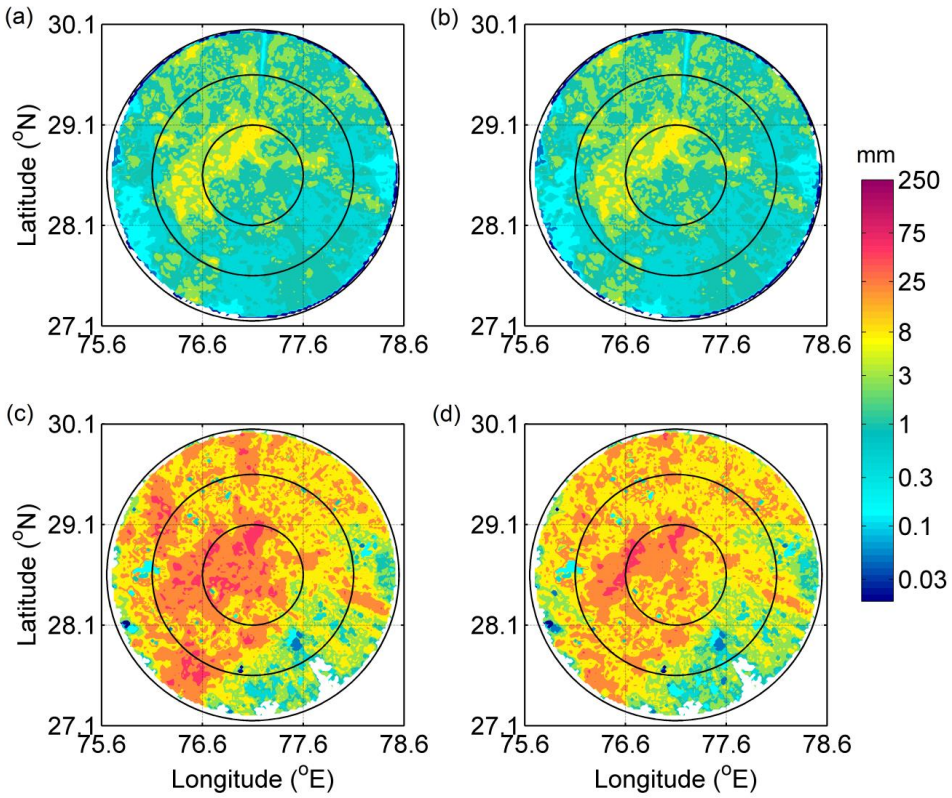

Figure 5.8. Horizontal structure of total accumulated precipitation (in mm) during 6, 12, 13, 14, 15 and 16 June derived using (a) R_{IG}, (b) R_{HMP}, (c) R_{BC} and (d) R_{DZ} (see Table 2.4 for functional forms).

mean square error for each pair of rainfall relations with rain gauge rain are shown in Table 5.1. Here, the normalized bias (NB) between the IMD rain gauge rainfall (R_{gauge}) and DWR derived rainfall (R_{DWR}) is calculated from the equation (Bringi *et al.* 2001):

$$NB = \frac{\left(\frac{1}{N}\right)\sum_{i=1}^{N}\left(\overline{R}_{DWR} - \overline{R}_{gauge}\right)}{\left(\frac{1}{N}\right)\sum_{i=1}^{N}\overline{R}_{gauge}} \quad . \tag{5.1}$$

The root mean square error (RMSE) is estimated from the equation,

$$RMSE = \sqrt[2]{\frac{\sum_{i=1}^{N}(R_{DWR} - R_{gauge})^2}{N}} \quad . \tag{5.2}$$

P_{acc} from Z_h have large normalized biases (NB's) and root mean square errors (RMSEs). On contrary, P_{acc} derived from K_{dp} are in better agreement with gauge rainfall

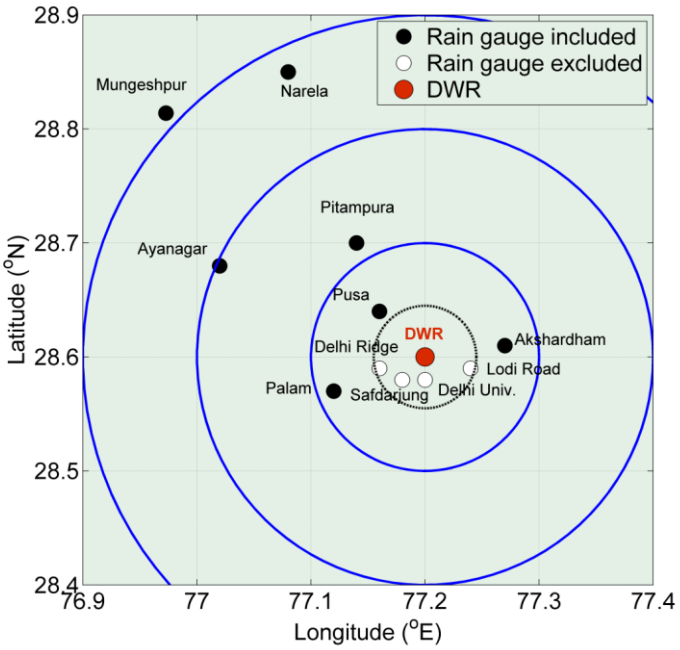

Figure 5.9. The distribution of IMD rain gauges around C-band polarimetric Doppler weather radar (28.58°N, 77.22°E). The rain gauges within the 5 km radius (in white filled-in circles) around DWR are excluded in the rainfall estimates. Following are the IMD rain gauge locations: (1) Pusa (77.16°E, 28.64°N), Akshardham (77.27°E, 28.61°N), Mungeshpur (76.97°E, 28.82°N) Narela (77.08°E, 28.85°N), Pitampura (77.15°E, 28.7°N), Aya Nagar (77.02°E, 28.68°N), Palam (77.12°E, 28.57°N), Lodi Road (77.24°E, 28.59°N), Safdarjung (77.23°E, 28.66°N), Delhi Ridge (77.18°E, 28.62°N), Delhi University (77.1°E, 28.7°N).

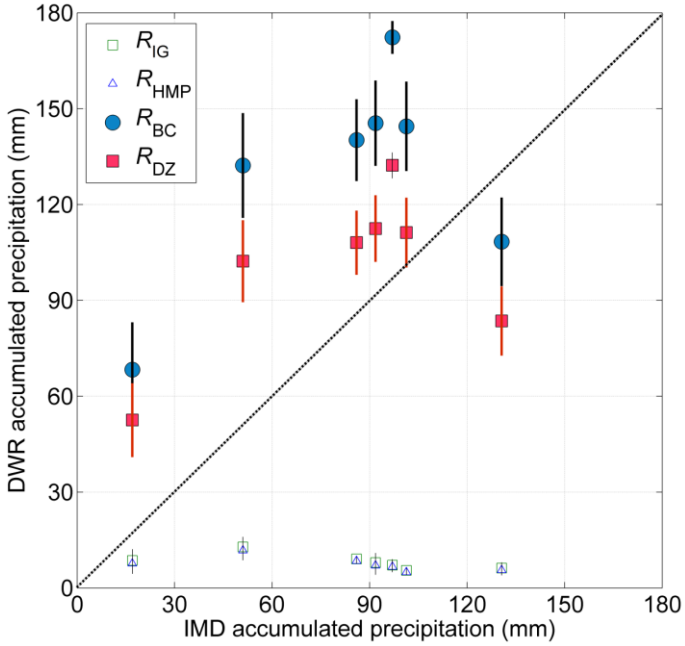

Figure 5.10. Comparison between DWR and Rain gauge accumulated precipitation. The vertical bar at each data point is the 1-standard deviation of rainfall accumulation at each DWR pixel around the rain gauge location.

accumulations. The least NB (0.22) and RMSE (~27 mm) are found for R-K_{dp} relation from Dovaik and Zrnic (1993) (Table 2.4 in Chapter 2 and Table 5.1). The maximum P_{acc} calculated from Z_h is less than 20 mm. It indicates that the rainfall estimates derived from the polarimetric variable K_{dp} are more realistic than that derived from Z_h. The Z-R relations are location as well as event specific (drop size distribution (DSD) is more fundamental). In the current study, the rainfall estimates from Z-R relations used may not be appropriate for cloud systems at Delhi. On the other side, K_{dp} is a function of phase shift in both horizontal and vertical polarized beams and its value is independent of DSD of hydrometeors and depend more on liquid water path seen by each beam (Bringi and Chandrasekar 2001). Although *R*-K_{dp} relations involve several assumptions (e.g. on orientation distributions of falling drops, raindrop axis ratio; see Bringi and Chandrasekar 2001, 538 pp. and Dovaik and Zrnic 1993) which are related to the shape and geometry of the hydrometeors, they gave better estimates.

Table 5.1. Normalized bias and RMSE between rain gauge and DWR derived accumulated precipitations.

No.	Rain rate relation	Symbol	***RMSE (mm)***	***NB***
1.	Iguchi *et al*. 2000 $Z_h=aR^b$	R_{IG}	65.5	-0.98
2.	Hunter *et al.* 1996; MP 1948 $Z_h=aR^b$	R_{HMP}	65.9	-0.90
3.	Bringi and Chandrasekhar 2001 $R(K_{dp})=a(K_{dp}/f)^b$	R_{BC}	45.8	0.59
4.	Doviak and Zrnic 1993 $R(K_{dp})=a(K_{dp}\lambda)^b$	R_{DZ}	27.6	0.22

5.4. Vertical profiles of cloud liquid water content

To further investigate the microphysical nature of the clouds, the vertical profiles of *M* for convective echoes are obtained. The *M* values derived from different relations (Table 2.5, Chapter 2) are shown in Figures. 5.11. *M* varied from less than 0.02 gm m^{-3} to nearly 4.8 gm m^{-3}. The large dynamic range of *M* shows natural variability during the lifetime of clouds. More importantly, both the magnitude of *M* and its variation in the vertical depend on the relation used for estimating *M*. M_{GC} (Table 2.6, Chapter 2) yields the lowest mean values of *M* of about 1 gm m^{-3} (Figure 5.11 a) while that based on M_{BC} and M_{DG} have mean about 2 gm m^{-3} throughout the altitude levels (starting from 1.5 km

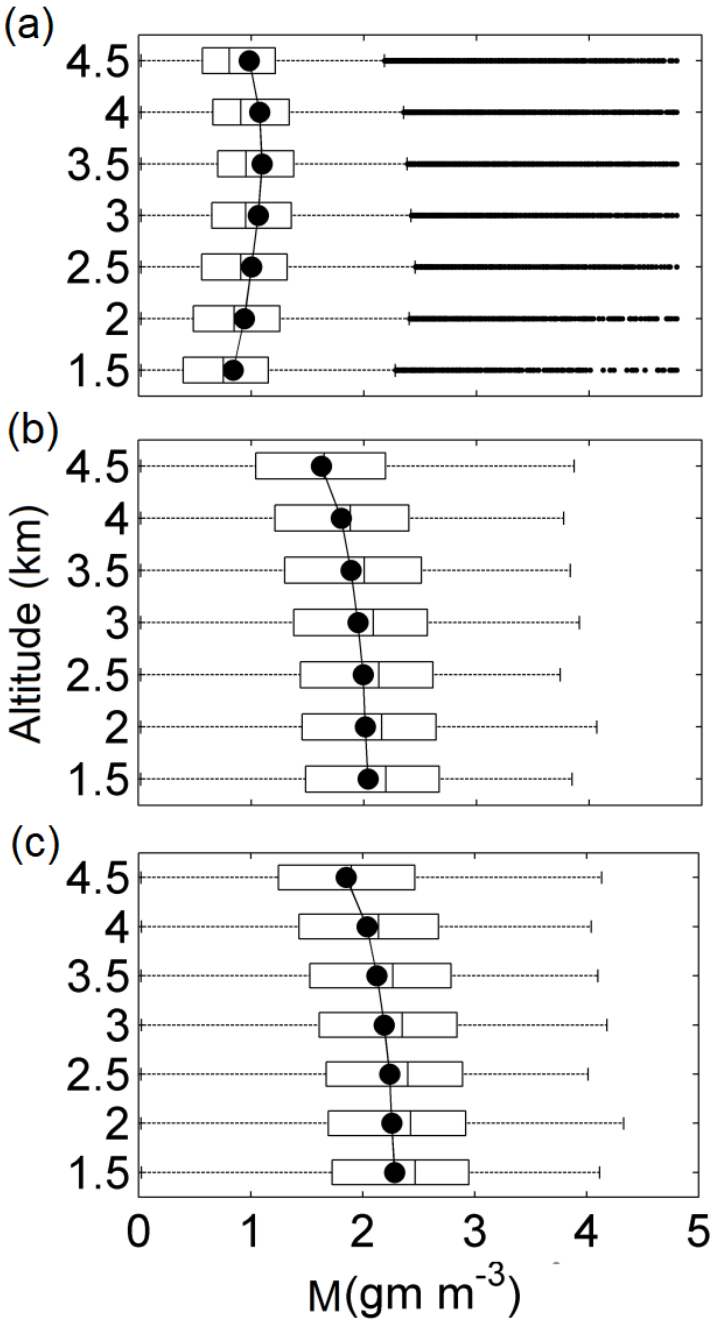

Figure 5.11. Cloud liquid water content (*M*) estimated using (a) M_{GC}, (b) M_{BC}, and (c) M_{DZ} (see Table 2.5 for functional forms). The filled circles are the average values of *M* at each altitude. Here, the horizontal bar within the box is the median value, and the lower and upper limits of *M* show 25% and 75% percentile of the data. Black dots beyond 75% percentile of *M* indicate the outliers in data.

till 4.5 km) (Figure 5.11 b and c; (Table 5.2). The maximum value of *M* is somewhat similar (~4.2) however the frequency of such higher *M* values is large for that derived from K_{dp} compare to that derived from Z_h. The peak in mean profile of *M* derived from Z_h is observed at 3.5 km while it is missing in that derived from K_{dp}. Small changes in

Table 5.2. Mean and maximum cloud liquid water content (M) derived from Z_h and K_{dp}.

No.	CLWC relation	Symbol	Mean (gm m^{-3})	Max (gm m^{-3})
1.	Greene and Clark 1972 $M(Z_h)=cZ_h^d$	M_{GC}	1	4.8
2.	Bringi and Chandrasekhar 2001 $M(K_{dp})=c(K_{dp}/f^*)^d$	M_{BC}	2.2	3.9
3.	Doviak and Zrnic 1993 $M(K_{dp})=c(K_{dp}\lambda^\#)^d$	M_{DZ}	2.4	4.2

*f is radar frequency =5.62 GHz for the Delhi C-band radar; #λ is radar beam wavelength= 5.33 μm

mean values of M at each altitude for M_{GC}, M_{BC} and M_{DZ} relations is noticed. Given the large differences in the values of M at each altitude, which one is likely to be correct? Answering this requires independent observations. Aircraft measurements made over Bareilly (which is situated in this region and not very far from Delhi) show mean M of 0.27 gm m^{-3} during the summer monsoon period (Morwal *et al.* 2012). Owing to safety considerations, aircraft avoids intense convective clouds, and aircraft samples are biased towards cumulus and cumulus congestus clouds. A higher M is expected in intense convective systems containing Cb clouds. Therefore, M estimates from (K_{dp}) relations are likely to be closer to reality. However, further studies are needed to confirm this.

5.5. Summary

This is the first study that reports the properties of convective clouds over the Indian region using data collected with a polarimetric DWR. Vertical structures of convective and stratiform echoes have been obtained, and storms and their characteristics are extracted. The vertical distribution of convective and stratiform echoes captured the signatures of heavy rainfall (below 4 km), melting band (~4 km) and anvil clouds at higher levels (~12 km). It is found that the convective clouds are very deep over the Delhi region, many of them extended beyond 16 km and a few even penetrated the altitude level of 18 km. The highest values of Z_h for both convective and stratiform echoes are observed around 4 km altitude, i.e., near the 0°C isotherm. The typical storm duration is an hour while few exceed 3½ hours. More than one-third of these individual storms propagated at speeds of 30 km hr^{-1} or more whereas majority of the storms move with speeds of 25 km hr^{-1} or less. The typical movement of the storms is in northwest and southeast directions. The temporal evolution of long-lived storm which had lifetime

of ~3½ hours shows that the average ETH of 30 dBZ more often remains above 10 km, indicates the presence of lightning and intense convective activities. It is found that the storms with higher vertical extent (>8 km) and large *ATI* contribute to the large precipitation amount. *ATI* and *RERV* are found to be strongly correlated. The precipitation rate (*R*) of storms is estimated between 5 and 34 mm hr^{-1}. During the 6 days period, the total accumulated precipitation (P_{acc}) derived from K_{dp} is found as large as 250 mm. Comparison of P_{acc} with rain guage rainfall P_{guage} accumulation shows that P_{acc} derived from polarimetric variable K_{dp} is closer to the P_{gauge} while P_{acc} derived from conventional Z-R relations are highly underestimated. The mean of cloud liquid water content derived from Z_h (~1 gm m^{-3}) is just half of that derived from K_{dp}. However their maximum bound (~4.2 gm m^{-3}) are somewhat comparable but their frequency at each vertical level differ largely. Those estimates based on relations involving polarimetric variable seem more realistic. These aspects need further investigation to narrow down the differences.

6

Conclusions

The present work reports the characteristics of convective clouds using spacebrone and ground based Doppler weather conventional and polarimetric radars. The mesoscale and storm scales of cloud systems are studied in detail.

First part of the work covers study of clouds using TRMM PR and CloudSat CPR data. It is concluded that the PR, essentially meant to measure characteristics of precipitating clouds, misses the anvil part of mesoscale convective systems, and the full spatial extent of MCSs is not covered. CPR captures the cloud spatial coverage better. However, its reflectivity values are much lower due to the strong attenuation suffered by the radar beam operating in W-band. CPR signal gets attenuated severely during rain, more so below 6 km height. Their measurements show very little overlap in their measured Z_e values. It is found that these radars have their respective limitations that need to be kept in mind while drawing conclusions on the cloud characteristics measured by PR and CPR.

In the second part, the life cycle of MCSs are discussed along with the properties of storms embedded in MCSs observed during the summer monsoon season which was reported for the first time using the DWR data over the Indian subcontinent. The convective echoes identification is done and their contribution in total area and precipitation are estimated. It is observed that the growth phase is characterized by a rapid increase in the number of storms. Importantly, within life span of an MCS, more than one life phases (e.g., mature or decay phase) may exist. MCS may contain a few too many storms whose area varies from less than 20 to more than 160 km^2 having average storm height typically varied between 6 to 10 km. During the initial growth phase of MCS, the convective precipitation fraction can be as high as 80% and then decreases with time, often not monotonically. The average convective precipitation fraction is 45% or below at all the five locations, higher at

Kolkata, Hyderabad and Delhi (~40%) and the least at Nagpur (13%). Arithmetic average generally underestimates the actual contribution of convective precipitation to the total precipitation from an MCS. For example, convective echoes contributed 55% of the total precipitation at Hyderabad, i.e., nearly 15% more than the average value. Patiala has the deepest 30 dBZ echoes with more than 15% of them extending above 10 km. 40 dBZ echo tops peak around 4 km (Delhi being an exception) and only a very small fraction of them are found above 10 km. MCSs clearly exhibit the regional differences via vertical profile of radar reflectivity. The average VPRR*s* at Hyderabad, Nagpur and Patiala show similarities in the mixed phase region while differences amplify below 5 km and above 10 km height. The peculiar microphysical and dynamical processes associated with each MCS govern VPRRs.

In the third part, findings from storm-scale are revealed and documented in detail. Using polarimetric DWR radar reflectivity data at Delhi (a land Indian region), the vertical distributions of convective and stratiform echoes captured the signatures of heavy rainfall (below 4 km), melting band (~5 km) and anvil clouds at higher levels (~12 km). It is found that the convective clouds are very deep over the Delhi region extended beyond 16 km. The highest values of Z_h for both convective and stratiform echoes are observed around 4 km altitude, i.e., near the melting level. The temporal evolution of long-lived storm of lifetime of ~3½ hours shows that the average ETH of 30 dBZ more often remains above 10 km, indicates the presence of lightning and intense convective activities. It is found that the storms with higher vertical extent (>8 km) and large *ATI* contribute to the large precipitation amount. *ATI* and *RERV* are found to be strongly correlated. The precipitation rate (*R*) of storms is estimated between 5 and 34 mm hr^{-1}. The total accumulated precipitation (P_{acc}) derived from K_{dp} is found as large as 250 mm during 6 June and 10-16 June, 2013. Comparison of P_{acc} with rain guage rainfall P_{guage} accumulation shows that P_{acc} derived from K_{dp} is closer to the P_{gauge} while P_{acc} derived from conventional Z-R relations are highly underestimated. The mean of cloud liquid water content (*M*) derived from Z_h (~1 gm m^{-3}) is just half of that derived from K_{dp}. However their maximum bound (~4.2 gm m^{-3}) are comparable but differ in their frequency at each vertical level. The *M* estimates based on relations derived using polarimetric variable seem more realistic than that derived using conventional Z_h. These aspects need further investigation to narrow down the differences.

In future, I would like to explore more DWR data from both single-polarized and polarimetric to understand the monsoonal clouds' structures over Indian region. Comparison of DWR data with K*a*- (35.5 GHz) and K*u*- (13.6 GHz) band radars onboard Global Precipitation Measurement (GPM) satellite will be another task which will reveal the limitations and sensitivities of sensors and will be helpful in validation of spaceborne reflectivity products using ground based platform. One of the prominent result from my thesis suggests that the rain estimates derived from polarimetric radars and rain gauges are nearer compare to that derived from single-polarized radars hence there is urgent need to strengthen the DWR network by installing more polarimetric radars (or upgrade the previously deployed radars) at various Indian land and oceanic locations. If the whole Indian region is covered by these polarimetric radars then it will be possible to get full tile of quality rainfall data over India which will be much more reliable than rainfall from space-borne sensors (e.g., TRMM PR, GPM PRs etc.) and will be more homogenous compare to rainfall ground networks (e.g., rain gauge, disdrometer etc.). Comparing it with model rainfall estimates will be another important step to improve our modelling outcomes over Indian region which will help to understand the monsoonal clouds' characteristics. In fact, it will further benefit to improve the cloud and convective parameterization in weather and climate models specifically over Indian region which are still inadequately applied. Teaching a full time course on radar meteorology will be my one of the important priorities. In upcoming years, more research units should come in existence which will be fully dedicated to radar meteorology where one may get expertise in this prestigious field of meteorology which is least known till date in India.

References

Abhilas, S., and Coauthors, 2007: Assimilation of Doppler weather radar observations in a mesoscale model for the prediction of intense rainfall events associated with mesoscale convective systems using 3DVAR. *J. Earth Syst. Sci*. **116**, 275-304.

Adeyewa, Z. D., and K. Nakamura, 2003: Validation of TRMM radar rainfall data over major climatic regions in Africa. *J. Appl. Meteor.* **42,** 331-347.

Albrecht, B. A., and Coauthors, 1995: The Atlantic stratocumulus transition experiment-ASTEX. *Bull. Amer. Meteor. Soc.* **76**, 889-904.

Alcala, C. M., and A. E. Dessler, 2002: Observations of deep convection in the tropics using the Tropical Rainfall Measuring Mission (TRMM) precipitation radar. *J. Geophys. Res.* **107**(D24), 4792, doi:10.1029/2002JD002457.

Arakawa, A., and W. H. Schubert, 1974: Interaction of a cumulus cloud ensemble with the large-scale environment, Part I. *J. Atmos. Sci*. **31**, 674-701.

Atlas, D., and Coauthors, 1999: Systematic variation of drop size and radar-rainfall relations, *J. Geophys. Res*. **104**(D6), 6155-6169.

Barker, H. W., and Coauthors, 2008: A comparison between CloudSat and aircraft data for a multilayer, mixed phase cloud system during the Canadian CloudSat-CALIPSO Validation Project. *J. Geophys. Res.* **113,** D00A16, doi: 10.1029/2008JD009971.

Behrangi, A., and Coauthors, 2012: On the quantification of oceanic rainfall using spaceborne sensors. *J. Geophys. Res.* **117**, D20105, doi:10.1029/2012JD017979.

Bhat, G. S., and S. Kumar, 2015: Vertical structure of cumulonimbus towers and intense convective clouds over the South Asian region during the summer monsoon season. *J. Geophys. Res. Atmos.* **120**, 1710-1722.

Bhat, G. S., and R. Narasimha, 2007: Indian summer monsoon experiments, *Curr. Sci*. **93**, 153-164.

Biggerstaff, M. I., and S. A. Listemaa 2000: An improved scheme for convective/stratiform echo classification using radar reflectivity. *J. Appl. Meteor.* **39**, 2129-2150.

Booker, H. G., 1946 Elements of radio Meteorology: how weather and climate cause unorthodox radar vision beyond the geometrical horizon. *Electrical Engineers-Part I.* **93**, 69-78.

Boos, W. R., and Z. Kuang, 2010: Dominant control of the South Asian monsoon by orographic insulation versus plateau heating, *Nature*. **463**, 218-222.

Braun, S. A., and R. A. Houze, 1994: The transition zone and secondary maximum of radar reflectivity behind a midlatitude squall line: Results retrieved from Doppler-radar data. *J. Atmos. Sci.* **51**, 2733-2755.

Bringi, V. N., and V. Chandrasekar, 2001: Polarimetric Doppler Weather Radar Principles and Applications, 2nd ed., *Cambridge Univ. Press*, New York, pp. 390, Ch.8, 537-545.

Bringi, V. N., T. D. Keenan and V. Chandrasekar, 2001: Correcting C-band radar reflectivity and differential reflectivity data for rain attenuation: A self-consistent method with constraints. *IEEE Trans. Geosci. Remote Sens*. **39**, 1906-1915.

Bringi, V. N., and Coauthors, 2001: An areal rainfall estimator using differential propagation phase: Evaluation using a C-band radar and a dense gauge network in the tropics. *J. Atmos. Oceanic Tech.* **18**, 1810-1818.

Bringi, V. N., and Coauthors, 2003: Raindrop size distribution in different climatic regimes from disdrometer and dual-polarized radar analysis. *J. Atmos. Sci*. **60**, 354-365.

Carty, H. M., and K-S. Kuo, 2008: A report: 2D-CloudSat-TRMM product description version 1.0; CloudSat Project, A NASA Earth system pathfinder mission.

Casey, S. P. F., A. E. Dessler and C. Schumacher, 2007: Frequency of tropical precipitating clouds as observed by the tropical rainfall measuring mission precipitation radar and ICESat/Geoscience laser altimeter system. *J. Geophys. Res.* **112,** D14215, doi: 10.1029/2007JD008468.

Casey, S. P. F., E. J. Fetzer and B. H. Kahn, 2012: Revised identification of tropical oceanic cumulus congestus as viewed by CloudSat. *Atmos. Chem. Phys.* **12,** 1587-1595.

Cetrone, J., and R. A. Houze, 2006: Characteristics of tropical convection over the ocean near Kwajalein. *Mon. Wea. Rev*. **134**, 834-853.

Cetrone, J., and R. A. Houze, 2009: Anvil clouds of tropical mesoscale convective systems in monsoon regions. *Quart. J. Roy. Meteor. Soc.* **135**, 305-317.

Chang, C. P., 1970: Westward propagating cloud patterns in the tropical Pacific as seen from time composite satellite photographs. *J. Atmos. Sci*. **27**, 133-138.

Charney, J. G., 1969: The intertropical convergence zone and the Hadley circulation of the atmosphere. *Proc. WMO/IUGG Symposium on Numerical Weather Prediction*, Tokyo, Japan, pp. III-73-79.

Chatterjee, P., U. K. De and D. Pradhan, 2015: Simulation of severe local storm by mesoscale model MM5 and validation using data from different platforms. *Int. J. Atmos. Sci*. 2015, Article ID 198704, doi:10.1155/2015/198704.

Chen, G. S., G. Liu and J. E. Kutzbach, 2014: Reexamining the barrier effect of the Tibetan Plateau on the South Asian summer monsoon, *Clim. Past*, **10**, 1269-1275.

Churchill, D. D., and R. A. Houze, 1984: Mesoscale updraft magnitude and cloud-ice content deduced from the ice budget of the stratiform region of a tropical cloud cluster. *J. Atmos. Sci.* **41**, 1717-1725.

Cifelli, R., and S. A. Rutledge, 1998: Vertical motion, diabatic heating, and rainfall characteristics in North Australia convective systems. *Quart. J. Roy. Meteor. Soc.* **124,** 1133-1162.

CIMO, 2008: CIMO *guide to Meteorogical instruments and methods of observation, secretariat of the WMO. Part II Observing methods. WMO No. 8 ed. 2008.* II.9-6, II.9-12 pp.

CTCZ, 2009: Continental tropical convergence zone (CTCZ) programme science plan. [Available online at http://odis.incois.gov.in/images/ctczimages/docs/science_plan. pdf.].

Das, S., R. Ashrit, and M. W. Moncrieff, 2006: Simulation of a Himalayan cloudburst event. *J. Earth Syst. Sci.* **115(3)**. 299-313.

Diner, D. J., and Coauthors, 1998: Multi-angle Imaging SpectroRadiometer (MISR) instrument description and experiment overview. *IEEE Trans. Geosci. Remote Sens.* **36,** 1072-1087.

Ding, Y., and Coauthors, 2006: South China Sea Monsoon Experiment (SCSMEX) and the East Asian monsoon. *J. Meteor. Res.* **20(2)**, 159-190.

Dixon, M., EOL/RAL, cited 2014: Radx C++ software package for radial radar data. [Available online at htttp://www.ral.ucar.edu/projects/titan/docs/radial_formats /radx.html.].

Dixon, M., and G. Wiener, 1993: TITAN: Thunderstorm Identification, Tracking, Analysis, and Nowcasting-A radar-based m*eth*odology. *J. Atmos. Oceanic Tech*. **10**, 785-797.

Donaldson, R. J., 1970: Vortex signature recognition by a Doppler radar. *J. Appl. Meteor*. **9**, 661-670.

Doneaud, A. A., and Coauthors, 1981: Simple method for estimating convective rain volume over an area. *Water Resour. Res*. **17**, 1676-1682.

Doneaud, A. A., and Coauthors, 1984: The area-time integral as an indicator for convective rain volumes. *J. Clim Appl. Meteor.* **23**, 555-561.

Doviak, R. K., and S. Zrnic, 1993: Doppler radar and weather observations, 2nd ed., *Academic Press*, San Diego, CA, pp. 562.

Fabry, F., and I. Zawadzki, 1995: Long-term radar observations of the melting layer of precipitation and their interpretation. *J. Atmos. Sci*. **52**, 838-851.

Fabry, F., 2015: Radar Meteorology: principle and practice. *Cambridge university press*, Cambridge. pp. 55.

Franchito, S. H., and Coauthors, 2009: Validation of TRMM precipitation radar monthly rainfall estimates over Brazil. *J. Geophys. Res.* **114**, D02105, doi: 10.1029/2007JD0 09580.

Fujita, T. T., 1981: Tornadoes and downbursts in the context of generalized planetary scales. *J. Atmos. Sci*. **38**, 1511-1534.

Gadgil, S., 2003: The Indian monsoon and its variability. *Annu. Rev. Earth Planet. Sci*. **31**, 429-467.

Gamache, J. F., and R. A. Houze, 1982: Mesoscale air motions associated with a tropical squall line. *Mon. Wea. Rev.* **110,** 118-135.

Gambheer, A. V., and G. S. Bhat, 2000: Life cycle characteristics of deep cloud systems over the Indian region using INSAT-1B pixel data. *Mon. Wea. Rev.* **128**, 4071-4083.

Gambheer, A. V., and G. S. Bhat, 2001: Diurnal variation of deep cloud systems over the Indian region using INSAT-1B pixel data. *Meteor. Atmos. Phys.* 78, 215-225.

Gilgen, H. J., and A. Ohmura, 1999: The global energy balance archive. *Bull. Amer. Meteor. Soc.* **80**, 831-850.

Gill, A. E., 1980: Some simple solutions for heat-induced tropical circulation. *Quart. J. Roy. Meteor. Soc*. **106**, 447-462.

Gorgucci, E., and V. Chandrasekar, 2005: Evaluation of Attenuation Correction Methodology for Dual-Polarization Radars: Application to X-Band Systems. *J. Atmos. Ocean. Tech*. **22**, 1195-1206.

Gourley, J. J., and Coauthors, 2010: Intercomparison of rainfall estimates from radar, satellite, gauge, and combinations for a season of record rainfall. *J. Appl. Meteor. Clim.* **49,** 437-452.

Greene, D. R., and R. A. Clark 1972: Vertically integrated liquid water-a new analysis tool. *Mon. Wea. Rev*. **100**, 548-552.

Gunn, R., and G. D. Kinzer, 1949: The terminal velocity of fall for water droplets in stagnant air. *J. Meteor*. **6**, 243-248.

Guy, N., S. A. Rutledge, and R. Cifelli, 2011: Radar characteristics of continental, coastal, and maritime convection observed during AMMA/NAMMA. *Quart. J. Roy. Meteor. Soc*. **137,** 1241-1256.

Haynes, J. M., and G. L. Stephens, 2007: Tropical oceanic cloudiness and the incidence of precipitation early results from CloudSat. *Geophys. Res. Lett.* **34,** L09811, doi: 10.1029/2007GL029335.

Hence, D. A., and R. A. Houze 2011: Vertical structure of hurricane eyewalls as seen by the TRMM Precipitation Radar. *J. Atmos. Sci.* **68**, 1637-1652.

Heymsfield, G. M., and S. Schotz, 1985: Structure and evolution of a severe squall line over Oklahoma. *Mon. Wea. Rev.* **113**, 1563-1589.

Heymsfield, G. M., and Coauthors, 2010: Characteristics of deep tropical and subtropical convection from nadir-viewing high-altitude airborne Doppler radar. *J. Atmos. Sci*. **67**, 285-308.

Hirose, M., and K. Nakamura 2002: Spatial and seasonal variation of rain profiles over Asia observed by spaceborne precipitation radar. *J. Clim.* **15**, 3443-3458.

Holton, J. R., 2004: An introduction to dynamic Meteorology, Chapter 11; 4th Edition, *Academic Press*, New York, pp. 531.

Houze, R. A., 1973: A climatological study of vertical transports by cumulus-scale convection. *J. Atmos. Sci*. **30**, 1112-1123.

Houze, R. A., 1977: Structure and dynamics of a tropical squall-line system. *Mon. Wea. Rev*. **105**, 1540-1567.

Houze, R. A., and C-P. Cheng, 1977: Radar characteristics of tropical convection observed during GATE: mean properties and trends over the summer season. *Mon. Wea. Rev.* **105**, 964-980.

Houze, R. A., 1981: Structures of atmospheric precipitation systems-A global survey. *Radio Science.* **16**, 671-689.

Houze, R. A., and A. K. Betts, 1981: Convection in GATE. *Rev. Geophys. Space Phys.* **19**, 541-576.

Houze, R. A., 1982: Cloud clusters and large-scale vertical motions in the tropics. *J. Meteor. Soc. Jpn.* **60**, 396-410.

Houze, R. A., and D. D. Churchill, 1987: Mesoscale organization and cloud microphysics in a Bay of Bengal depression. *J. Atmos. Sci.* **44**, 1845-1867.

Houze, R. A., 1989: Observed structure of mesoscale convective systems and implications for large-scale heating. *Quart. J. Roy. Meteor. Soc*. **115**, 425-461.

Houze, R. A., 2004: Mesoscale convective systems. *Rev. Geophys*. **42**, RG4003, doi:10.1029/ 2004RG000150.

Houze, R, A., D. C. Wilton, B. F. Smull, 2007: Monsoon convection in the Himalayan region as seen by the TRMM Precipitation Radar. *Quart. J. Roy. Meteor. Soc*. **133**, 1389-1411.

Houze, R. A., 2014: *Cloud Dynamics*. 2nd ed., International geophysical series, Academic press. 83, 142-143, 152 pp.

Hudak, D., P. Rodriguez, and N. Donaldson 2008: Validation of the CloudSat precipitation occurrence algorithm using the Canadian C-band radar network. *J. Geophys. Res.* **113**, D00A07, doi: 10.1029/2008JD009992.

Hunt, K. M. R., A. G. Turner and D. E. Parker, 2016: The spatiotemporal structure of precipitation in Indian monsoon depressions. *Quart. J. Roy. Meteor. Soc*. **142**, 3195-3210.

Hunter, S. M., 1996: WSR-88D radar rainfall estimation: capabilities, limitations and potential improvements. *National Weather Digest.* **20**, 26-38. [Available online at http://www.nw- as.org /digest/papers/1996/Vol20No4/Pg26-Hunter.pdf.].

Iguchi, T., and R. Meneghini, 1994: Intercomparison of single-frequency methods for retrieving a vertical rain profile from airborne or spaceborne radar data. *J. Atmos. Oceanic Tech.* **11**, 1507-1516.

Iguchi T., and Coauthors, 2000: Rain-profiling algorithm for the TRMM precipitation radar. *J. Appl. Meteor*. **39**, 2038-2052.

Iguchi, T., and Coauthors, 2009: Uncertainties in the rain profiling algorithm for the TRMM precipitation radar. *J. Meteor. Soc. Jpn.* **87A,** 1-30.

IMD Report, 2013: Monsoon 2013: a report, *Met. Monograph: Synoptic Meteorology*, No.: ESSO/IMD/SYNOPTIC MET/01-2014/15.

Jirak, I. L., and Coauthors, 2003: Satellite and radar survey of mesoscale convective system development. *Mon. Wea. Rev*. **131**, 2428-2449.

Johnson, R. H., and R. A. Houze, 1987: *Precipitating cloud systems of the Asian monsoon*. Monsoon Meteorology. C. P. Chang and T. N. Krishnamurti eds. *Oxford University Press*, *New York*. 298-353.

Johnson, J. T., and Coauthors, 1997: The storm cell identification and tracking algorithm: An enhanced WSR-88D algorithm. *Wea. and Forc*. **13**, 263-276.

Jorgensen, D. P., and M. A. LeMone, and S. B. Trier, 1997: Structure and evolution of the 22 February 1993 TOGA COARE squall line: Aircraft observations of structure, circulation, and near-surface energy fluxes. *J. Atmos. Sci*. **54**, 1961-1985.

Kiehl, J. T., and K. E. Trenberth, 1997: Earth's Annual Global Mean Energy Budget. *Bull. Amer. Meteor. Soc.* **78**, 197-208.

Kelly, P., and B. Mapes, 2011: Zonal mean wind, the Indian monsoon, and July drying in the western Atlantic subtropics. *J. Geophys. Res*. **116**, D00Q07, doi:10.1029/2010 JD015405.

Kerr, R. A., 2009: Clouds appear to be big, bad player in global warming. *Science*. **325**, 376.

Kim, S. W., And Coauthors, 2011: Intercomparisons of cloud-top and cloud-base heights from ground-based Lidar, CloudSat and CALIPSO measurements. *Int. J. Remote Sens.* **32,** 1179-1197.

King, M. D., and Coauthors, 1992: Remote sensing of cloud, Aerosol, and water vapor properties from the moderate resolution imaging spectrometer (MODIS). *IEEE Trans. Geosci. Remote Sens.* **30,** 2-27.

Kollias, P., and Coauthors, 2007: Millimeter-wavelength radars: New frontier in atmospheric cloud and precipitation research. *Bull. Amer. Meteor. Soc.* **88,** 1608-1624.

Krishnamurti, T. N., 1985: Summer monsoon experiment-a review. *Mon. Wea. Rev.* **113**, 590-26.

Kumar, S., and G. S. Bhat, 2016: Vertical profiles of radar reflectivity factor in intense convective clouds in the tropics. *J. Appl. Meteor. Clim*. **55**, 1277-1286.

Kummerow, C., and Coauthors, 1998: The tropical rainfall measuring mission (TRMM) sensor package. *J. Atmos. Ocean. Tech.* **15,** 809-817.

Kummerow, C., and Coauthors, 2000: The status of the Tropical Rainfall Measuring Mission (TRMM) after two years in orbit. *J. Appl. Meteor.* **39,** 1965-1982.

Laing, A. G., and J. M. Fritsch, 1997: The global population of mesoscale convective complexes. *Quart. J. Roy. Meteor. Soc*. **123**, 389-405.

Lang, T. J., and Coauthors, 2007: Radar-observed characteristics of precipitating systems during NAME 2004. *J. Clim.* **20**, 1713-1733.

Lau, N. C., and M. W. Crane, 1995: A satellite view of the synoptic-scale organization of cloud properties in midlatitude and tropical circulation systems. *Mon. Wea. Rev.* **123**, 1984-2006.

Lau J., and Coauthors, 2000: A report of the field operations and early results of the South China Sea Monsoon Experiment (SCSMEX). *Bull. Amer. Meteor. Soc*. **81**, 1261-1270.

Laurent, H., and Coauthors, 2002: Characteristics of Amazonian mesoscale convective systems observed from satellite and radar during the WETAMC/LBA experiment. *J. Geophys. Res*. **107**, 8054, doi:10.1029/2001JD000337.

LeMone, M. A., and Coauthors, 1995: Boundary layer recovery in the stratiform region of mesoscale convective system in TOGA COARE. *Proceedings of the 21st conference on hurricane and tropical Meteorology*, Miami. American Meteorogical Society, Boston, USA. 91-93.

Li W., and C. Schumacher, 2011: Thick anvils as viewed by the TRMM precipitation radar. *J. Clim*. **24,** 1718-1735.

Li, J., and Coauthors, 2012: The characteristics of mesoscale convective systems (MCSs) over East Asia in warm seasons, *Atmos. Ocean Sci. Lett.* **5(2)**, 102-107.

Lin, Y-L., 2007: *Mesoscale Dynamics*. Cambridge University Press, Chapter 1.

Li, Y., and Coauthors, 2008: Cloud-resolving modeling of deep convection during KWAJEX. Part I: Comparison to TRMM satellite and ground-based radar observations. *Mon. Wea. Rev*. **136**, 2699-2712.

Liu, C., and Coauthors, 2008: A cloud and precipitation feature database from nine years of TRMM observations. *J. Appl. Meteor. Clim.* **47**, 2712-2728, doi: 10.1175/2008 JAMC1890.1.

Liu, C., and E. J. Zipser, 2008: Diurnal cycles of precipitation, clouds, and lightning in the tropics from 9 years of TRMM observations. *Geophys. Res. Lett.* **35,** L04819, doi: 10.1029/2007GL032437.

Liu, C., and E. J. Zipser, 2013: Why does radar reflectivity tend to increase downward toward the ocean surface, but decrease downward toward the land surface?. *J. Geophys. Res.* **118**, 135-148.

Liu, C., and Coauthors, 2012: Relationships between lightning flash rates and radar reflectivity vertical structures in thunderstorms over the tropics and subtropics. *J. Geophys. Res*. **117**, D06212, doi:10.1029/2011JD0 17123.

Ludlam, F. H., 1980: *Clouds and Storms: The behavior and effect of water in the atmosphere*, Pennsylvania State University Press. University Park. 405 pp.

Luo, Z., and G, Y Liu, and G. L. Stephens, 2008: CloudSat adding new insight into tropical penetrating convection. *Geophys. Res. Lett.* **35,** L19819, doi: 10.1029/2008GL035330.

Mapes, B. E., and R. A. Houze, 1992: An integrated view of the 1987 Australian monsoon and its mesoscale convective systems. I: Horizontal structure. *Quart. J. Roy. Meteor. Soc*. **118**, 927-963.

Mapes, B. E., P. Liu, and N. Buenning, 2005: Indian monsoon onset and Americas midsummer drought: out-of-equilibrium responses to smooth seasonal forcing. *J. Clim.* **18**, 1109-1115.

Marshall JS, Langille RC and Palmer WM. 1947. Measurement of rainfall by Radar. *J. Meteor*. **4**, 186-192.

Masunga, H., and C. D. Kummerow 2006: Observations of tropical precipitating clouds ranging from shallow to deep convective systems. *Geophys. Res. Lett.* **33,** L16805, doi: 10.1029/2006GL026547.

Mathon, V., H. Laurent, and T. Lebel, 2002: Mesoscale convective system rainfall in the Sahel. *J. Appl. Meteor.* **41**, 1081-1092.

Matrosov, S.Y., 2014: Intercomparisons of CloudSat and ground-based radar retrievals of rain rate over land. *J. Appl. Meteor. Clim.* **53**, 2360-2370.

Matrosov, S.Y., 2015: The use of CloudSat data to evaluate retrievals of total ice content in precipitating cloud systems from ground-based operational radar measurements. *J. Appl. Meteor. Clim.* **54**, 1663–1674.

Medina, S., and Coauthors, 2010: Summer monsoon convection in the Himalayan region: Terrain and land cover effects. *Quart. J. Roy. Meteor. Soc.* **136**, 593-616.

Morel, C., and S. Senesi, 2002: A climatology of mesoscale convective systems over Europe using satellite infrared imagery. I: Methodology. *Quart. J. Roy. Meteor. Soc*. **128**, 1953-1971.

Morwal, S. B., and Coauthors, 2012: Cloud microphysical properties over Indian monsoon regions during CAIPEEX-2009. *J. Atmos. Solar-Terrestrial Phy*. **81-82**, 76-85.

Mukhopadhyay, P., and M. Mahakur, H. A. K. Singh, 2009: The interaction of large scale and mesoscale environment leading to formation of intense thunderstorms over Kolkata Part I: Doppler radar and satellite observations. *J. Earth Syst. Sci*. **118**, 441-466.

Nair, S., G. Srinivasan and R. Nemani, 2009: Evaluation of multi-satellite TRMM derived rainfall estimates over a western state of India. *J. Meteor. Soc. Jpn.* **87,** 927-939.

Nakazawa, T., 1988: Tropical super clusters within intraseasonal variations over the Western Pacific. *J. Meteor. Soc. Jpn.* **66**, 823-829.

Nesbitt, S. W., E. J. Zipser, and D. J. Cecil, 2000: A census of precipitation features in the tropics using TRMM: Radar, ice scattering, and lightning observations. *J. Clim*. **13,** 4087- 4106.

Nesbitt, S. W., R, Cifelli S. A. Rutledge, 2006: Storm morphology and rainfall characteristics of TRMM precipitation features. *Mon. Wea. Rev*. **134**, 2702-2721.

Nicholson, S. E., and Coauthors, 2003a: Validation of TRMM and other rainfall estimates with a high-density gauge dataset for West Africa. Part I Validation of GPCC rainfall product and pre-TRMM satellite and blended products. *J. Appl. Meteor*. **42,** 1337-1354.

Nicholson, S. E., and Coauthors, 2003b: Validation of TRMM and other rainfall estimates with a high-density gauge dataset for west Africa. Part II Validation of TRMM rainfall products. *J. Appl. Meteor.* **42,** 1355-1368.

Novo, S., and D. Martinez, and O. Puentes, 2014: Tracking, analysis, and nowcasting of Cuban convective cells as seen by radar. *Met. Apps*. **21**, 585-595.

Orlanski, I., 1975: A rational subdivision of scales for atmospheric processes. *Bull. Amer. Meteor. Soc.* **56**, 529-530.

Pai, D. S., and S. C. Bhan, 2013: Monsoon 2013 *IMD Met Monograph No.*: ESSO/IMD /SYNOPTIC MET/01-2014/15.

Park, H., and Coauthors, 2009: The hydrometeor classification algorithm for the polarimetric WSR-88D: Description and application to an MCS. *Wea. Forc.* **24**, 730-748.

Pessi, A. T. and S. Businger, 2009: Relationships among lightning, precipitation, and hydrometeor characteristics over the North Pacific ocean. *J. Appl. Meteor. Clim.* **48**, 833-848.

Philips, P. J., and A. E. Gill, 1987: An analytic model of the heat-induced tropical circulation in the presence of a mean wind. *Quart. J. Roy. Meteor. Soc*. **113**, 213-236.

Pokherel, S., and D. R. Sikka, 2013: Variability of the TRMM-PR total and convective and stratiform rain fractions over the Indian region during the summer monsoon. *Clim. Dyn*. **41**, 21-44.

Potts, R. J., andT. D. keenan, and P. T. May, 2000: Radar characteristics of storms in the Sydney area. *Mon. Wea. Rev.* **128,** 3308-3319.

Punkka, A. J., and M. Bister, 2005: Occurrence of summertime convective precipitation and mesoscale convective systems in Finland during 2000-01. *Mon. Wea. Rev.* **133**, 362-373.

Rajeevan, M., S. Gadgil, and S Bhate, 2010: Active and break spells of the Indian summer monsoon. *J. Earth Syst. Sci*. **119**, 229-247.

Rajeevan, M., and Coauthors, 2012: A study of vertical cloud structure of the Indian summer monsoon using CloudSat data. *Clim. Dyn.* **40**, 637-650.

Rao, Y. P., 1976: Southwest Monsoon. *Meteor. Monogr*. No. 1. India Meteor. Dept., New Delhi. 366 pp.

Rao, T. N., and Coauthors, 2001: Classification of tropical precipitating systems and associated *Z-R* relationships. *J. Geophys. Res*. **106**, 17699-17711.

Rao, Y. V. R., and Coauthors, 2007: An experiment using the high resolution eta and WRF models to forecast heavy precipitation over India; *Pure Appl. Geophys*. **164(8-9)**, 1593-1615.

Rigo, T., and M-C. Llasat, 2007: Analysis of mesoscale convective systems in Catalonia using Meteorogical radar for the period 1996-2000. *Atmos. Res*. **83**, 458-472.

Roca, R., and V. Ramanathan, 2000: Scale dependence of monsoonal convective systems over the Indian Ocean. *J. Clim.* **13**, 1286-1298.

Romatschke, U., S. Medina and R. A. Houze, 2010: Regional, seasonal, and diurnal variations of extreme convection in the south Asian region. *J. Clim*. **23**, 419-439.

Romatschke, U., and R. A. Houze, 2011: Characteristics of precipitating convective systems in the South Asian monsoon. *J. HydroMeteor.* **12**, 3-26.

Rosenfeld, D., E. Amitai, and D. B. Wolff, 1995: Classification of rain regimes by the three dimensional properties of reflectivity fields. *J. Appl. Meteor.* **34**, 198-211.

Rosenfeld, D., and C. W. Ulbrich, 2003: Cloud microphysical properties, processes, and rainfall estimation opportunities. *Meteor. Monogr.* **30**, 237-237.

Rossow, W. B., and E. N. Duenas, 2004: The International Satellite Cloud Climatology Project (ISCCP) web site: An online resource for research. *Bull. Amer. Meteor. Soc.* **85**, 167-172.

Rossow, WE. B., and Y-C. Zhang, 1995: Calculation of surface and top-of-atmosphere radiative fluxes from physical quantities based on ISCCP datasets. Part II: validation and first results. *J. Geophys. Res.* **100**, 1167-1197.

Rowe, A. K., S. A. Rutledge and T. J. Lang, 2011: Investigation of microphysical processes occurring in isolated convection during NAME. *Mon. Wea. Rev.* **139**, 424 443.

Rowe, A. K., S. A. Rutledge and T. J. Lang, 2012: Investigation of microphysical processes occurring in organized convection during NAME. *Mon. Wea. Rev.* **140**, 2168-2187.

Ryzhkov, A. V., and D. S. Zrnic, 2007: Depolarization in ice crystals and its effect on radar polarimetric measurements. *J. Atmos. Oceanic Tech.* **24**, 1256-1267.

Rowe, A. K., and R. A. Houze, 2014: Microphysical characteristics of MJO convection over the Indian Ocean during DYNAMO. *J. Geophys. Res. Atmos.* **119**, 2543-2554.

Sahany, S., V. Venugopal and R. S. Nanjundiah, 2010: Diurnal-scale signatures of monsoon rainfall over the Indian region from TRMM satellite observations. *J. Geophys. Res*. **115,** D02103, doi:10.1029/2009JD012644.

Saikranthi, K., and Coauthors, 2014: Morphology of the vertical structure of precipitation over India and adjoining oceans based on long-term measurements of TRMM PR. *J. Geophys. Res. Atmos*. **119**, 8433-8449.

Schmetz, J., and Coauthors, 2002: An introduction to Meteosat second generation (MSG). *Bull. Amer. Meteor. Soc.* **83**, 977-992.

Schumacher, C., and R. A. Houze, 2000: Comparison of radar data from the TRMM satellite and Kwajalein oceanic validation site. *J. Appl. Meteor.* **39,** 2151-2164.

Schumacher, C., and R. A. Houze, 2003: Stratiform rain in the tropics as seen by the TRMM precipitation radar. *J. Clim*. **16**, 1739-1756.

Schumacher, C., and R. A. Houze, 2006: Stratiform precipitation production over sub-Saharan Africa and the tropical East Atlantic as observed by TRMM. *Quart. J. Roy. Meteor. Soc.* **132,** 2235-2255.

Shah, S., R. Notapietro, and M. Branca, 2015: Storm identification, tracking and forecasting using high-resolution images of short-range X-band radar. *Atmosphere*. **6**, 579-606.

Sikka, D. R., and S. Gadgil, 1980: On the maximum cloud zone and the ITCZ over Indian, longitudes during the Southwest monsoon. *Mon. Wea. Rev.* **108**, 1840-1853.

Sikka, D. R., 1997: Desert clim and its dynamics. *Curr. Sci.*, **72**, 35-46.

Smull, B. F., and R. A. Houze, 1987: Dual-Doppler radar analysis of a midlatitude squall line with a trailing region of stratiform rain. *J. Atmos. Sci.* **44**, 2128-2148.

Steiner, M., and R. A. Houze, 1993: Three-dimensional validation at TRMM ground truth sites: Some early results from Darwin, Australia. Preprints, *26th Conference on Radar Meteorology,* Norman, American Meteorogical Society, 417-420.

Steiner, M, R. A. Houze, and S. E. Yuter, 1995: Climatological characterization of three-dimensional storm structure from operational radar and rain gauge data. *J. Appl. Meteor.* **34**, 1978-2007.

Stephens, 1994: Remote sensing of the lower atmosphere: An introduction. Oxford University Press, UK, 523 pp.

Stephens, G. L., and Coauthors, 2002: The CloudSat mission and the A-TRAIN: A new dimension to space-based observations of clouds and precipitation. *Bull. Amer. Meteor. Soc.* **83,** 1771-1790.

Stephens, G. L., and Coauthors, 2008: CloudSat mission performance and early science after first year of operation. *J. Geophys. Res.* **113,** D00A18, doi: 10.1029/2008JD009982.

Stith, J. L., 1995: In situ measurements and observations of cumulonimbus mamma. *Mon. Wea. Rev.* **123**, 907-914.

Streten, N. A., and A. J. Troup, 1973: synoptic climatology of satellite observed cloud vortices over the Southern Hemisphere. *Quart. J. Roy. Meteor. Soc*. **99**, 787-788.

Takahashi, C., and Coauthors, 2008: Relationships among structures, development processes, and heating profiles for two mesoscale convective systems in inactive phase of a large-scale disturbance over Northern Australia during the Southern summer in 1998-1999. *J. Meteor. Soc. Jpn*. **86**, 81-117.

Testud, J., and Coauthors, 2000: The rain profiling algorithm applied to polarimetric weather radar. *J. Atmos. Ocean. Tech.* **17,** 332-356.

Trier, S. B., and Coauthors, 1996: Structure and evolution of the 22 February 1993 TOGA COARE squall line: Numerical simulations. *J. Atmos. Sci*. **53**, 2861-2886.

Toracinta, E. R., and Coauthors, 2002: Radar, passive microwave, and lightning characteristics of precipitating systems in the tropics, *Mon. Wea. Rev*. 130, 802-824.

Turner, 1986: Turbulent entrainment: The development of the entrainment assumption, and its application to geophysical flows. *J. Fluid Mech.* **173**, 431-471.

Tyagi, A. *et al.*, 2012: Monsoon Monograph, *India Meteorogical Department, New Delhi*. Vol. **2.**

Velasko, I., and J. M. Fritsch, 1987: Mesoscale convective complexes in the Americas. *J. Geophys. Res.* **92**(D8), 9591-9613.

Waliser, D. E. and C. Gautier, 1993: A Satellite-derived climatology of the ITCZ. *J. Clim.* **6**, 2162-2174.

Wang, Y., and Coauthors, 1996: The impact of ocean surface fluxes on a TOGA COARE convective system. *Mon. Wea. Rev.* **12**, 2753-2763.

Webster, P. J., and Coauthors, 1998: Monsoons: Processes, predictability, and the prospects for prediction. *J. Geophys. Res.* **103**(C7), 14451-14510.

Webster, P. J., and Coauthors, 2002: The JASMINE pilot study, *Bull. Amer. Met. Soc*. **83**, 1603-1630.

Wielicki, B. A., and Coauthors, 1996: Clouds and the Earth's Radiant Energy System (CERES) An earth observing system experiment. *Bull. Amer. Meteor. Soc.* **77,** 853-868.

Winker, D. M., and Coauthors, 2009: Overview of the CALIPSO mission and CALIOP data processing algorithms. *J. Atmos. Ocean. Tech.* **26**, 2310-2323.

Wolff, D. B., and Coauthors, 2005 Ground validation for the Tropical Rainfall Measuring Mission (TRMM). *J. Atmos. Ocean. Tech.* **22,** 365-380.

Xu, W., and E. D. Zipser, 2012: Properties of deep convection in tropical continental, monsoon, and oceanic rainfall regimes. *Geophys. Res. Lett*. **39**, L07802, doi:10.1029 /2012GL051242.

Yang, L., and Coauthors, 2016: Flash flooding in small urban watersheds: Storm event hydrologic response. *Water Resour. Res*. **52,** 4571-4589.

Yoon, J., and Coauthors, 2016: An empirical method to improve rainfall estimation of dual polarization radar using ground measurements, *Hydrol. Earth Syst. Sci. Discuss*. doi:10.5194/hess-2016-27.

You, C-H., and D-I Lee, 2015: Algorithm development for the optimum rainfall estimation using polarimetric variables in Korea. *Adv. Meteor*. **2015**, doi:10.1155/2015/395937.

Yuan, J., R. A, Houze, and A. J. Heymsfield, 2011: Vertical structures of anvil clouds of tropical mesoscale convective systems observed by CloudSat. *J. Atmos. Sci.* **68,** 1653-1674.

Yuter, S. E., and R. A. Houze, 1995: Three-dimensional kinematic and microphysical evolution of Florida cumulonimbus. Part II: Frequency distribution of vertical velocity, reflectivity, and differential reflectivity. *Mon. Wea. Rev*. **123**, 1941-1963.

Zhang, Z., and T. N. Krishnamurti, 1996: A generalization of Gill's heat-induced tropical circulation. *J. Atmos. Sci*. **53**, 1045-1052.

Zhang, Y., and Coauthors, 2007: Cluster analysis of tropical clouds using CloudSat data. *Geophys. Res. Lett.* **34,** L12813, doi: 10.1029/2007GL029336.

Zipser, E. J., and K. R. Lutz, 1994: The vertical profile of radar reflectivity of convective cells: A strong indicator of storm intensity and lightning probability?. *Mon. Wea. Rev*. **122**, 1751-1759.

Zipser, E. J., and Coauthors, *2006*: Where are the most intense thunder storms on Earth?. *Bull. Amer. Meteor. Soc.* **87**, 1057-1071.